



BALTO



39th Annual VFS Student Design Competition

eVTOL Air Taxi for Passengers with Reduced Mobility

Sponsored by Bell



*Daniel Guggenheim School of
Aerospace Engineering
Georgia Institute of Technology
Atlanta, GA, 30332*

39th Annual Vertical Flight Society Student Design Competition
Graduate Category

AE 6334 - Rotorcraft Design II

Decoupled by:



Abraham Atte – Graduate Student
CAD & Cabin Design
aatte3@gatech.edu

Decoupled by:



Carlota Bonnet – Graduate Student
Cabin Design & CFD
carlotabonnet@gatech.edu

Decoupled by:



Zelin Hu – Graduate Student
Flight Dynamics & Control
zhu338@gatech.edu

Decoupled by:



Howon Lee – Graduate Student
Structures & CAD
hlee981@gatech.edu

Decoupled by:



Derek Safieh – Graduate Student
Team Leader
dsafieh@gatech.edu

Decoupled by:



Jeremy Louis Seeyave – Graduate Student
Aerodynamics
jseeyave3@gatech.edu

Decoupled by:



Eleni Sotiropoulos-Georgiopoulos – Graduate Student
Flight Dynamics & Control
eas6@gatech.edu

Decoupled by:



Naveen Raj Srinivasan – Graduate Student
naveenraj.s@gatech.edu

Decoupled by:



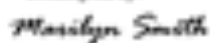
Shreyas Srivathsan – Graduate Student
Propulsion
sshreyas@gatech.edu

Decoupled by:



Siobhán Whittle – Graduate Student
CFD & Aerodynamics
sewhittle@gatech.edu

Decoupled by:



Dr. Marilyn J Smith – Faculty Advisor
marilyn.smith@ae.gatech.edu

Decoupled by:



Dr. Juergen Rauleder – Faculty Advisor
juergen.rauleder@gatech.edu



Daniel Guggenheim School
of Aerospace Engineering
Georgia Institute of Technology
Atlanta, GA, 30332

To the Vertical Flight Society:

The members of the Georgia Institute of Technology Graduate Student Design Team hereby grant VFS full permission to distribute the enclosed Executive Summary and Final Proposal for the 39th Annual Design Competition as they see fit.

Thank you,
The Georgia Tech Graduate Design Team

Acknowledgements

The Georgia Tech Design Team would like to thank those who were able to answer our general technical questions prior to the design.

Industry Professionals The following individuals have either given a technical seminar or have answered general technical questions over the course of the semester (listed in alphabetical order of last names).

Jeremy Bain – Aerodynamicist, Joby Aviation

Dr. Doug Boyd – Senior Aerospace Engineer, NASA Langley Research Center

Jay Carter, Jr. – President, CEO, and Principal Design Engineer, Carter Aviation Technologies

Dr. Chengjian He – Vice President of Research and Development, Advanced Rotorcraft Technology

Anne L. Jannarone – Assistant Dean of Students/Director, Office of Disability Services, Georgia Institute of Technology

Hugues Moreau & Team – CEO, International Aircraft Services (IAS), Abidjan, Côte d’Ivoire

Bob Shaffer – Luxury Travel Advisor, Cruise & Travel Experts

Dr. William Staruk – Aeromechanics Engineer, Joby Aviation

Dr. Vivek Ahuja – CEO, Research In Flight

Natalia Alvarez – Graphic Designer

Georgia Tech Faculty

Dr. Juergen Rauleder

Assistant Professor and Associate Director of Vertical Lift Research Center of Excellence, Daniel Guggenheim School of Aerospace Engineering, Georgia Institute of Technology

Dr. Marilyn J. Smith

Professor and Director of Vertical Lift Research Center of Excellence, Daniel Guggenheim School of Aerospace Engineering, Georgia Institute of Technology

Dr. Jonnalagadda V. R. Prasad

Professor and Associate Director of Vertical Lift Research Center of Excellence, Daniel Guggenheim School of Aerospace Engineering, Georgia Institute of Technology

Dr. Brian J. German

National Institute of Aerospace Langley Associate Professor, Daniel Guggenheim School of Aerospace Engineering, Georgia Institute of Technology, and Director of Georgia Tech’s Center for Urban and Regional Air Mobility (CURAM)

Dr. Chance C. McColl

Lecturer, Daniel Guggenheim School of Aerospace Engineering, Georgia Institute of Technology

Dr. Daniel P. Schrage

Professor Emeritus, Daniel Guggenheim School of Aerospace Engineering, Georgia Institute of Technology

Table of Contents

Acknowledgements	ii
Table of Contents	iii
List of Figures	vii
List of Tables	xi
Nomenclature	xiii
1 Introduction	4
2 Concept of Operations	5
2.1 Operational Requirements	5
2.2 Mission Profile	5
2.3 Stakeholder Requirements: An Overview of Disabilities and Accessibility Needs	6
3 Preliminary Configuration Selection	12
3.1 Customer Requirements	12
3.1.1 Design Objectives	12
3.1.2 Analytical Hierarchy Process (AHP)	14
3.2 Configurations Considered	15
3.3 Vehicle Sizing	18
3.3.1 Methodology	18
3.3.2 Results	20
4 Analysis Tools	21
4.1 GTsim	21
4.2 S&D BEMT	21
4.3 XFOIL	22
4.4 AVL	22
4.5 FlightStream	22
4.6 ANSYS AIM 19.1	22
5 Preliminary Vehicle Sizing	22
5.1 SLSS Results	23
5.2 Rotor Design Goals	24
5.3 Rotor Design	24
5.3.1 Single Main Rotor Compound	25
5.3.2 Tilt-Rotor	25
5.3.3 Multirotor Compound	26

5.3.4	Comparison of Relative Advantages and Disadvantages of Each Rotor Configuration	26
5.4	Mission Energy and Power Requirements	27
5.5	Wing Characteristics	28
5.6	Landing Gear Analysis	29
5.7	Final Configuration Selection	29
6	Vehicle Design Overview	30
6.1	Vehicle Performance	30
6.2	Vehicle Systems Overview	31
7	Cabin Design	32
7.1	Initial Cabin Sizing	32
7.1.1	Wheelchair Market Study	32
7.1.2	Sizing Considerations	33
7.2	Cabin Configuration Selection	33
7.3	Seat Selection	34
7.3.1	Selection of the fixed seats	34
7.3.2	Selection of the folding seats	34
7.3.3	Design of wheelchair tie-downs	35
7.4	Final Cabin Configuration	36
7.4.1	Cockpit layout	36
7.4.2	Main cabin layout	36
7.4.3	Cabin Entry Points	39
7.4.4	Cabin Acoustics	40
7.5	Operations, Ingress & Egress	40
7.5.1	Requirement Compliance	41
8	Fuselage Aerodynamic Design	43
9	Rotor Design	45
9.1	Lifting Rotors	45
9.1.1	Methodology	45
9.1.2	Airfoil Selection	47
9.1.3	Trade Study	49
9.1.4	Final Lifting Rotor Design	50
9.2	Cruise Propellers	51
9.2.1	Airfoil Selection	51
9.2.2	Trade Study	51
9.2.3	Final Propeller Blade Design	53
9.3	Hub Design	53

9.4	Blade Structure	56
9.5	Lifting Rotor – Cruise Propeller Interaction in Transition	57
10	Aerodynamic Wing Design	58
10.1	Airfoil Selection	58
10.2	Trade-study on Wing Planform Design	59
10.3	Final Wing Design	60
11	Structural Design	61
11.1	Limit Load Definitions	61
11.2	Shear and Moment Diagram	63
11.3	Airframe Design	63
11.4	Wing Structural Design	65
11.4.1	Wing Spar	65
11.4.2	Motor Boom	66
11.4.3	Wing Assembly FEA	67
11.5	Landing Gear Design	68
11.5.1	Trade Studies	69
11.5.2	Landing Gear Characteristics	70
11.6	Fatigue Analysis	71
12	Powerplant System	73
12.1	Battery Selection	73
12.2	Motor and Electronic Speed Controller Analysis	75
12.3	Motor and ESC Placement	76
12.4	Wiring & Battery Placement	76
12.4.1	Wiring Material	76
12.4.2	Wiring Diagrams and Battery Setup	77
12.5	Gear Box	77
12.6	Powertrain Operational Considerations and Maintenance	80
13	Weight Breakdown and CG Analysis	81
14	Flight Mechanics and Control	84
14.1	Hover Analytical Dynamic Model	84
14.2	Cruise Analytical Dynamic Model	84
14.3	Tail and Control Surface Sizing	85
14.3.1	Horizontal Tail Sizing and Longitudinal Stability	85
14.3.2	Vertical tail Sizing and lateral stability	87
14.3.3	Control Surfaces	88

15 Vehicle Performance & Maneuvers	91
15.1 Power Required Curve	91
15.2 Hover Ceiling	92
15.3 Service Ceiling	93
15.4 Maneuvers	93
15.5 Results for Minimum Measures of Agility	94
15.5.1 Angular Rate Control in OGE Hover	94
15.5.2 Vertical Agility in OGE Hover	94
15.5.3 Attitude change in cruise	95
15.6 Limiting Maneuvering Load Factor	95
16 Acoustics	96
17 Lifecycle Cost Analysis	98
17.1 Acquisition Cost	98
17.2 Operating Cost	98
17.3 Maintenance Cost	99
17.4 Cost Comparison	99
18 Summary	99
References	101

List of Figures

Figure 2.1	Vehicle Mission Profile	6
Figure 3.1	Weights and ranking of cabin selection objectives	15
Figure 3.2	Weights and ranking of configuration selection objectives	15
Figure 3.3	Configurations considered	16
Figure 3.4	Pugh Matrix Results with respect to the multicopter	18
Figure 3.5	SLSS General Calculating Algorithm	19
Figure 3.6	SLSS results for the SMR	19
Figure 3.7	Power curve results from SLSS for final three potential configurations	20
Figure 4.1	S&D Validation against Experimental Data	21
Figure 5.1	Preliminary design of the three selected configurations	23
Figure 5.2	Single Main Rotor parametric study	25
Figure 5.3	Tilt Rotor Parametric Study	25
Figure 5.4	Multirotor Compound parametric study	26
Figure 5.5	Landing gear models analyzed	29
Figure 6.1	Stage wise battery and time	31
Figure 6.2	Torque response to one motor loss	31
Figure 6.3	Location of variable/fixed pitch rotors on <i>Balto</i>	32
Figure 7.1	Cabin configurations considered	33
Figure 7.2	Virtual Reality recreation of the preliminary cabin layout	34
Figure 7.3	Stow 'n Go™ folding mechanism	35
Figure 7.4	Components of the WTORS	35
Figure 7.5	Buckle and tongue attachment	36
Figure 7.7	Cockpit view	36
Figure 7.6	Cabin configurations three-view	37
Figure 7.8	Cabin and undercarriage storage locations (wheelchair rails and folding seat compartments hidden for clarity)	38
Figure 7.9	Undercarriage storage compartment access door	38
Figure 7.10	<i>Balto</i> 's open ramp for boarding	40
Figure 8.1	Fuselage iterative stages, side views	43
Figure 8.2	Fuselage iterative stages, isometric views	43
Figure 8.3	Pressure coefficient contours of the fuselage without and with fairing	44
Figure 8.4	Pressure coefficient at the empennage without and with fairing	44
Figure 8.5	Streamlines around the aerodynamic empennage	44
Figure 9.1	Schematic outline of the blade aerodynamic process	46
Figure 9.2	Reynolds and Mach numbers on lifting rotor disk for hover and transition speeds	47
Figure 9.3	Performance characteristics for different airfoils	48
Figure 9.4	Lift-to-drag ratio and moment coefficient for airfoils Eppler 360, Eppler 852, and Clark X	48

Figure 9.5	Design Space Pareto Front	49
Figure 9.6	Balto's Design Point Blade vs. rectangular untwisted planform	49
Figure 9.7	Induced Power Loss vs. Out-board taper ratio	49
Figure 9.8	Blade Geometric Characteristics	50
Figure 9.9	C_l/C_d vs. α	51
Figure 9.10	η vs. radius	52
Figure 9.11	Operation in cruise condition, $\Omega = 120 \text{ rad/s}$	52
Figure 9.12	η vs. Rotational Speed. Collective trimmed to required thrust	52
Figure 9.13	η vs. Twist Rate over Radius	53
Figure 9.14	η vs. Taper Ratio (in-board & out-board)	53
Figure 9.15	Propeller Blade Geometric Characteristics	54
Figure 9.16	Hover Variable Pitch Mechanism	55
Figure 9.17	Cruise Variable Pitch Mechanism	55
Figure 9.18	Nylon 66 Miter Gear FEA Cross-check	56
Figure 9.19	Blade Structure	57
Figure 9.20	FEA Analysis for Blades	57
Figure 9.21	Wake interaction during transition flight, $V = 27\text{m/s}$	58
Figure 10.1	Lift-to-drag ratio and moment coefficient for airfoils NACA 4412, LA 203, and Eppler 423	59
Figure 10.2	Velocity magnitude contours of the wing without and with propeller-induced flow at 105 knots	60
Figure 10.3	Velocity magnitude contours of the wing without and with propeller-induced flow at 105 knots	60
Figure 11.1	The magnitudes and locations of the loads in the three limit maneuver loading conditions	61
Figure 11.2	The magnitudes and locations of the loads in the two transverse gust conditions . . .	62
Figure 11.3	The magnitudes and locations of the loads in the two landing load conditions	62
Figure 11.4	The magnitudes and locations of the loads in the rotor failure condition	63
Figure 11.5	Total shear and bending moment diagrams for all seven limit loading conditions . . .	63
Figure 11.6	Airframe CAD model and description of different locations on the bulkhead cross-section	64
Figure 11.7	The Equivalent Von-Mises stress of the airframe at the three heavily loaded conditions: vertical landing with max load, vertical landing with drag load, and rotor failure. All loads are multiplied by safety factor of 1.5. All units are in Pascals.	65
Figure 11.8	The types of loads that the wing experiences at various flight regimes	66
Figure 11.9	The dimensions for the three candidates of main spar cross-section	66
Figure 11.10	The bending stiffnesses in all three directions for the main spar cross-section candidates	67
Figure 11.11	Wing CAD model and description of different locations on the wing cross-section . . .	67
Figure 11.12	An isometric view of the motor boom structure. The wing attachment plate is joined to a rib-like structure which is connected to the main spar. The motors are mounted on top of the motor attachment plates on both sides of the boom.	67

Figure 11.13	The Equivalent Von-Mises stress of the wing assembly at its three most heavily loaded conditions: the upward vertical gust condition, rotor failure condition, and the symmetrical pushover in V_{mo} . All loads are multiplied by safety factor of 1.5. All units are in Pascals.	68
Figure 11.14	The acceleration in terms of gravitational acceleration of the aircraft during impact for the skid and the oleo-pneumatic landing gear	69
Figure 11.15	The contour plot of the coefficient of pressure around the fuselages of different landing gear retractability conditions at cruise speed of 54.02 m/s (177.22 ft/s)	69
Figure 11.16	The comparison of the load stroke curve for a conventional landing gear and the extreme energy absorbing landing gear (EEA).	71
Figure 11.17	The Equivalent Von-Mises stress of the landing gear assembly for the two landing load conditions. All loads are multiplied by safety factor of 1.5. All units are in Pascals.	71
Figure 11.18	Rotating shaft model and corresponding material S-N curve used to determine fatigue damage	72
Figure 11.19	Fatigue simulation results	73
Figure 12.1	Trends for battery properties in existing technology	74
Figure 12.2	Hover and cruise motor gear boxes	76
Figure 12.3	Full vehicle electrical wiring diagram, top view	78
Figure 12.4	Full vehicle detailed electrical wiring diagram, top view, ESC wiring	79
Figure 12.5	Full vehicle electrical wiring diagram side view	79
Figure 12.6	Performance plots for EMRAX 268 motor	80
Figure 12.7	Potential maintenance hatches marked in red	81
Figure 13.1	<i>Balto</i> 's CG travel for different cabin arrangements (in red) with respect to the fuselage box (in grey)	81
Figure 14.1	Short period mode flying qualities, red dot identifies <i>Balto</i> 's results	87
Figure 14.2	Lateral mode characteristics depending on vertical tail surface S_v and span b_v	88
Figure 14.3	Historical guidelines of aileron sizing	89
Figure 14.4	Minimum aileron deflections for roll attitude change with respect to forward speed	89
Figure 14.5	Elevator-wing chord ratio	89
Figure 14.6	Effect of elevator areas on achieving pitch agility	90
Figure 14.7	Time for 10 deg pitch change for the selected elevator area	90
Figure 14.8	Rudder deflection required to counter engine loss depending on cruise speed and vertical tail surface	91
Figure 14.9	Time required to achieve +/- 6 deg change of heading for different amplitudes of rudder deflections	91
Figure 15.1	Power required curve with lifting rotor and cruise propeller available power	92
Figure 15.2	HOGE ceiling versus GTOW	92
Figure 15.3	Altitude versus power required for HOGE. The lower dotted black line is the power available during normal operation conditions. The higher dotted black line is the power available when all motors are utilized.	92
Figure 15.4	Service ceiling	93
Figure 15.5	Service ceiling vs. GTOW	93
Figure 15.6	Power required curve with lifting rotor and cruise propeller available power	93

Figure 15.7	Variation of roll angle and roll rate with time for a roll maneuver in hover with wind	94
Figure 15.8	Variation of rotor thrust with time for a roll maneuver in hover with wind	94
Figure 15.9	Variation of pitch angle and pitch rate with time for a pull-up in hover with headwind	94
Figure 15.10	Variation of rotor thrust with time for a pull-up in hover with headwind	94
Figure 15.11	Change of g values and rotor thrust values in the vertical acceleration	95
Figure 15.12	Lateral state trajectories in rolling	96
Figure 15.13	Pitch angle and pitch rate variation with time	96
Figure 15.14	Yaw angle and yaw rate variation with time for a -15-degree rudder deflection	96
Figure 15.15	Climb inputs with one motor at max. continuous torque	96
Figure 16.1	Hover acoustics test setup (top view). Microphones are represented with red spheres .	97
Figure 16.2	Sound pressure level at various vertical heights below the rotors	97

List of Tables

Table 2.1	RFP Vehicle, Cabin, and Mission Requirements	5
Table 2.2	RFP Mission Profile Summary	6
Table 3.1	Requirements to provide maximum comfort and safety to passengers with disabilities based on Design Objectives	13
Table 5.1	Parameters obtained from the SLSS results for the three selected configurations	23
Table 5.2	Rotor characteristics for each configuration	24
Table 5.3	Mission segments energy requirements for each vehicle	28
Table 5.4	Mission segments power requirements for each vehicle	28
Table 5.5	Motor and controller selected for each vehicle configuration	29
Table 5.6	Wing characteristics for each possible configuration	29
Table 6.1	Vehicle performance	30
Table 6.2	Vehicle rotor performance	30
Table 6.3	Vehicle Propeller Performance	31
Table 7.1	Examples of wheelchair types, sizes, and weights; maximum values are highlighted	33
Table 7.2	Items and passengers and their weights in each cabin configuration. The differences between configurations are highlighted in bold.	39
Table 7.3	Cabin requirement compliance	42
Table 9.1	Lifting rotor performance characteristics	51
Table 9.2	Cruise Propeller Performance at $V_c = 105$ knots	54
Table 9.3	Material Comparison for Variable Pitch	56
Table 9.4	Total weight per pitch mechanism for all rotors	56
Table 9.5	Rotary System Weight	57
Table 10.1	Wing planform parameters weights	59
Table 10.2	Wing planform trade study results in percent	59
Table 10.3	Wing aerodynamic properties at 105 <i>knots</i> forward speeds without and with propeller-induced flow	61
Table 11.1	Maximum stresses and locations on the airframe at different limit load conditions	64
Table 11.2	Maximum stresses and locations on the wing assembly at different limit load conditions	68
Table 11.3	Maximum stresses and locations on the landing gear at different limit load conditions	71
Table 11.4	Shaft material properties	71
Table 11.5	Shaft loads and stresses	72
Table 11.6	Shaft fatigue damage accumulated during each mission segment	73
Table 12.1	Potential battery material comparison and selection	74
Table 12.2	Potential Motors Comparison and Selection	75
Table 12.3	Potential gears comparison and selection	79
Table 12.4	Potential gears comparison and selection	80
Table 13.1	Location of <i>Balto</i> 's center of gravity	82
Table 13.2	<i>Balto</i> ' moments of inertia	82

Table 13.3	<i>Balto</i> mass and cost	83
Table 14.1	Horizontal tail volume ratio	86
Table 14.2	Horizontal tail aspect ratio and taper ratio	86
Table 14.3	Longitudinal modes results for the selected horizontal tail	87
Table 14.4	Lateral modes results for the selected vertical tail	89
Table 17.1	<i>Balto</i> 's acquisition cost breakdown	98
Table 17.2	<i>Balto</i> 's operating cost breakdown	99
Table 17.3	<i>Balto</i> 's maintenance cost breakdown	99

Nomenclature

ω^b	Angular velocity vector of the aircraft
τ^a	Moment due to aerodynamic forces
F^a	Aerodynamic and propulsive force vector
I^b	Inertia matrix of the aircraft
r^i	Position vector of i th lifting rotor relative to aircraft CG
s^i	Direction of i th lifting rotor angular momentum
T^i	i th lifting rotor thrust vector
V^e	Aircraft velocity vector of mass center relative to earth fixed point
η_H	Dynamic pressure ratio of the horizontal tail
Ω	Angular speed of lifting rotor
τ_D	Anti-torque on lifting rotor due to drag
τ_E	Torque by electric motor
$C_{L_{\alpha,H}}$	Horizontal tail lift curve slope
$C_{M_{\alpha,f}}$	Pitch stiffness due to fuselage
$C_{M_{\alpha}}$	Pitch stiffness coefficient
$x_{ac,w}$	Longitudinal location of wing aerodynamic center
x_{cg}	Longitudinal CG location
μ_g	Vehicle mass ratio, [-]
ρ	Density, [kg/m ³] or [slug/ft ³]
θ_{tip}	Linear twist rate
θ_{tw}	Spanwise twist rate
a_V	Vertical tail volume
b	Wing span
b_r	Rudder span
b_V	Vertical tail span
c	Rotor chord
c_r	Rudder chord
c_V	Vertical tail chord
$C_{D_{v,f}}$	Fuselage vertical drag coefficient
$C_{L,\alpha}$	3D lift curve slope, [/radian]
DL	Disk Loading
eta_V	Vertical tail dynamic pressure ratio

g	Gravitational constant, [m/s ²] or [ft/s ²]
J	Lifting rotor inertia
K_g	Gust alleviation factor
L/D_i	Lift to induced-drag ratio, [-]
L	Lift, [N] or [lb]
MGC	Mean geometric chord, [m] or [ft]
n_g	Gust load factor
q	Dynamic pressure
R	Rotor radius
R_{cut}	Root Cut-out
S	Wing area, [m ²] or [ft ²]
S_f	Fuselage area from the top view
TR_{in}	in-board taper ratio
TR_{out}	out-board taper ratio
TR_{trans}	taper ratio transition location
Ude	Vertical gust velocity, [m/s] or [ft/s]
V	Aircraft speed in KEAS, [knots]
W	Gross weight, [kg] or [lb]
y_T	Distance from the operating engine to the fuselage centerline along the body y axis
$d\epsilon_{\frac{d\alpha}{d\alpha}}$	Downwash change with angle of attack
V_H	Volume ratio of the horizontal tail

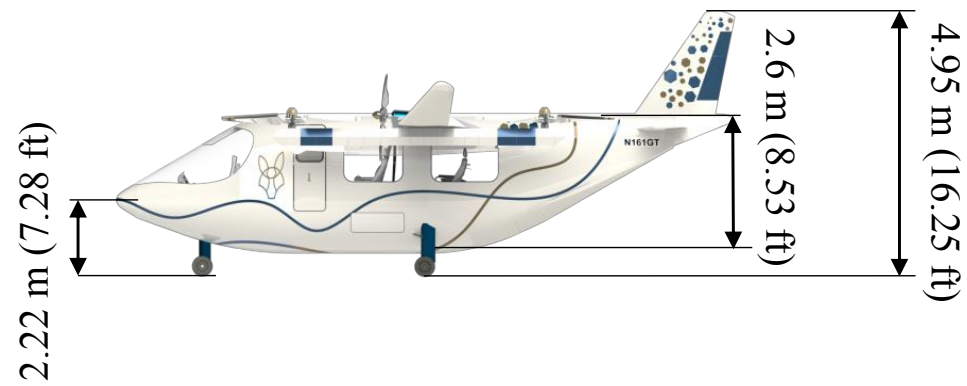
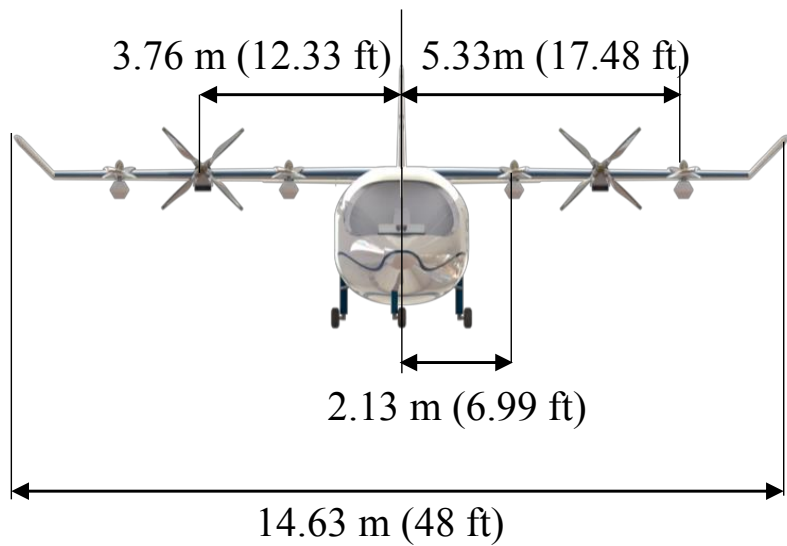
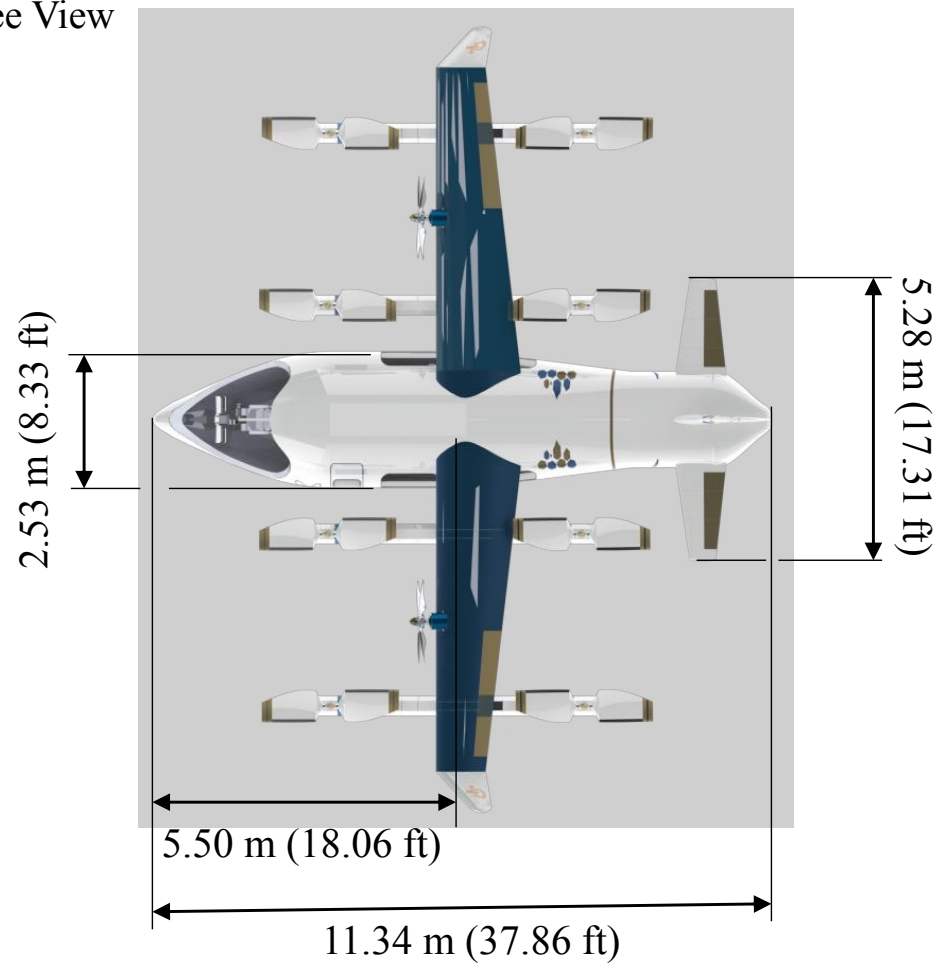
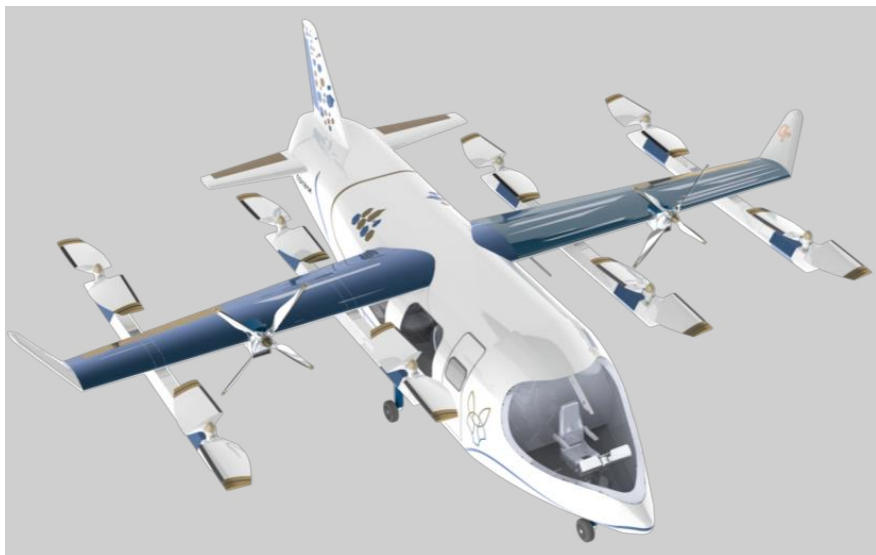
Balto RFP Requirements and Compliances

RFP Requirement	Solution	Chapter
The design shall conform to the applicable requirements of 14 CFR 29.1433 – §29.833	The cabin, cockpit and baggage compartments conform with the applicable requirements	7
The distribution of thrust among the powered elements combined with lifting surfaces and airframe aerodynamic forces can be placed in equilibrium about the center of gravity (cg)	The vehicle lifting surfaces and propulsive elements are placed in such a manner that the net forces and moments about centre of gravity remain in equilibrium	13
The aircraft shall be capable of recovering from critical maneuvering conditions	The vehicle has sufficient control surfaces and electric motors.	14
The aircraft can generate revenue in its role as an air taxi	Comparison to existing air taxis put <i>Balto</i> in competitive ranges for revenue generation	17
The aircraft shall maintain a climb rate of 30.48 m/min (100 ft/min) at the forward speed for minimum power	<i>Balto</i> 's climb rate exceeds the requirements up to 11,000 m (36,000 ft)	15.3
In OGE hover with a wind of 31.48 km/hr (17 knots) from the critical direction, there shall be sufficient control power to generate aircraft angular rate responses within 1.5 seconds of at least 15 deg/sec in pitch, roll, and yaw	With 8 designed lifting rotors under RPM plus variable-pitch control, the vehicle can achieve the requirement.	15.5.1
In OGE hover there shall be sufficient vertical agility to accelerate from 1.0g to no less than 1.25g in 1.5 seconds	<i>Balto</i> can accelerate from 1.0g to 1.25g in 0.8 seconds	15.5.2
In cruise, there shall be sufficient control power to achieve attitude changes from trim of 10-deg pitch, 10 deg roll, and 6 deg heading within 1.5 seconds	<i>Balto</i> 's control surfaces are able to provide enough control authority to perform required maneuvers.	15.5.3
The landing gear shall be designed to absorb the energy associated with a rate of sink equal to 2 m/s (6.55 ft/s) at initial ground contact	<i>Balto</i> 's landing gear can withstand a rate of sink equal to 4.08 m/s (13.39 ft/s)	11.5

Documentation Requirements and Compliances

Documentation Requirement	Chapter
Compliance checklist for the cabin requirements from 14 CFR 29 and accessible cabin requirements	7.5.1
Description of each cabin configuration by a list containing items that are included in that configuration	7.4.2
Trade study of three configurations	5
Weight breakdown, and center of gravity analysis for the selected configuration	13
The control system sizing to meet certain threshold requirements, and the aircraft recovery from critical maneuvering conditions capabilities	14, 15
Aerodynamic properties of the aircraft, and structural analysis for loads associated with the critical flight maneuvering conditions	9.1, 10, 14
Landing gear energy absorption characteristics, and structural analysis of loads associated with limit landing conditions	11.5
Description of the operating envelope such that the aircraft can generate revenue in its role as an air taxi	17
Envelope of aircraft gross weight versus longitudinal center of gravity position considering all combinations of allowable passenger and baggage configurations for the various cabin configurations	13
Intrinsic performance of the aircraft shall be established: maximum takeoff altitudes plotted versus the range of gross weights, maximum operating altitudes versus the range of gross weights, maximum takeoff and operating altitudes	15
Design maximum operating speed V_{MO} is no less than the cruising speed established for the design mission and no greater than the maximum level flight speed with the drive system providing maximum continuous power	15
Structural properties for the materials chosen and identification of the most stressed point for each section of the fuselage	11.3
Perform a fatigue analysis of the most critically loaded, rotating element of the drive system	11.6

Vehicle Three View



1 Introduction

Recent urban densification has generated congestion and pollution issues in every major city. In this context, transportation companies and aircraft manufacturers have shown a growing interest in urban air mobility (UAM) and advanced air mobility (AAM) solutions. New advances in electric propulsion technology have made it feasible to develop a new generation of Vertical Take-Off and Landing (VTOL) vehicles designed with an emphasis on affordability, reduced emissions, and quietness. If the goal is to “move city commuting into the sky” [1] or “spend less time traveling and more time living” [2], it is imperative that this goal be met for all. Designing novel urban air mobility vehicles with the needs of people with disabilities in mind will open the benefits of UAM to a broader demographic and will contribute to making air travel more inclusive.

According to the Center for Disease Control (CDC), one out of four adults has a disability (physical or hidden) [3]. While incorporating new technologies in the aerospace field has made it achievable to move individuals over longer distances in shorter amounts of time, air transport of persons with disabilities or reduced mobility is often overlooked [4]. A white paper prepared by The Civic Air Transport Association and Aerobility calls upon UAM and AAM developers to consider the needs of those who “stand to benefit most from its introduction – disabled communities” by providing an inclusive mode of transportation from one location to another [4].

Balto, named for the lead sled dog that carried the life-saving diphtheria antitoxin from Anchorage to Nome in 1925, is a lift-cruise configuration designed by the Georgia Institute of Technology (GT) Graduate Design Team to transport persons with reduced mobility (PRM) safely. As was the case in 1925, *Balto* provides help to people when other means of transportation fall short. The team consulted with Anne L. Jannarone (Director of Georgia Tech’s Office of Disability Services) and M. Bob Shaffer (a travel agent that specializes in travel for people with disabilities), amongst others, to ensure that the needs and preferences of those with disabilities were foremost in the design of the vehicle. The team also consulted with several industry experts on the technical aspects of the design to ensure that the resulting eVTOL could safely and efficiently complete the required mission.

The mission requires a vehicle that can transport passengers between an urban, suburban, or rural hub to an airport located at least 100 miles away, with a configurable cabin that can accommodate at least two passengers with reduced mobility or four passengers with full mobility. *Balto* exceeds the mission requirements with the safety and comfort of the PRM passengers as the critical design parameter. The multicopter lift/thrust compound vehicle is designed to seamlessly transition from hover to forward flight to maintain level flight and reduce the amount of motion experienced by the passengers inside the vehicle. The redundancy of the overall design removed any single failure points. Because only a few customers are being transported, the cabin is designed to provide a comfortable and deluxe journey from start to endpoint. The design was configured and analyzed using a combination of in-house codes developed for this project, high- and mid-fidelity solvers, and analytic methods.



2 Concept of Operations

The Request for Proposal (RFP) seeks an “eVTOL design [that] might alleviate some of the challenges, remove barriers and create an enabling environment” for “people with disabilities of all types - including hidden disabilities” [5]. With this charter, a vehicle that is *just another cool looking* UAM/AAM concept *must* be secondary to creating a safe vehicle with an environment that minimizes emotional stress and physical discomfort for these passengers.

2.1 Operational Requirements

As outlined in the 2022 VFS Student Design Competition RFP, the general vehicle, cabin, and mission-specific requirements [5] are provided as a quick reference in Table 2.1.

<i>General Vehicle Requirements</i>	
Propulsion System	Electric propulsion with vertical takeoff and landing
Max Length and Width	15.24 m (50 ft)
Max Tip Speed	183 m/s (600 ft/s)
Certification Basis	FAA 14 CFR Part 29
<i>Cabin Requirements</i>	
Cabin Layout	Configurable
Baseline Configuration	4 passengers + 1 pilot No mobility restrictions
Alternate Configuration	2 passengers + 1 pilot Passengers with reduced Mobility
Baggage Space	0.22 m ³ (7.9 ft ³) per passenger
Baggage Weight	38 kg (83 lb) per passenger
<i>Mission Requirements</i>	
Mission Range	161 km (100 miles)
Atmospheric Conditions	ISA+20°C

Table 2.1 RFP Vehicle, Cabin, and Mission Requirements

The RFP is seeking novel designs that will extend the use of eVTOL vehicles for short-range missions for people of all demographics. Hence, the design must transport up to four passengers with no mobility restrictions and at least two passengers with reduced mobility between an urban, suburban, or rural hub and an airport separated by 160 km (100 miles). The primary goal of the aircraft is to ensure the safety and comfort of the passengers in transit while also executing the mission in the most efficient way possible.

2.2 Mission Profile

The RFP-designated vehicle mission is graphically represented in Figure 2.1 with a segment summary in Table 2.1.

The RFP defines ground elevation at both the origin and final destination of the mission to be 609.6 m (2000 ft). The mission begins with the vehicle performing a normal vertical takeoff and hover in ground effect (IGE) for ten seconds. The vehicle shall then vertically climb out of ground effect for a distance of 30.48 m (1000 ft) until an altitude of 640.1 m



(200 ft) is reached. The vertical climb rate of the vehicle is 48.77 m/s (160 ft/s). At the desired altitude, the vehicle shall then hover for another ten seconds before climbing 609.6 m (2000 ft) to reach the 1219.2 m (4000 ft) cruise altitude. The ascent climb angle is 9.46°. The vehicle shall reach cruise velocity when a distance of 3.47 km is achieved. The vehicle shall then cruise for an additional 149.1 km before beginning its descent. A prescribed angle of descent of 4° is given in the RFP, meaning the vehicle will start descending at 8.28 km from the final destination. Once the vehicle has descended 609.6 m (2000 ft) to an altitude of 640.1 m (2100 ft), the vehicle shall hover for ten seconds. Finally, the vehicle will begin its final descent and execute an IGE hover for ten seconds before vertically landing.

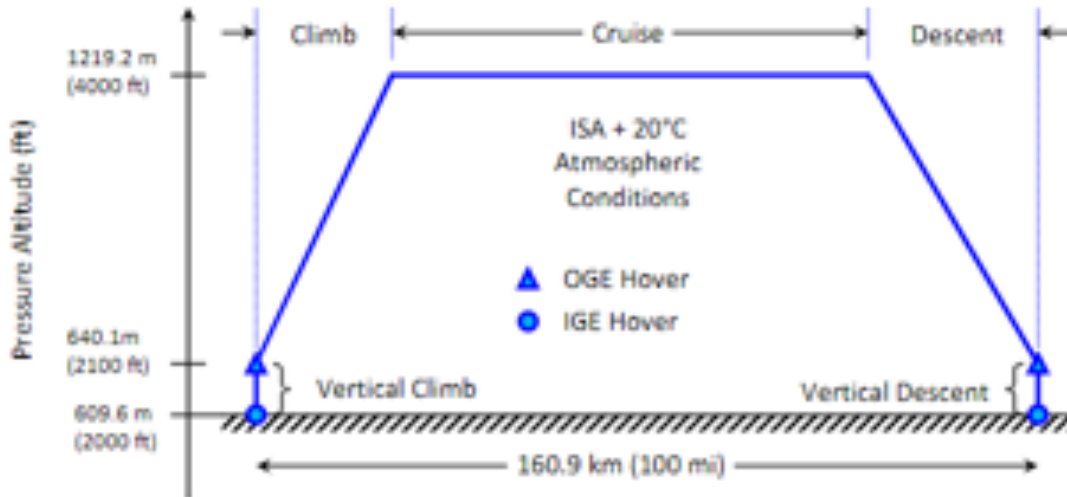


Figure 2.1 Vehicle Mission Profile (from Ref. 5)

<i>Mission Segment</i>	<i>Segment Characteristics</i>
Normal vertical takeoff to IGE hover	0 sec
IGE hover	10 sec
Vertical climb to 30.48 m (100 ft) AGL	Rate of climb (ROC)= 48.77 m/s (160 ft/min) OGE
OGE hover at 30.48 m (100 ft) AGL	10 sec
Steady climb to 609.6 m (2000 ft) AGL	Climb gradient = 1:6 (9.46 deg angle of climb)
Cruise at 609.6 m (2000 ft) AGL	ISA + 20°C at all mission points
Steady descent to 30.48 m (100 ft) AGL	Angle of descent = 4 deg
OGE hover at 30.48 m (100 ft) AGL	10 sec
Vertical descent to IGE hover	
IGE hover	10 sec
Normal vertical landing from IGE hover	0-sec

Table 2.2 RFP Mission Profile Summary

2.3 Stakeholder Requirements: An Overview of Disabilities and Accessibility Needs

The World Health Organization (WHO) defines disability as “an umbrella term, covering impairments, activity limitations, and participation restriction” [6]. In contrast, the ADA defines a person with a disability as a person who has a “physical or mental impairment



that substantially limits one or more major life activity, a person who has a history or record of such an impairment, or a person who is perceived by others as having such an impairment” [7].

The GT team consulted with Anne Jannarone, the Director of the Office of Disability Services at Georgia Tech, and Bob Shaffer, a luxury travel advisor that specializes in travel for people with disabilities. The team wanted to ensure the customers’ needs – passengers with disabilities – were always the priority at every step in the design. Consulting with experts allowed the team to verify findings from research and obtain more insight into real travel experiences and challenges of people with disabilities while ensuring no misunderstandings or omissions were made.

Disabilities can take many forms and are not always visible. Our consultation with the Georgia Tech Office of Disability Services found that the main population of students with disabilities has a form of hidden disability [8]. A hidden, or invisible, disability is a disability that is “not to be immediately noticed by an observer except under unusual circumstances or by disclosure from the disabled person or other outside sources” [9]. A study by the Center for Talent Innovation showed that among white-collar, college-educated employees, 30% have a disability, and of all employees with a disability, 62% have an invisible disability [10].

Working with Georgia Tech’s Office of Disability Services, the team divided disabilities into different categories, considering the consequences of each disability and the vehicle design constraints needed to alleviate both physical and emotional/mental concerns. While not all disabilities fit into a specific category, and every person with a disability is unique, the team hopes that all passengers with disabilities will feel comfortable and respected while aboard the vehicle by addressing particular groups’ needs. The team presents a non-exhaustive list of disabilities considered and what unique design considerations they bring.

Reduced mobility with mobility aids:

Mobility aids are devices designed to help people with reduced mobility move and enjoy more freedom; they include wheelchairs, scooters, walkers, crutches, and canes. For simplicity, mobility scooters will be included when using the term wheelchair. The first consideration regarding mobility aids is accessing the vehicle, as regular stairs or steps are unable to be used. A ramp or lift is needed to allow access to wheelchairs into the vehicle. Crutches and cane users can use both stairs and ramps, but multiple testimonies and studies show that, in general, they prefer to use ramps, as even slopes are easier to navigate than steps [11]. Wolfenbarger and Shehab showed that ramps are also preferred for people with reduced mobility without mobility aids and older people. Respondents to their study cited being “less fatigued, less likely to trip, and more comfortable when using ramps” [12].

For ease of access into their seats, passengers with reduced mobility prefer seats where the armrest can be removed or lowered. The Air Carrier Access Act (ACAA) requires half of the aisle seats to have movable armrests [13]. Transfer from wheelchairs to seats must be easy, comfortable, and efficient, requiring sufficient space. Some wheelchair users can self-transfer into seats, but others need assistance. While relocating from wheelchairs to the seat is the option used in airplanes, passengers might prefer to stay in their wheelchairs for the flight duration, as is done in road travel. Remaining seated might be the only possibility if the wheelchair cannot be folded or if a mobility scooter is used. In that case, the wheelchair or scooter has to be strapped safely onto the cabin floor and still allow for a safe and comfortable



flight. FAA regulations allow for wheelchair strapping or strapping the wheelchair on the cabin floor using the same regulations as for cargo [14].

Wheelchair users almost always fly with a companion or caregiver familiar with their disability and how to assist them [15]. Mobility aid for cane and crutches users must be easily accessible, especially before and after the flight. Moreover, people using crutches want to avoid unnecessary physical contact with others [15]. The study reported stumbling on other passengers, making it an unpleasant experience for both parties.

Design considerations: Ramp access, easy transfer to a seat, wheelchair tie-down mechanism, good aisle width, seating arrangements for a caregiver.

Reduced mobility without mobility aids:

Reduced mobility does not always involve mobility aids; some of these disabilities are invisible. People can have a disability that impacts their mobility but does not require the use of mobility aids. For example, people with chronic pain, chronic fatigue, or muscle atrophy do not always need or choose to use mobility aids; however, they still deserve special accommodations. As with cane and crutches users, many people with physical disabilities who do not use mobility aids prefer ramps to stairs for similar reasons: it requires less effort to climb. Moreover, special care should be taken to increase comfort during flights. Seats should be comfortable so that aches and pains experienced by passengers with chronic pain or chronic fatigue are minimized.

Design considerations: Ramp access, easy transfer to seat, comfortable seats.

Low vision and blindness:

Often a hidden disability, low vision, or blindness can present significant challenges during travel. An exploratory study on the flight experiences of blind people showed that blind people want to avoid unnecessary physical contact with others [15]. Some blind people said they were not familiar with the crew members' safety information or the film; moreover, they reported feeling insecure about hearing or understanding messages relayed on the public announcement system [15]. Therefore, it is essential to include all information in accessible formats - the text should be written so that any text-to-speech software can translate it. All written instructions should also include Braille. If an announcement system is used, the ambient volume must be low to not interfere with the understating of the message.

Braille can be a valuable tool for communicating written information to vision-impaired passengers. However, the American Printing House stated that only 8% of blind children in 2020 could read Braille [16], and this trend extends to adult populations as well. Only one in ten blind adult people can read Braille [17]. However, it is essential to include other forms of communication that are accessible to people with vision impairments. Consequently, all information presented to passengers should be delivered in audio and written form, including information traditionally only shown in writing.

Blind people almost always travel with a companion familiar with their disability and who knows how to assist them [15]. The vehicle shall therefore be designed to accommodate a companion for people who are blind.

Blind people might travel with a mobility cane or with a service animal. These are



addressed in other parts of this section.

Design considerations: Good aisle width, audio information, low ambient noise, text-to-speech translation, seating arrangements for a caregiver.

Hearing impairment:

When traveling, people with partial or complete deafness face unique challenges: announcements are inaccessible, last-minute changes are hard to obtain, and safety protocols can be hard to communicate. It is thought that 4% of the world population is affected by deafness [18]. All information should be presented visually to allow passengers with hearing impairments to understand all information communicated to them.

Design considerations: Visual information, speech-to-text translation.

Epilepsy:

According to the World Health Organization, 50 million people are affected by epilepsy globally, or between 4 and 10 per 1000 people [19]. In 2015 the CDC estimated that 1.2% of the U.S. population was affected by epilepsy [20]. Baker et al. found that 37% of the children/teenagers in their study expected their condition to hinder their future opportunities for traveling and exploring [21]. McIntosh found that, while having epilepsy did not impede people from traveling, it could cause them distress [22]. Some participants cited the long wait times as a deterrent to air travel. None of the study participants had traveled alone; similar to people who use wheelchairs and people with vision impairments, people with epilepsy rarely travel alone. It is crucial to accommodate seats for the companion and the disabled passenger.

While most epileptic seizures occur in people with a history of epilepsy, they can affect people with no history of seizures when traveling with rotorcraft. In 2007, a patient being transported to the emergency room by helicopter after a lawn-mower accident suddenly experienced an onset of epileptic seizures that lasted several minutes. The patient had no history of photosensitive epilepsy and did not suffer from seizures before or after this incident. After investigation, the medical team concluded that the seizures had been caused by the sunlight shining through spinning helicopter rotor blades [23]. The phenomenon, known as “Rotor Flicker Vertigo”, is often underreported despite being crucial for the safety of passengers in rotorcraft [23]. Flicker Vertigo is defined as “an imbalance in brain cell activity created by light sources that emit flickering rather than a steady light,” typified by nausea, vertigo, and, in rare cases, seizure activity [24]. Considering the effects of rotor flicker and how to mitigate them is crucial, especially for the required vehicle. Passengers not necessarily used to traveling by rotorcraft could be exposed to rotor flickers in transit. While the effects of flicker vertigo are usually mild (nausea is the most common symptom), they can cause photosensitive epilepsy on rare occasions. People with a history of epilepsy are much more likely to suffer from seizures if exposed to rotor flicker and therefore need to be shielded from it.

While specific cases of Rotor Flicker Vertigo have been reported (e.g. [23,24]), there have been no extensive studies on the phenomenon. While a communication report studied the effect of multiple factors - including contrast, frequency, and retinal area stimulated - in flicker vertigo caused by wind turbines [25], few studies of the sort exist for rotorcraft. The



design should prevent the potential of flicker vertigo and shield passengers from the rotating blades. This can be done through window placement or window coverings.

Design considerations: Shield for light filtering through the windows and windshield.

Autism Spectrum Disorder:

Autism spectrum disorder (ASD) is a hidden developmental disability caused by differences in the brain [26]. According to the CDC, the prevalence rate for ASD among 8-year-olds in the United States is 23.0 per 1,000 children [27]. People with ASD can behave, communicate, interact or learn in different ways from the majority of the population. The behavior of people with ASD can vary significantly. Communication skills can range from excellent to nonverbal; some might need a lot of assistance in their daily lives, while others are entirely independent.

People with ASD can have difficulties traveling by air, finding the experience overstimulating due to bright lights, noises, screenings, and crowds [28]. Indeed, people with ASD can be under- or over-stimulated by touch, smell, noise, or light [29]. The cabin must be designed in a way that helps people with ASD. To help with over-stimulation by noise, the passengers will have access to a noise-canceling headset; for noise under-stimulation, extensive visual support to accompany any audio announcement (which is also required for accessibility). The cabin must be shielded from the exterior light, especially the rotor flicker, to help with light over-stimulation. The cockpit will be separated from the main cabin to block the light coming from the windshield. Passengers will be asked and warned before any contact to mitigate touch sensitivity. Seats should not have big seams or very textured fabrics.

Design considerations: Neutral colors, minimal textures, low ambient noise, pre-flight information.

Mental illness:

Mental illness is a broad term that encapsulates an extensive range of hidden disabilities. This report only addresses a few of them, but the team hopes that accommodations made for these mental illnesses will also benefit any other that passengers might have. Mental illnesses are “health conditions involving changes in emotion, thinking or behavior (or a combination of these)” [30]. One in five people in the United States, and one in four in the United Kingdom, are affected by at least one mental illness [31–33]. The main groups of mental disorders are mood disorders, anxiety disorders, personality disorders, psychotic disorders, eating disorders, and trauma-related disorders [34].

Mood disorders are a mental health class that health professionals use to broadly describe all types of depression and bipolar disorders [35], although bipolar disorders can be categorized differently [36]. Anxiety disorders are characterized by intense, excessive, and persistent worry and fear about everyday situations [37]. They can include obsessive-compulsive disorders (OCD) [8, 36]. Standing et al. performed a study subjecting participants to varying levels of noise and found that the group exposed to 75dB showed elevated levels of anxiety [38]; the cabin noise must therefore be lower than 70dB. Personality disorders refer to a long-term pattern of thinking, behavior, and emotion that is dysfunctional, extreme, and inflexible, including borderline personality disorders and obsessive-compulsive personality disorders [36, 39]. Psychotic disorders are severe mental disorders that cause abnormal



thinking and perceptions, like schizophrenia [34, 36, 40]. Eating disorders are associated with severe disturbances in people’s eating behaviors and related thoughts and emotions [41]. Trauma-related disorders are a group of emotional and behavioral problems that may result from childhood traumatic and stressful experiences [34, 42]. These include Post-Traumatic Stress Disorder (PTSD). People suffering from trauma-related disorders might benefit from the help of a service animal, which is discussed in a later section.

These disorders are usually treated with therapy and sometimes medication. By the recommendation of Anne Jannarone, Georgia Tech’s Office of Disability Services Director, the vehicle shall include resources so that passengers experiencing symptoms of mental illness in-flight might contact a professional during travel to ensure the safety of the passengers and the pilot. These resources shall be accessible by audio and visual interface. The cockpit shall have physical separation from the cabin to ensure the pilot’s safety during the flight.

Design considerations: Low ambient noise, pre-flight information, immediate counseling resources, cockpit-cabin separation.

Learning impairments:

Learning impairments are diverse and numerous. The most common learning disability is dyslexia, affecting 7% of the population [43].

Dyslexia is characterized by “difficulties with accurate and/or fluent word recognition and poor spelling and decoding abilities” [44]. Making sure all signs and written information is dyslexia-friendly can improve the flight experience for dyslexic people. Many dyslexia-friendly fonts have been developed to aid reading comprehension for people with dyslexia, like OpenDyslexic and Dyslexie. These fonts use Sans Serif, their letters that have sticks and tails (like b, d, p, q) vary in length, and they have ticker lines in parts of the letters – Dyslexie claims it “creates a visual center of gravity” in the letters to prevent them from “being turned upside down” [45]. While these fonts seem promising, multiple studies show they don’t increase reading speed or comprehension [46–48]. In fact, in a study comparing OpenDyslexic to Arial and New Times Roman, participants (both dyslexic and non-dyslexic) preferred Arial and New Times Roman to OpenDyslexic [47]. However, one aspect of these fonts does positively impact reading comprehension and reading speed: letter-spacing [48]. Increased inner-letter spacing improves texts’ readability, especially for people with dyslexia [49]. If the Arial font letter spacing is matched to that of the Dyslexie font, reading speed and comprehension increase similarly to when using Dyslexie [50]. It is not necessary to use a dyslexic-specific font To be dyslexic-friendly, but it is helpful to increase inner letter spacing.

Design considerations: Increased letter spacing in all written information.

Service Animals:

While the list of disability types is by no means exhaustive, one additional consideration that was explored was the use of service animals during flight. The ADA and the Air Carrier Access Act define a service animal as “a dog that is individually trained to do work or perform tasks for a person with a disability” [51, 52]. While some airlines allow emotional support animals (ESA) on board, this is no longer required by the Air Carrier Access Act. Indeed, ESA is no longer considered service animals by the U.S. Department of Transportation. While some people might benefit from having an ESA with them, these



dogs are not adequately trained to handle the unique stressors of air travel, resulting in unsafe situations for staff, passengers, and other dogs (especially service dogs) [53, 54]. The team decided only to allow service animals on board the vehicle as defined by the Air Carrier Access Act. Task-trained psychiatric service dogs are now considered service dogs, like those trained to assist people with PTSD [52, 55], and are therefore allowed aboard the vehicle.

Design considerations: Increased legroom, good aisle width.

3 Preliminary Configuration Selection

3.1 Customer Requirements

3.1.1 Design Objectives

The specific needs of passengers with disabilities and the requirements of the RFP are presented here as a list of design conditions, partitioned into two focus areas: cabin design and configuration design. These design objectives, and their definitions, are listed below.

Cabin Design Objectives:

- **Acoustics:** Maximum cabin noise level shall not exceed 70dB (similar to a dishwasher or a shower) throughout the duration of the flight. High noise levels can induce anxiety, headaches, and other ailments, especially among passengers with anxiety. A study by Zevitas et al. found that, out of a sample size of 200 planes, the median noise in airplane cabins was 84 dB [56]. Kim et al. found that elevated noise exposure and vibrations increased the risk of eyestrain and headaches [57]. Further, a study by Ashkenazi et al. showed that patients with migraines have a sound threshold that is 15dB lower than the average non-migraine patient [58].
- **Vibrations:** Vibrations shall be minimized for improved passenger comfort as vibratory loads can exacerbate spinal and head injuries, in particular. Kim et al. found that elevated noise exposure and vibrations increased the risk of eyestrain and headaches, with a maximum threshold of 140dB at 500 Hz [57].
- **Safety:** Safety of the cabin is critical in the design of the *Balto* due to the level of care that is required when transporting passengers with disabilities. The cabin design shall have enhanced crashworthiness. Seats shall be designed with energy absorption capabilities and increased storage for safety equipment and medical devices. Safety equipment, like seat-belts and life-vests, shall be stored during flight and easily accessible in case of emergency. Passengers traveling with mobility aids shall be able to access them in flight easily.
- **Reconfigurability:** Configuration of *Balto* shall be easily rearranged to account for a diverse range of disabilities. The cabin shall be self-contained and not require any external materials to switch between configurations. Priority shall be placed on the height of the cabin to ensure passengers with reduced mobility using mobility aids (e.g., crutches) and passengers with low vision and blindness can easily move around the cabin.
- **Passenger Accommodation:** Accommodations in pre-/post- and during flight shall include air conditioning, temperature-controlled storage (for medicine), easy access to carry-on(s), a noise-canceling cabin, special medical equipment (e.g., oxygen, electric plugs), and ergonomic seating.
- **Spaciousness:** Real and perceived volume of the cabin interior shall be maximized to ensure the comfort of passengers with reduced mobility. Furthermore, a large cabin volume minimizes the effects of claustrophobia-induced anxiety. Suppose a passenger with reduced mobility is traveling with a caregiver.



In that case, a spacious cabin enhances the mobility of the caregiver and provides them with ease of access to the passenger they support.

- **Ground-ops:** *Balto* shall be designed to ensure easy ground operations. Ingress and egress must be simple, especially for passengers with reduced mobility. Moreover, pre-flight checks and preparations shall be as effortless as possible. Wheelchair tie-downs shall be simple and fast.
- **Pilot Safety/Accessibility:** During the flight, the pilot shall experience minimal interference while also still able to communicate with passengers.

A summary of the cabin design objectives, and some of their implications for improving passengers' experience with disabilities, is presented in Table 3.1.

Design Objective	Disability Catered To	Design Accommodations
Acoustics	Low vision/blindness, mental illness (anxiety)	Low ambient noise
Vibrations	Reduced mobility	Minimal vibrations
Reconfigurability	Reduced mobility, low vision/blindness,	Seating for a caregiver,
Passenger Accommodation	Reduced mobility, low vision/blindness, hearing impairment, epilepsy, ASD, mental illness	Ramp access, audio/visual information, text-to-speech/speech-to-text, shield from outside flicker light, neutral colors, minimal textures, counseling resources
Spaciousness	Reduced mobility, low vision/blindness, ASD, mental illness, Service Animals	Ramp access, good aisle width, seating for a caregiver
Ground-Ops	Reduced mobility, epilepsy	Ramp access, short loading times
Pilot Safety/Accessibility	–	Physical cockpit/cabin separation

Table 3.1 Requirements to provide maximum comfort and safety to passengers with disabilities based on Design Objectives

Configuration Design Objectives:

- **Acoustics:** *Balto* shall have an acceptable perceived noise footprint to meet social and certification expectations in take-off, landing, and cruise. The acoustics shall have low transmissibility into the cabin. In addition to the comfort experienced by passengers onboard *Balto*, reduced noise levels are essential for public acceptance and reducing the level of noise pollution in urban areas where *Balto* will be operational. The noise footprint of *Balto* shall be no greater than 70dB, similar to Joby Aviation's noise footprint [2].
- **Vibrations:** *Balto* shall have low vibrations to minimize fatigue, lifecycle cost, and maintenance cost. The vibrations shall be at a safe limit for the pilot and have low transmissibility into the cabin.
- **Hover Performance:** Hover and axial flight shall require low power demand and have good stability and control capabilities.



- **Cruise Performance:** *Balto* shall minimize best range power and maximize best range speed. The team chose to reduce the best range over best endurance to be more closely tailored to the needs of a passenger aircraft. Turn rates and bank angles shall be kept low to diminish the resulting forces experienced by disabled passengers.
- **Safety:** Importance is placed on minimizing the risk of life and property for the operators and bystanders of the vehicle. Redundancy shall allow the vehicle to maintain control and perform a safe landing in case of the loss of one rotor or a single point failure.
- **CG Travel:** The CG envelope shall be large enough to allow mobility of passengers and caregivers without loss of stability in flight.
- **Feasibility/Mechanical Simplicity:** The technology used shall be readily available and certified. *Balto* must be manufacturable.
- **Compactness:** Cabin volume shall be maximized while also keeping the landing footprint suitable for a helipad – which will be the most constrained landing location – and also maintaining maneuverability within the constraints of an urban environment.
- **Cost:** The configuration shall use technology and materials that are cost-effective for manufacturing, operation, and maintenance.
- **Compatibility with Electric Propulsion Technology:** The electric propulsion system shall be easily implemented. Batteries on the vehicle shall be accessible, rapidly swapped on the ground for high turn-over time, and shall be in a safe storage location during flight.

3.1.2 Analytical Hierarchy Process (AHP)

AHP matrices were used to determine the weight of each design objective for the cabin and configuration, respectively. The analysis entailed weighing each design objective relative to the other design objectives (shown in the vertical columns). The scoring weights are:

- $1/3$ for “much less important”
- $1/2$ for “less important”
- 1 for “as important”
- 2 for “more important”
- 3 for “much more important”

The average of all team members’ inputs comprised the final AHP results. The standard deviation was confirmed to be low for all scores.

The cabin’s final weight and the configuration design objectives, and their respective rankings from the AHP are shown in Figures 3.1 & 3.2, respectively. For both, the most crucial factor is safety. Most urban air taxi designs consider safety to be vital, but it is of even greater significance when transporting people with reduced mobility. Similarly, pilot safety is the second most essential design objective for the cabin, especially since the vehicle will be designed for a single pilot. Mechanical simplicity, CG travel, vibrations, and ground operations were all ranked as important factors in the selection of the configuration as they all have significant impacts on the effectiveness of the vehicle at performing the desired tasks. CG travel allows versatility in the number and placement of components in the cabin without altering the vehicle’s stability. The team strongly emphasized CG travel, as people with disabilities may require large and heavy pieces of medical equipment to be stored onboard. Limiting vibrations also ensures the comfort and health of passengers, which is critical because people with disabilities and reduced mobility may have underlying injuries that significant vibrations could exacerbate. As the RFP calls for the design of an air taxi, it is necessary to ensure that the ground operations occur in a fast and effective manner such that the maximum safe number of flights that can be performed are not constrained by excessive amounts of time spent on the ground performing pre-flight and post-flight tasks. Spaciousness was considered to be the least consequential



of all cabin design objectives. While the eventual assistant passenger should be able to move around the cabin to help the passenger with reduced mobility, the cabin's spaciousness should not come at a cost to any other design priorities. Because most of the mission will be spent in cruise, the latter's performance is ranked after safety for the configuration, and hover performance is ranked last, as a minimal amount of time will be spent in hover.

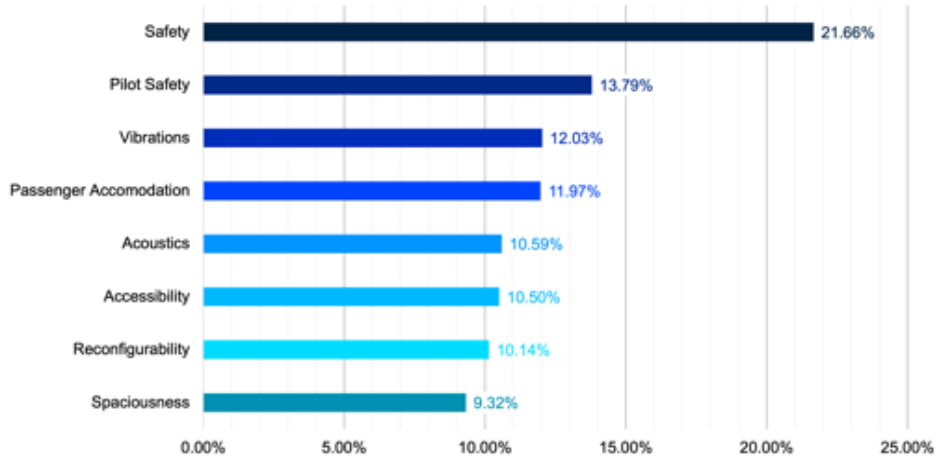


Figure 3.1 Weights and ranking of cabin selection objectives

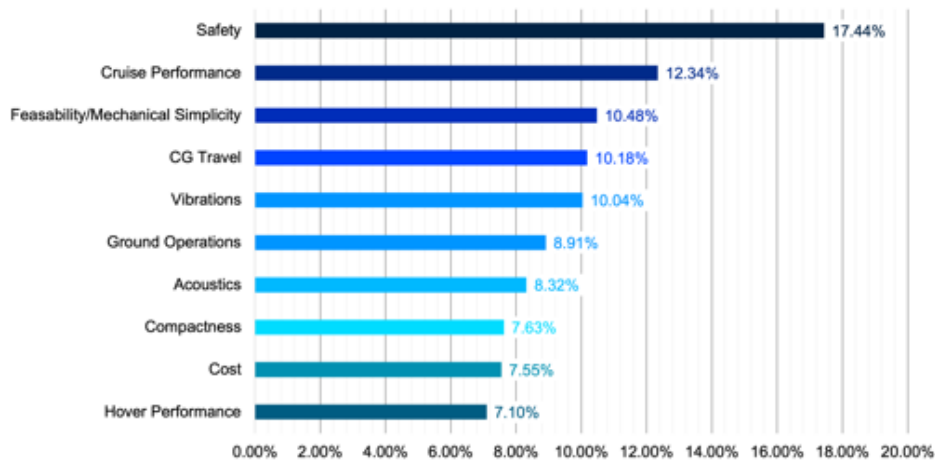


Figure 3.2 Weights and ranking of configuration selection objectives

3.2 Configurations Considered

The team qualitatively compared 12 configurations – illustrated by examples in Figure 3.3 – using a Pugh matrix to evaluate the design objectives presented previously. Each configuration was weighted against a baseline multirotor configuration (set with a score of 0). The multirotor was used as a baseline as most UAM concepts use more than one rotor in their designs (e.g., 2, 59).

Integer scores between -3 and 3 were given to each configuration, where -3 is “performs much worse than a multirotor for this design objective,” and 3 is “performs much better than a multirotor for this design objective”.

Brief descriptions of each configuration considered, with their qualitative advantages and disadvantages, are given below:





Figure 3.3 Configurations considered (from left to right, top to bottom: from Refs. 60–71)

- **Multirotor (four or more separated rotors that provide both lift and propulsion):** With at least four individual rotors used, multirotor are very efficient for vertical flight. Primarily, the addition of rotors implies that the blade tip speed need not be as high as a single main rotor, significantly reducing noise levels. Multirotors can reduce –or eliminate– the need for cyclic and collective controls, removing the weight and complexity of swashplates. Controls can be achieved with differential thrust instead. Multirotors also provide redundancy in case of failure: rotors can be designed for more than the required thrust to compensate if a critical component fails. Finally, multirotors have a good maneuverability capacity.
- **Single Main Rotor (one main rotor for lift and propulsion, and one tail rotor for anti-torque):** While the mechanical simplicity of this configuration is higher than for a multirotor, other factors might be less ideal for this mission. While this is a safe configuration for traditional transportation missions, allowing for autorotation in case of engine failure, this mission requires the ability to safely land in case of loss of one engine or one rotor. Moreover, autorotation alone is not ideal for passengers with some forms of disabilities as the landing can involve rapid maneuvers.
- **Coaxial Rotor (two vertically separated counter-rotating rotors for both lift and propulsion):** The coaxial is an improvement on the single main rotor, having two counter-rotating rotors placed on top of each other, which provides better hover capabilities than the single main rotor and eliminates the need for a tail rotor. However, this can also reduce the center of gravity envelope. The rotors and rotor hub design and maintenance complexity are vastly increased. Hover performance is of low priority in the design objectives, reducing the importance of the main advantage of the coaxial configuration.
- **Compound Coaxial (coaxial rotor with added structures):** Such an aircraft seeks to improve on the coaxial configuration by adding wings or similar structures to improve the cruise characteristics of the coaxial configuration. The added feature may reduce hover performance due to the added structure and increased weight but contributes to better cruise control characteristics. However, the issues existing with the coaxial configuration are still a factor for this configuration, making it suboptimal for this mission.



- **Tandem Rotor (two horizontally separated counter-rotating rotors for both lift and propulsion):** In most configurations, tandem rotor configurations have two axially placed rotors separated horizontally, also varying in height in most cases. While such a design does increase the center of gravity envelope (compared to the single main rotor), it is only in one direction, unlike the multirotor. Furthermore, any rotor failing is a single point failure which is not ideal for the mission. The rotor placement relative to the cabin is helpful for the boarding and deboarding of passengers. Still, its design can require a larger cabin/fuselage, which will make it harder to implement given the size constraints.
- **Tilt-Rotor (two or more rotors that can tilt independently, allowing the rotors to be used for both vertical lift in hover and propulsive rotors in forward flight):** The mission in consideration has a significant portion of cruise. In such regimes, it is a well-proven fact that wings perform much more efficiently than rotors. Thus, less power may be needed in cruise, reducing the acoustic levels. Note that there is a weakness in hover due to the presence of the wing and the interactions that will create a less effective aircraft, but it makes up for the hover performance in the cruise phase. There is the added complexity of the rotating nacelle both mechanically and from a controls standpoint.
- **Tilt-Wing (two or more rotors that can tilt with the wings for forward flight during which wings provide lift and rotors provide propulsion):** The tilt-wing is a slight modification on the tiltrotor by having the entire wing rotate from hover to cruise rather than just the rotor nacelle. Note that this design slightly improves hover characteristics while maintaining the same cruise efficiency (as compared to a tiltrotor). However, there is the added cost involved with the increased structural complexity of rotating the entire wing, which may also contribute to some additional vibrations. Despite the slight downsides, it does offer enough positives to be one of the configurations considered for further analysis
- **Intermeshing Rotor (similar to coaxial rotor configuration but the rotors are angled sideways):** Intermeshing the rotors do increase performance from the coaxial since the larger disk area and better aerodynamic interactions between the two rotors, results in better lift and hover characteristics. It also maintains the advantage of not requiring the tail rotor. However, such a configuration does have a low forward flight speed which is not beneficial to this mission. Furthermore, there is added mechanical complexity and challenge in controlling the aircraft should one of the rotors fail.
- **Tail-Sitter (take-off and landing on the tail, then tilts horizontally in flight):** Unlike other configurations, the tail-sitter has a vertically-oriented fuselage. It takes off and lands on its tail, then pitches down 90° in forward flight. It often has better cruise characteristics than tiltrotor or multirotor configurations. However, this mission requires few, if any, attitude changes, and tilting the fuselage on landing and take-off is not ideal.
- **Rotor-in-Wing (rotors providing both lift and propulsion are embedded in the wings):** The rotor-in-wing aircraft is designed as an airplane, with rotors embedded in the wings to provide axial flight and hovering capabilities. The rotors are mounted on a tilting mechanism to provide propulsive forces in forward flight. Since the rotors are encased in a fenestron-like structure, they are quieter than traditional rotors. Their design is more complex than conventional rotors, as vibrations could cause the blades to collide with the encasing fenestron.
- **Multirotor thrust and lift compounded (multirotor configuration with added wing and/or propellers for forward flight):** This configuration seeks to combine the advantages of fixed and rotary-wing aircraft without the added complexity brought by tilting mechanisms in the tilt-wing or tiltrotor configurations. The hover performance is similar to that of the multirotor, although the wing adds drag in axial flight. The wing increases the forward flight performance, and propellers might provide propulsion in forward flight. This configuration provides a large CG travel envelope similar to the multirotor configuration and does not present any single-failure points. Due to the support structures required for the rotors, these configurations can be heavier than others considered.



- SMR thrust and lift compounded (SMR configuration with added wing and/or propellers for forward flight):** With wings and propellers added to a traditional single main rotor configuration, the SMR thrust/lift compound configuration is one of the least complex designs for vertical flight aircraft. Both propeller aircraft and single main rotor aircraft are known and trusted designs. The main rotor can be slowed down in forward flight to reduce drag, and propulsive force can be obtained from propellers on the wing. This configuration provides both autorotation and gliding capabilities in forward flight, making it safer than other configurations. However, gliding is not possible in hover, and the only safety measure would be autorotation. Good autorotative performance in hover requires a large rotor, which leads to increased weight and significant aeroelastic effects.

The Pugh matrix results are summarized in Figure 3.4. Five configurations had very similar scores: the tilt-wing, the multirotor, the SMR compound, and the multirotor compound. The other configurations considered were more than two-tenths of a point away from the baseline configuration, the multirotor. The multirotor thrust and lift compounding configuration, the single main rotor thrust and lift compounding configuration, and the tiltrotor configuration were selected to perform a preliminary vehicle sizing to choose the final configuration.

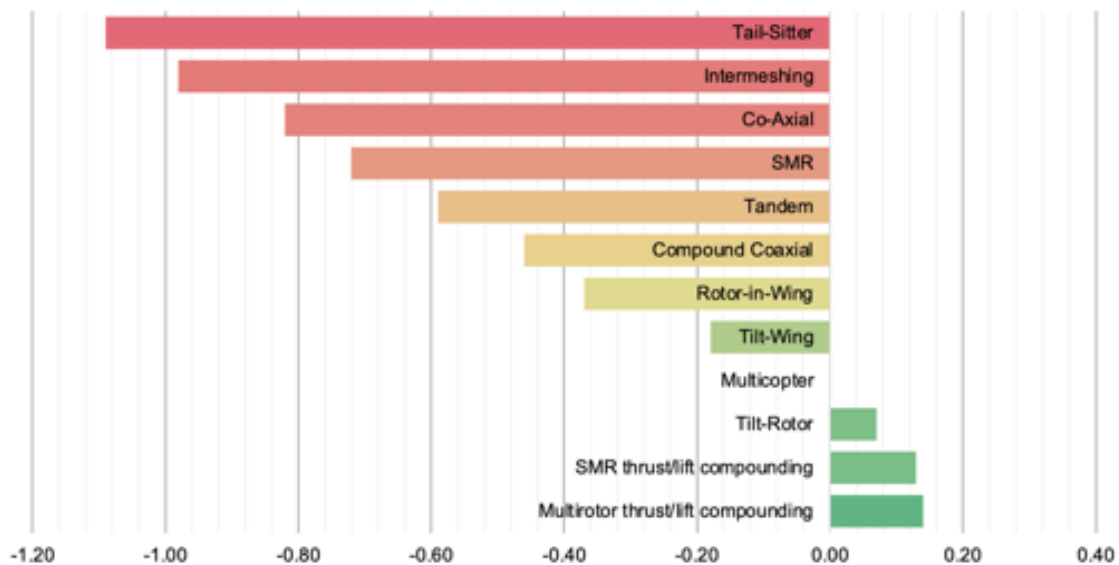


Figure 3.4 Pugh Matrix Results with respect to the multicopter

3.3 Vehicle Sizing

3.3.1 Methodology

After the preliminary configuration selection using the Pugh Matrix in Section 3.2, the team had three configurations to study to determine which one was best suited for the mission: the multirotor thrust and lift compounding, the SMR thrust/lift compounding, and the tiltrotor. The team used an in-house analysis code, SLSS, to perform the preliminary sizing of these configurations and the SMR for validation and select the final configuration.

The code is based on momentum theory and equations derived in Refs. 72–77. Detailed equations will not be given for brevity, but the overarching procedure is explained below and summarized in Figure 3.5.

Weight-Energy Balance:

Weight is one of the primary design considerations, so a weight energy balance model was included using a bisection code. Initial inputs for the upper and lower limits for the gross weight are made, and an initial



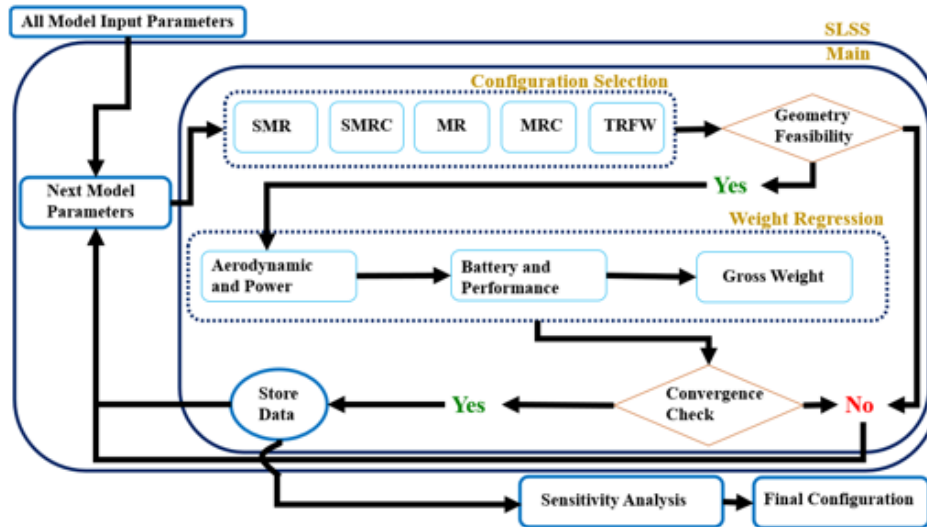


Figure 3.5 SLSS General Calculating Algorithm

estimate of the gross weight is typically chosen as the middle point between upper and lower bounds. Note that since the payload and the empty weights are fixed, the only estimate is the available battery weight. The aerodynamics and power requirements of the configuration of interest are calculated to obtain the required battery weight. Details on the required battery weight calculation are given in a later paragraph. Comparing the battery weight available and required, the bisection bounds are changed depending on if the weight estimate is too small or large. This process is repeated until the available battery weight equals the required battery weight. In some cases, a specific vehicle model is unable to converge. In that case, the model is rejected, and the algorithm moves on to the next one.

Checks were also added to the code to ensure those vehicle models fit the RFP requirements, such as ensuring that it fits within fifty feet by fifty feet box.

Power required calculations:

The aerodynamics and power requirements of the various configurations considered are calculated differently depending on the vehicle model. For the traditional SMR, using momentum theory and the estimated weight, the coefficient of thrust, inflow coefficient, approximate flat plate drag, and power coefficient – among other parameters – are calculated for a range of freestream velocities, covering both hover and forward flight. The power required with respect to forward velocity values is obtained and passed to the required battery weight computation. This SMR case was used to validate the SLSS code, as shown in Figure 3.6. The other configurations follow a procedure similar to the SMR to obtain the required power, but it is modified to fit each configuration. For the multirotor, the number of rotors is changed from one to a discrete number, $n \geq 2$. For simplicity, interactional effects between rotors are not taken into consideration. The SMR compound and multirotor compound configurations add complexity, including a wing and propellers in forward flight. The aerodynamic components of the wing are obtained from fixed-wing performance analysis [79]. The calculations for the aerodynamic properties remain the same as for the SMR and the multirotor in hover. The propeller power required to travel at the given forward speed is calculated first in forward flight. When the

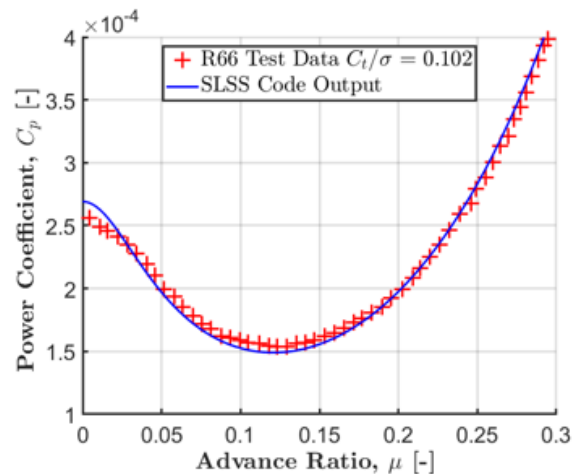


Figure 3.6 SLSS Results for the SMR compared to Ref. 78



propellers are in use, the wing's lift is computed assuming a blown wing, i.e., the effects of the propellers' wake on the wing (without swirl). The power required for the rotors is calculated from the estimated gross weight minus the lift provided by the wings. The rotors do not contribute to any forward flight velocity for this configuration. The sum of the power required by the propellers and the rotors is used to obtain the final power required with respect to forward speed values for the compound configurations.

Finally, the tiltrotor configuration, with a fixed-wing, requires the addition of the tilt of the rotors in the transition from hover to forward flight.

For simplicity, it is assumed all rotors tilt. The rotor tilt is computed at every forward speed, and the power is calculated from momentum theory for forward speed. The effective climb is also considered to ensure that the forward speed and required thrust are satisfied.

As for the compound configurations, the downwash of the rotors on the wings is estimated and included in the wing lift calculations.

Parameters considered:

For each configuration, multiple parameters were varied.

Using a medium-fidelity CFD software, Solidworks, then confirmed with a higher fidelity CFD software, the flat plate drag area was determined to be 0.5 m^2 (5 ft^2) for the initial fuselage, without wings or rotors. This analysis was applied to all configurations. The empty weight fractions were obtained from historical data and do not include battery weight, as fuel weight is not included in the historical data. The lift curve slope was kept constant for all blades and wings, and – when applicable – the wing angle of attack was held at 3 degrees, and the wing aspect ratio was varied. The blade tip speed, blade chord, rotor twist, number of blades, and number of rotors were varied for all configurations. For all but the tiltrotor configuration, the rotor radius was varied. The rotor radius was not varied for the tiltrotor, as the number of rotors and wing aspect ratio is used to determine the rotor radius. Overall, the code analyzed over one million configurations.

Required battery weight calculation:

The power required obtained for each model can be used to compute the required battery weight. The battery specifications used are given in Section 12.1. The majority of the mission is in cruise; for simplicity, it is assumed the vehicle is in cruise for the entire mission for the battery weight calculation. The mission time was varied from zero to three hours, with a fixed distance required by the RFP. The corresponding mission velocities are correlated to the required power values found for each model. The required power is then converted into energy needed, which determines the battery weight based on the mass-energy density of 400 Wh/kg given in the RFP. The range [80,81] and endurance of the vehicle are computed using the battery weight. The battery weight is fed back into the weight regression model.

3.3.2 Results

The SLSS code evaluated nearly ten million vehicle configurations, defining one hundred thousand that successfully converged as potential configurations for the mission. The output information included the power curve, geometrical parameters, and performance metrics of the converged configurations, including gross weight, mission time, disk loading, power loading, range, endurance, and energy requirements.

The performance metrics and additional empirical parameters were then utilized to create a Pugh matrix to evaluate and assess these configurations. The empirical parameters included potential redundancies in vehicle configuration, design complexity,

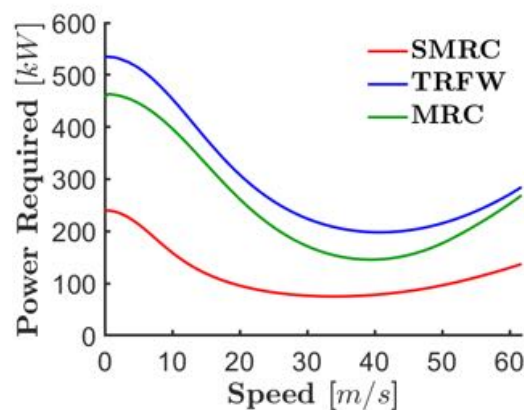


Figure 3.7 Power curve results from SLSS for final three potential configurations



manufacturing feasibility, and maintenance costs. The Pugh analysis reduced the potential configurations to three final configurations, which are described in Section 5: a single main rotor with compounded lift (SMRC), a tiltrotor (TR), and a multirotor with lift compounding (MRC).

The power curve for the three configurations is shown in Figure 3.7. The vehicles are compared in detail in Section 5.

4 Analysis Tools

To complete the design of the aerodynamic components, the team took a multi-fidelity and multi-objective approach in order to account for all the required variables. The team employed various in-house built codes and off-the-shelf solvers to complete the design; these are described in the following section. All methods have been validated with at least once similar configuration by the team to ensure accuracy. These are not shown due to page limitations.

4.1 GTsim

For highly separated and viscous numerical simulations, an in-house high fidelity computational fluid dynamics (CFD) solver, GTsim [82] was applied. GTsim employs a finite volume (cell-centered) formulation with fourth-order spatial and second-order (Backward Differentiation Formula) temporal discretization schemes in a block structured approach to ensure high accuracy. A variety of turbulence closures are available; for this effort the unsteady Reynolds-Averaged Navier-Stokes (URANS) simulations utilized the $k\omega$ -SST turbulence model [83]. The solver includes the ability to resolve the incompressible and compressible Navier-Stokes equations; here, the compressible equations were solved. GTsim has been extensively validated with experimental data and correlated with extant comparable solvers for a full suite of canonical flows [82]. The tool was used to obtain the aerodynamic characteristics of the chosen airfoils. The team has significant experience with this solver for airfoils and wings [84].

4.2 S&D BEMT

For the design of the rotary wing components, the S&D BEMT code was a self-developed in-house based on the blade-element momentum theory (BEMT) model outlined by Leishman [72] and Johnson [74]. The BEMT code was designed to be parametrizable with the design variables outlined by the RFP. The code was validated against experimental data presented by Ramasamy [85]. The validation is shown in Figure 4.1. The code does not apply small angle approximations in its calculations so that it can account for the effects

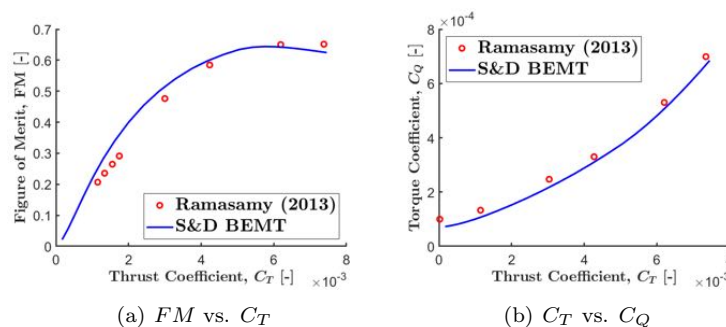


Figure 4.1 S&D Validation against Experimental Data

of high twist angles at the low tip speeds outlined by the RFP. Additions to the code include estimation of the induced power loss factor and the Prandtl tip loss factor as outlined in Johnson [74]. Therefore, the



code provides a more realistic estimation for lower aspect ratio rotors that usually have higher induced loss factors than the 15% standard for regular rotors [72]. The induced power loss factor is a function of the chord at $0.7\%R$ over the blade radius, causing the lower aspect ratio blades to have much higher loss factors.

4.3 XFOIL

XFOIL [86] is a low-fidelity aerodynamics solver used for 2D analysis of airfoils. While the results are less accurate than a high-fidelity software, general trends can be captured when selecting an airfoil for blade or wing design. XFOIL was used for the initial selection of airfoils for the wing (section 10) and the rotating blades (section 9).

4.4 AVL

AVL is an extended vortex lattice model software developed by Mark Drela and Harold Youngren [87]. It is used for the aerodynamic and flight-dynamic analysis of wings and rigid aircraft. It was used to select the planform size and shape for *Balto's* wing (section 10).

4.5 FlightStream

FlightStream is a medium-fidelity vorticity panel method software developed by Darcorp [88]. It is able to analyze varying flight conditions, propeller and wing loads and wakes, and aerodynamic forces and moments. FlightStream is additionally able to perform acoustic analysis. The run-time of FlightStream is significantly shorter than high-fidelity solvers, and has good correlations with experimental data.

FlightStream was validated using the ROBIN fuselage. The aerodynamic coefficients obtained with FlightStream were compared to those obtained experimentally by Schaeffler et al. [89]. The fuselage drag was found to have an error of 7.2% when compared to the experimental values. This error was deemed acceptable for a medium-fidelity solver.

FlightStream was used to analyze the aerodynamic properties of the fuselage (section 8), the wing (10), and the full vehicle (6).

4.6 ANSYS AIM 19.1

ANSYS AIM, a commercial Finite Element Analysis (FEA) software suite, was applied to perform structural and fatigue analysis [90]. ANSYS AIM was employed to design and evaluate *Balto's* airframe (section 11.3), wings (section 11.4), and landing gear (section 11.5). Moreover, the software was used to perform a fatigue analysis on the rotating shafts of the lifting rotors and the cruise rotors (section 11.6).

5 Preliminary Vehicle Sizing

From the results obtained in Section 3, the team designed three configurations: a single main rotor lift and thrust compounding (SMRC), a tilt-rotor (TR), and a multirotor thrust and lift compounding (MRC). The approximate sizing for each vehicle was obtained from SLSS (see Section 3.3.2), which provided insight into the wing sizes, rotor sizes, and a performance metrics the vehicle is required to match in order to successfully finish the mission. These are explored in further detail in this section to arrive at final configuration geometry and performance.



5.1 SLSS Results

The converged configurations obtained from the SLSS code are presented in Table 5.1, and each configuration's parameters were used to refine the designs.

	SMRC		TR		MRC	
	SI	English	SI	English	SI	English
Gross Mass	2616 kg	5766 lb	3172 kg	6994 lb	2448 kg	5397 lb
Cruise Speed	44.4 m/s	86.4 kts	53.0 m/s	103.0 kts	44.4 m/s	86.4 kts
Cruise Drag Area	0.71 m ²	7.60 ft ²	0.78 m ²	8.36 ft ²	0.68 m ²	7.35 ft ²
Mission Time	62 min	62 min	53 min	53 min	62 min	62 min
Cont. Power Hover	560 kW	751 HP	560 kW	751 HP	107 kW	143 HP
Cont. Power Cruise	246 kW	330 HP	-	-	107 kW	143 HP
Cont. Torque Hover	2820 N-m	24959 lb-in	2820 N-m	24959 lb-in	250 N-m	2213 lb-in
Cont. Torque Cruise	480 N-m	0 lb-in	-	-	250 N-m	2213 lb-in
Total Mission Energy	122 kW-hr	164 HP-hr	282 kW-hr	378 HP-hr	215 kW-hr	288 HP-hr
Reserve Battery Mass	70.0 kg	154 lb _m	190. kg	419 lb _m	127 kg	280 lb _m
Total Battery Mass	305 kg	673 lb _m	705 kg	1554 lb _m	537 kg	1184 lb _m

Table 5.1 Parameters obtained from the SLSS results for the three selected configurations

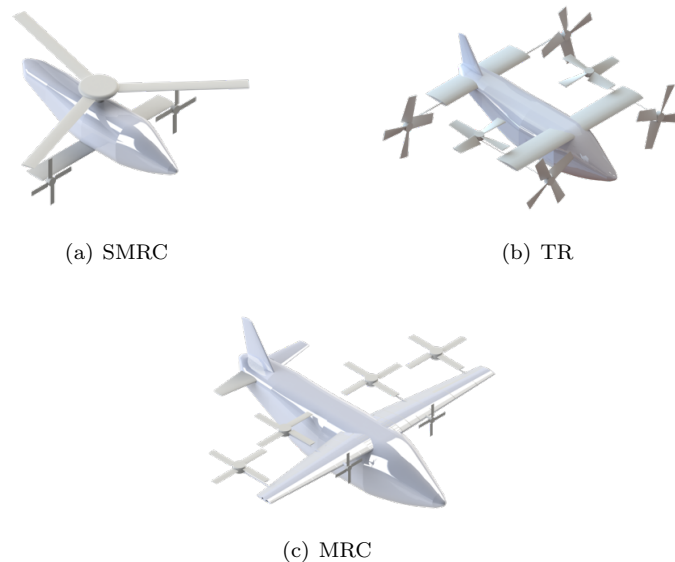


Figure 5.1 Preliminary design of the three selected configurations

The SMRC (Figure 5.1 (a)) has a single main rotor placed above the fuselage. The propellers are placed along the wing at an even spacing. The propellers are placed away from the fuselage to prevent interactional effects between the propeller wakes and the fuselages, and to ensure they are not in the wake of the main rotor. A tail is added at the empennage to provide control surfaces, as there will be no tail rotor, unlike what can be seen in traditional single main rotors. This configuration is comparable to the slowed rotor concept developed by Carter Copter.

The TR (Figure 5.1 (b)) has a long wing span and a large rotor radius, which would make a single wing be longer than the required 15.24 m (50 ft) box limit stated by the RFP. The wing span was divided into two wings, which simplified the rotor tilting process and improved the weight distribution across the vehicle. The main wing has four rotors: two tilting rotors at the wing tips, and two non-tilting rotors between the tip and the fuselage. The second wing has two tilting rotors at its tips, and will act as a tail.



The MRC (Figure 5.1 (c)) has the maximum number of lifting rotors distributed along the wing, which also has cruise propellers distributed along its span. A tail is added for control purposes.

5.2 Rotor Design Goals

An effective rotor design starts with a good airfoil selection. Depending on the use case, whether it is for hover efficiency or propulsive efficiency, understanding the aerodynamic provided by the airfoil and its corresponding aerodynamic coefficients is of the utmost importance. The following selection outlines the process of rotor blade design. While a more detailed methodology is shown in Section 9.1 for lifting rotors, and Section 9.2 for cruising propellers, a more concise description is presented here to avoid repetition due to the page limitation.

For all the configurations studied in this trade study, the rotor blades operate at an average Reynolds number of 3.5 million. Airfoil thickness is selected depending on the application of the airfoil. While small thickness-to-chord ratios can be detrimental to the aerodynamic efficiency due to their abrupt stall, this does not apply to our flight regime of low Mach numbers thorough the rotor disk. Airfoils are compared, and the selected airfoil must have a high C_l/C_d , low C_m magnitudes, and not present an abrupt stall.

Once the airfoil is selected, the blade planform has to be defined. For low Reynolds numbers and low Mach number, a blade sweep does not present any advantages. Taper can be applied, but since the rotors studied here do no operate in the transonic region, the effect of taper is limited.

The effects of twist are also studied, to ensure optimum aerodynamic efficiency across the rotor disk.

5.3 Rotor Design

	SMRC		TR		MRC	
	SI	English	SI	English	SI	English
Rotor Blade Chord	0.76 m	2.5 ft	0.61 m	2.0 ft	0.61 m	2.0 ft
Rotor Blade Tip Speed	121.92 m/s	400 ft/s	121.92 m/s	400 ft/s	158.50 m/s	520 ft/s
Rotor Blade Twist	0 deg	0 deg	-30 deg	-30 deg	0 deg	0 deg
Rotor Blade Radius	7.32 m	24 ft	1.52 m	5 ft	1.22 m	4 ft
Propeller Blade Chord	0.21 m	0.7 ft	-	-	0.61 m	2.00 ft
Propeller Blade Tip Speed	121.92 m/s	400 ft/s	-	-	158.50 m/s	520 ft/s
Propeller Blade Twist	0 deg	0 deg	-	-	0 deg	0 deg
Propeller Blade Radius	1.22 m	4.0 ft	-	-	0.99 m	3.25 ft
Number of Rotor Blades	3 blades		4 blades		2 blades	
Number of Rotors	1 rotor		6 rotors		4 rotors	
Number of Propeller Blades	4 blades		-		4 blades	
Number of Propellers	2 propellers		-		2 propellers	

Table 5.2 Rotor characteristics for each configuration

The following subsections are dedicated to the comparison of performance metrics across the three selected configurations. Based on the RFP request, an emphasis is placed on the thrust coefficient vs. Torque coefficient across the design space, but other important design parameters like disk loading, figure of merit and propulsive efficiency are also considered. The following discussion is separated into subsections referencing the three configurations to avoid confusion. To avoid repeatability and ensure compactness of the report, the methodology followed is the same as the one followed in Chapter 9. In addition, the propeller comparison is only discussed in the multirotor compound to avoid repeatability of content.



5.3.1 Single Main Rotor Compound

The initial sizing code outlined a single main rotor compounded with thrust and lifting components. The initial design called for a rotor radius that maximizes the area over the footprint. To understand the sensitivity of performance (defined as C_T/C_Q) parametric studies were done on the effect of spanwise twist on the figure of merit, the effect of rotor radius and the effect of outboard taper. The results of this study is outlined in Figure ...

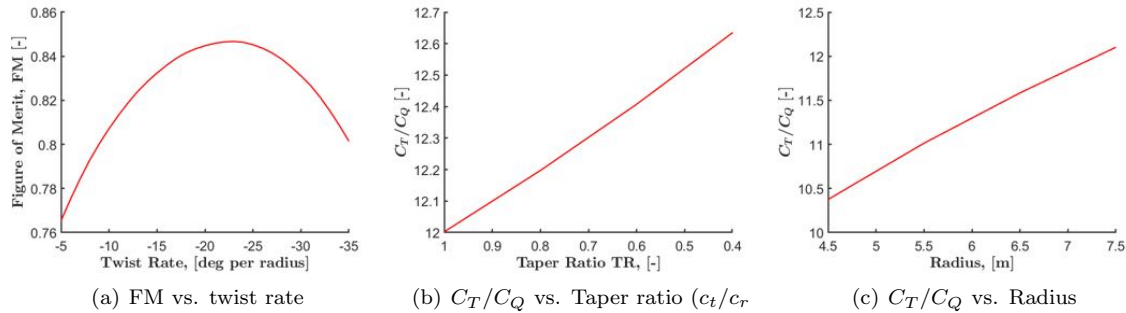


Figure 5.2 Single Main Rotor parametric study

The parameter that has the most effect on hover efficiency (FM) is the twist rate over the span. Adding twist, the inflow approaches its ideal state, therefore increasing the aerodynamic efficiency. Figure 5.2 (b) depicts the effect of taper ratio, as the taper ratio increases the C_T/C_Q increases linearly. The effect of taper is relatively low due to the low Reynolds number and local Mach number. Figure 5.2(c) shows that increasing the radius also increases the C_T/C_Q parameter due to the reduction of induced velocities along the disk. Through this analysis, the ideal configuration for the SMR compound features a maximized rotor radius, a twist of about 20 degrees across the span, and no taper ratio. The adverse effects of a large rotor in forward flight are not included as the configuration relies on its wing for lift and pusher propellers for propulsive force.

5.3.2 Tilt-Rotor

The tilt-rotor presents with a unique design challenge, the design of a rotor that is efficient in both hover and forward flight. This is a complicated design challenge as both flight regimes are completely different. In hover, the rotor experiences shallow inflow angles while in cruise they are extremely high. Twist is the predominant feature on the design of these types of rotors, the cruise requires a high twist rate while the hover shallow ones. Figure 5.3 presents the trade studies done to understand the parameters that affect both the propulsive efficiency and the figure of merit.

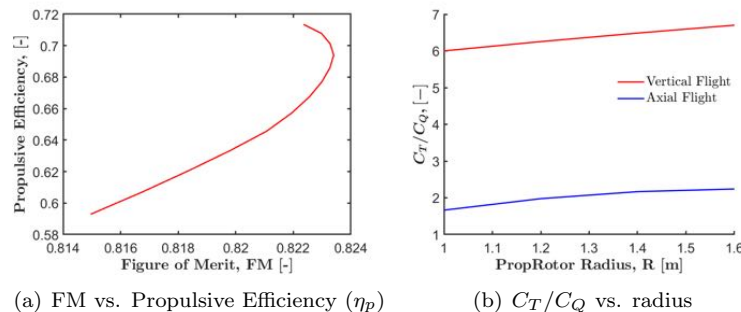


Figure 5.3 Tilt Rotor Parametric Study



Figure 5.3 (a) demonstrates the comparison between the propulsive efficiency and the hover figure of merit by varying twist. The medium-high twist rates (35 - 40 $deg/span$) presented the highest figure of merit while still exhibiting good propulsive efficiency. In Figure 5.3 (b) the effect of radius on the C_T/C_Q is studied; for the cruise regime the C_T and C_Q were non-dimensionalized in the rotor nomenclature. Increasing the radius of the prop-rotor also increased the C_T/C_Q in a linear fashion. The ideal configuration for increased performance on the tilt-rotor presents a high twist rate and a radius close to 1 m (3.2 ft).

5.3.3 Multirotor Compound

The multirotor compound features an even number of lifting rotors for the hover configuration and lift+thrust compounding for the cruise regime. For conciseness of the report, the effects of the twist and radius explored in the single main rotor compound section will be re-stated. The SLSS code outlined many configurations of lifting rotors so the effect of increasing the number of rotors was explored. The trade space was limited to 6 lifting rotors and above due to controllability and stability issues encountered with multirotors with fewer rotors.

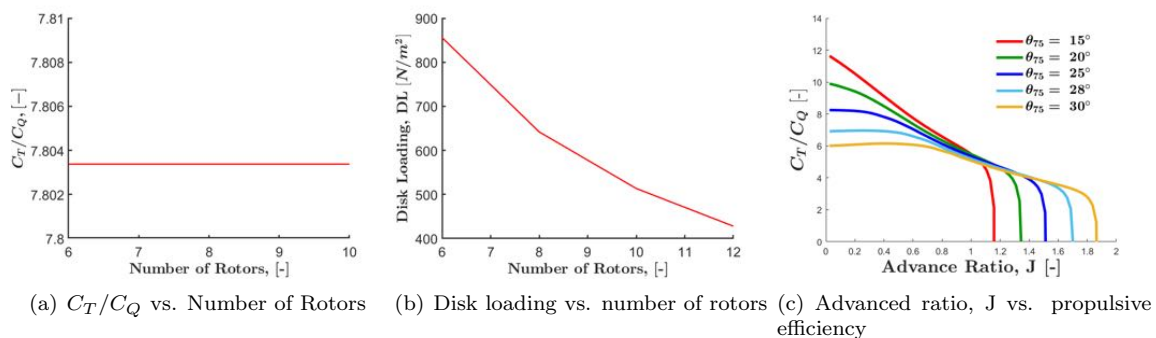


Figure 5.4 Multirotor Compound parametric study

Figure 5.4 (a) indicates that adding rotors does not change the C_T/C_Q experienced by the blades. To add to the analysis, Figure 5.4 (b) shows the effect that the number of rotors have on disk loading. More rotors exhibit a lower disk loading therefore they exhibit a better hover performance due to reduced inflow angles. The study of propellers was also of paramount importance as both the multirotor compound and the compounded single main rotor rely on them for propulsive force. The SLSS code outlined similar propeller sizes, therefore the analysis in Figure 5.4(c) is valid for both configurations. In Figure 5.4(c), the C_T/C_Q can be maximized by adding a variable pitch mechanism effectively extending the operational envelope. The optimal design for this configuration would feature eight lifting rotors with two large tractor propellers.

5.3.4 Comparison of Relative Advantages and Disadvantages of Each Rotor Configuration

The previous subsections analyzed the trade space for the three main configurations being studied: Compound Single Main Rotor, Tilt-rotor, Compound Multirotor. This section focuses on highlighting the pros and cons on each configurations.

Compound Single Main Rotor:

The compounded single main rotor design provides with excellent hover performance and low power consumption during hover. This is because the large main rotor exhibits lower disk loading than its competitors. While the configuration has great hover capabilities, the large rotor can become a penalty in forward flight. This configuration could have large flapping as well as significant aeroelastic characteristics. These adverse effects are reduced by the introduction of the tractor propellers and wing for lift offset. Even in that case, the rotor will introduce a large drag penalty. From the baseline performance metric of this study, C_T/C_Q ,



the configuration is superior, featuring a ratio of about 12 while the others feature a value in the 6-8 range. From a safety perspective, this configuration provides the best gliding and autorotative capabilities due to its large rotor, but the main concern is the operation in the dead-man zone. A failure during hover will inevitably result in a hard crash-landing which is not an option for the type of passengers that this vehicle is designed for.

A report by Floros and Johnson [91] details a comprehensive analysis done on the slowed rotor configuration. It was found that, for the slowed rotor concept, higher values of collective pitch values were needed to achieve the minimum power required [91]. During all flight, *Balto* the floor of the vehicle is kept level to ensure the comfort of passengers. A higher value of collective pitch as needed by the slowed rotor concept, however, does not warrant a comfortable flight for persons with reduced mobility. If lower value of collective pitch were maintained, then the power required would be too great.

Tilt Rotor:

The tilt-rotor configuration offers the best of the aircraft and the rotorcraft world in one vehicle. Unlike the other configurations, the tilt-rotor uses all its components in all stages of flight. In hover the rotors are positioned in the optimal position for vertical flight while in cruise, these tilt and provide the propulsive force. This is a very clean design as none of the components are operate for only a single mission segment. This new tilt-rotor configuration minimizes the hover download over the wing and the fuselage by moving the rotors beyond the wing. While this configuration has great advantages, it also has disadvantages that overshadow the mission's application. The main issue is the added complexity of the design, having multiple tilting mechanisms that are cycled every flight adds to the failure points and the energy requirements during transition. The transition portion of the tilt-rotor introduces vehicle motion that may cause discomfort to the reduced mobility passengers, contravening one of the top priorities of the design drivers. The handling qualities of the tilt-rotor are also a disadvantage when there is a failure, as the ability to maintain level flight in the case of a failure is of paramount importance. From a performance point of view, the tilt-rotor has the worst hover and forward flight performance as the blade is designed to operate in the middle ground of both regimes. The C_T/C_Q is also the lowest between the configurations, meaning that the configuration requires more power than the other configurations considered.

Multirotor Compound:

The multirotor compound offers a very good value proposition for the mission at hand. It is the middle ground between the performance of the tilt-rotor and the single main rotor compound with a C_T/C_Q of 7.8. The configuration provides with independent systems for hover and cruise operation. This decoupling of systems lets the configuration to be optimized for hover and forward flight independently. Unlike the single main rotor, the multirotor compound has the capability of reducing the impact that the lifting rotors have by aligning them with the planform. From a safety perspective, the multirotor compound has more redundancy in hover, and it has the handling qualities of an aircraft in the cruise regime, two qualities that neither of the other configurations has. In the case of an engine loss in hover, other motors can quickly recover and maintain level hover. If there is an issue during cruise that restrains power from the vehicle, this configuration can glide and do a rolling landing like any other conventional aircraft. In addition, this configuration provides the capability to make the attitude of flight are more predictable and manageable for the customers of the mission. Throughout the flight, the same pitch attitude can be maintained - a key for PRM and other disabled passengers, which neither of the other two configurations can guarantee. The main drawback of the design is that the structures needed to hold the lifting motors can be heavy and a source of drag in cruise.

5.4 Mission Energy and Power Requirements

To determine the optimum configuration for the mission, vehicle power and energy requirements must be analyzed. The methodology used to analyze and select the powerplant system(s) is detailed in Section 12 for readability when discussing the final configuration and is not duplicated here due to page limitations.

The energy consumed by each configuration for mission segments at the lowest mission time is shown in Table 5.3. For all three configurations, cruise is the longest segment and therefore consumes the most



energy.

The SMRC requires the lowest energy for the entire mission. The MRC requires 76% more, and the TR requires 130% more energy than the SMRC.

Mission Segment	Energy (kW-hr)	SMRC	TR	MRC
Hover 1		0.83	2.01	1.59
Axial Climb		2.59	5.71	4.79
Hover 2		1.33	3.21	2.54
Cruise Climb		4.13	5.00	3.98
Cruise		77.80	177.35	141.07
Cruise Descent		4.13	5.00	3.98
Hover 3		1.33	3.21	2.54
Axial Descent		1.12	2.39	2.01
Hover 4		0.83	2.01	1.59
Reserve		27.98	76.06	50.75

Table 5.3 Mission segments energy requirements for each vehicle

The power consumed by each configuration for mission segments for their minimum mission time is shown in Table 5.4. For all configurations, axial climb is the biggest power draw component of the mission, requiring more than double the cruise power. All configurations have a cruise lifting surface, penalizing the axial flight performance of the vehicles. The wings do not provide any lift during that mission segment but produce additional drag, which is exacerbated by the download of the rotors.

Mission Segment	Power (kW)	SMRC	TR	MRC
Hover 1		149.59	360.91	286.19
Axial Climb		249.62	589.74	467.66
Hover 2		239.20	577.10	457.61
Cruise Climb		171.50	208.00	165.38
Cruise		83.95	228.17	152.25
Cruise Descent		71.97	87.29	69.40
Hover 3		239.20	577.10	457.61
Axial Descent		264.85	608.21	482.34
Hover 4		149.60	360.91	286.19
Reserve		83.95	228.17	152.25

Table 5.4 Mission segments power requirements for each vehicle

While the energy requirements of the vehicles determine its battery mass, the power requirements of each vehicle were used to individually select an appropriate motor. A detailed methodology is presented in Section 12; it is not repeated here for brevity.

Battery masses of 305.09 kg (672.61 lb), 704.87 kg (1553.97 lb) and 537.10 (1184.10 lb) were required for the SMRC, TR and MRC, respectively.

The motors were selected from the power requirements and the number of rotors. The motors and controllers for the rotors of each configuration are listed in Table 5.5.

5.5 Wing Characteristics

All the finalist configurations are designed to take off vertically and transition to level forward flight. As the same methodology was used to perform the detailed vehicle design in Section 10, it is not repeated here and only results are shown. The NACA 2412 airfoil was selected to perform this preliminary wing design. The wings aerodynamic properties were obtained using AVL (see Section 4.4) providing a common basis to



	SMRC	TR	MRC
Rotor Motor	MagniX 650	MagniX 650	EMRAX 268
Rotor Controller	UniTEX Bamo Car D3	UniTEX Bamo Car D3	UniTEX Bamo Car D3
Propeller Motor	EMRAX 348	-	EMRAX 268
Propeller Controller	UniTEX Bamo Car D3	-	UniTEX Bamo Car D3

Table 5.5 Motor and controller selected for each vehicle configuration

perform a trade study between the configurations. The resulting wing planforms for each configuration are presented in Table 5.6.

	SMRC		TR		MRC	
	SI	English	SI	English	SI	English
Chord	1.22 m	4.0 ft	1.52 m	5.0 ft	1.37 m	4.5 ft
Span	9.75 m	32.0 ft	12.19 m	40.0 ft	12.34 m	40.5 ft
Taper Ratio	0		0		0	
Aspect Ratio	8.0		8.0		9.0	
Type	Rectangular		Rectangular		Rectangular	
$C_L/C_{D,i}$	58.9		59.1		63.98	

Table 5.6 Wing characteristics for each possible configuration

5.6 Landing Gear Analysis

The team's primary concern was the comfort of its passengers, so the cabin was designed before the configuration was selected, and the fuselage was built around it (see Section 8). Because of this, a single landing gear analysis could be performed for all three configurations.

The team compared two types of landing gear configurations: skids and wheels. The landing gears were modeled on the undercarriage of the fuselage (Figure 5.5), and the impact of the RFP required landing velocity of 2 m/s (6.6 ft/s) was analyzed for both landing gears using ANSYS AIM 19.1 [90]. The analysis is detailed in Section 11.5.

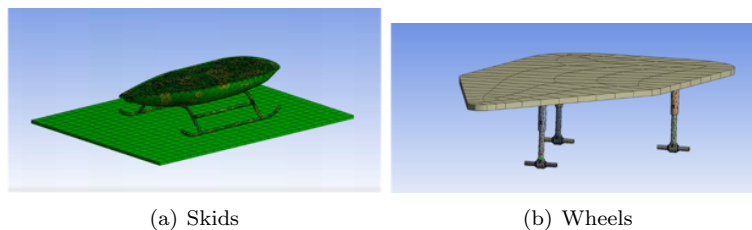


Figure 5.5 Landing gear models analyzed

The maximum acceleration felt in the cabin with the wheels landing gear was 63% lower than with the skids with fewer oscillations. The team decided to use wheels and suspensions to minimize load transfer to the passengers.

5.7 Final Configuration Selection

Based on the trade study performed in the previous sections, the multirotor compound was chosen as the final vehicle configuration. The multirotor compound configuration outperformed the single main rotor compound and the tilt-rotor configurations in many metrics. Of significant importance to the team



was the fact that the multirotor compound vehicle provides multiple levels of redundancy that the other configurations examined do not provide. Specifically in hover, the multirotor compound is still capable of maintaining flight in the case of a failure in one of the rotor systems. In addition to the safety afforded by the rotor systems in the hover condition, the multirotor compound also provides the comfort of an aircraft in cruise unlike the single main rotor configuration. This means the the multirotor compound is essentially a "flying platform" meaning that it can transition between cruise and hover with minimal changes in the aircraft attitude angle. This is paramount for the comfort of passengers especially those with sensitive injuries that may be exacerbated from being tilted at odd angles in cruise and transitions between hover and cruise. The decision between the SMR compound and the multirotor compound was solidified by a survey undertaken by the team on social media for non-engineers. With over 100 respondents, 94 % of them declared they would prefer to travel in an airplane than a helicopter. While the multirotor compound is a vertical take-off and landing vehicle, it is designed to resemble an airplane. A vehicle that is perceived like an airplane can be the first step into improving the public perception on rotorcraft and rotary wing vehicles. In addition, it will make significant inroads in addressing the challenges of mitigating the stress that PRM and other disabled passengers would have, creating a more inclusive and welcoming environment. In addition to the comfort of the passengers on board, the aircraft-like configuration of the multirotor compound in cruise allows for an extra layer of safety as it can glide to the ground in the instance of a catastrophic failure. In the case of the single main rotor and the tilt-rotor, a catastrophic failure would require an auto-rotation maneuver to reach safety. This maneuver involves sudden changes the vehicle attitude which causes discomfort to the passengers and will end in a rougher landing in comparison to the multirotor compound further endangering passengers.

6 Vehicle Design Overview

6.1 Vehicle Performance

Figure 6.1 (a) shows the stage wise battery consumption for *Balto* and Figure 6.1 (b) shows the time taken for each of the stages. 6.1 (a) shows that the the first stages of the mission which are hover and climb sequences only account 8.03% of the overall batter capacity. As expected the largest consumption of the battery capacity is the cruise phase of the mission which accounts for 50.4% of the battery capacity. At the end of the mission, 78.1% of the battery capacity has been expended. However, as dictated in the RFP, there must be 20% of additional reserve battery. In cases when this battery capacity is unused, *Balto* is able to reach full charge in a smaller amount of time which decreases the turn-around time for the passengers at the origin.

Tables 6.1, 6.3, and 6.2 detail the general vehicle, propeller and rotor performance characteristics, respectively.

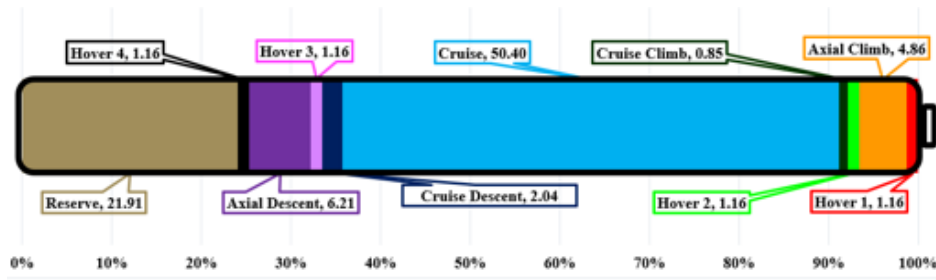
Parameter	Value	
	SI	English
Range	247 km	153 mi
Endurance	1.5 hr	1.5 hr
Maximum Operating Speed	82.31 m/s	160 kts
Cruise Velocity	54.02 m/s	105 kts
Best Range Velocity	54.02 m/s	105 kts
Best Endurance Velocity	46.3 m/s	90 kts
Vertical Climb Velocity	3.5 m/s	6.80
Cruise Power	100 kW	134.10 HP

Table 6.1 Vehicle performance

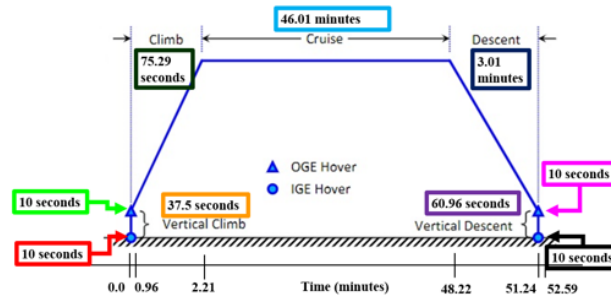
Parameter	Value	
	SI	English
Tip Speed (Hover)	158 m/s	520 ft/s
Disk Loading	622 N/m ² hr	13 lb/ft ²
Power Loading	0.0433 N/W	7.72 lb/HP
Blade Loading	0.0965	0.0965
Loss Factor	1.305	1.305
Figure of Merit	0.74	0.74
Hover Thrust	3056 N	687.02 lb
Hover Torque 430 N-m	317 lb-ft	
Hover Power 70.5 kW	94.5 HP	
Maximum Thrust Fixed Pitch 4072 N	915 lb	
Maximum Thrust Variable Pitch 4093 N	920 lb	
Maximum Torque Fixed Pitch 574 N-m	423.36 Lb-ft	
Maximum Torque Variable Pitch	660 N-m	486.79 lb-ft
Maximum Power Fixed Pitch	108.5 kW	145 HP
Maximum Power Variable Pitch	109.51 kW	146.31 HP

Table 6.2 Vehicle rotor performance





(a) Battery consumption by Stage



(b) Time taken per stage

Figure 6.1 Stage wise battery and time

Parameter	Value	
	SI	English
Tip Speed	183 m/s	600 ft/s
Thrust Coefficient	622 N/m ²	13 lb/ft ²
Torque Coefficient	0.0433 N/W	7.27 lb/HP
Advance Ratio (Cruise)	0.0965	0.0965
Efficiency (Cruise) 0.85	0.85	
Blade Angle (at 0.75R in Cruise)	24.12 deg	24.12 deg
Torque (Cruise)	327.36 N-m	241 lb-ft
Power (Cruise)	49 kW	65.71 HP

Table 6.3 Vehicle Propeller Performance

6.2 Vehicle Systems Overview

Balto's lifting rotors were initially designed to be fixed pitch, variable RPM rotors. While this would lower the complexity of the rotor systems, the large diameters created barriers to full RPM control especially in the cases when instant responses to correct for failures are required. Figure 6.2 illustrates the instantaneous torque response to one motor loss for a RPM control and a variable pitch and RPM rotor. For the variable RPM rotor to obtain the same instantaneous response as the variable pitch and RPM rotor, the required continuous torque of the motors would exceed the maximum available continuous torque. Therefore, it was necessary to utilize a combination of variable pitch rotors and fixed pitched rotors for *Balto's* lifting rotors. This combination is illustrated in the Figure 6.3. The variable pitch lifting rotors on the outboard allow of quick control responses to large changes in moments in the case of an engine failure and will prevent large changes in attitude in these cases while allowing inboard

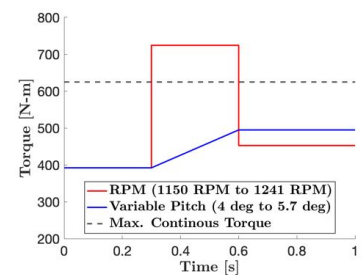


Figure 6.2 Torque response to one motor loss



fixed pitch lifting rotors to compensate for the failure case. This strategy allows for the retention of *Balto's* stability while also mitigating the large increase in the power required due to the large changes in the torque required.

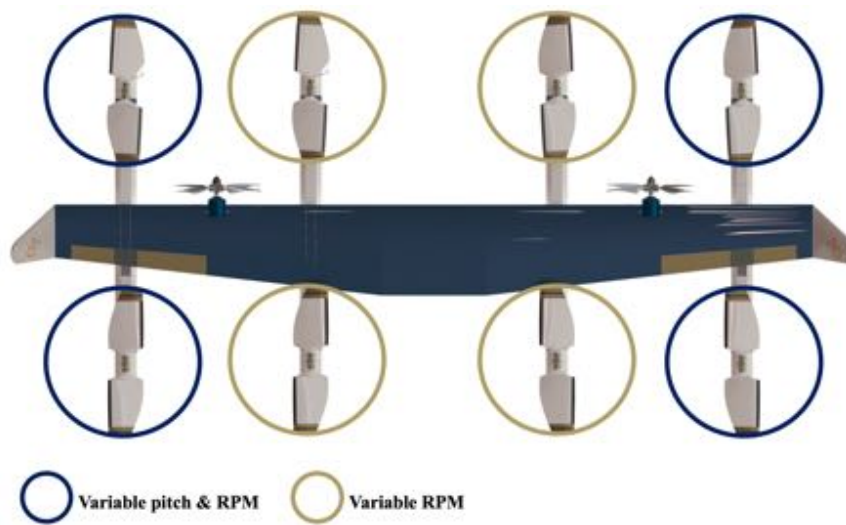


Figure 6.3 Location of variable/fixed pitch rotors on *Balto*

7 Cabin Design

7.1 Initial Cabin Sizing

The RFP calls for two configurations of the cabin:

- One baseline configuration that accommodates four (4) passengers with full mobility
- One configuration that accommodates at least two (2) passengers with disabilities

Both configurations must additionally accommodate one pilot and luggage for all passengers. All passengers are allowed a checked bag, a carry-on bag, and a personal item. Furthermore, the vehicle shall provide storage for any additional medical equipment passengers might travel with.

The team concluded that the most space-limiting configuration would be the cabin arrangement accommodating two passengers with disabilities, as mobility aids can take up a significant room. Therefore, the cabin was sized to this configuration.

7.1.1 Wheelchair Market Study

A wheelchair is the largest mobility aid that the cabin will accommodate. As such, the team performed a market analysis of wheelchairs available today to determine the maximum size allowed in the cabin. A selection of wheelchairs is presented in Table 7.1, and shows that the maximum length and width of a wheelchair are 1.02 m (3.3 ft) and 0.74 m (2.4 ft), respectively. Moreover, the heaviest wheelchair on the market is 159 kg (350 lbs). These dimensions were therefore used to size the cabin.



Wheelchair	Type	Width		Length		Weight	
		m	ft	m	ft	kg	lb
Jazzy 600 ES [92]	Powered	0.635	2.08	0.914	3.00	56.2	124
Merits Health P301 Gemini Power Wheelchair [93]	Powered	0.614	2.00	1.016	3.33	158.8	350
Jazzy 1450 Heavy Duty [94]	Powered	0.737	2.42	0.965	3.17	152.4	336
The Quickie LIFE R Active Wheelchair [95]	Rigid Frame	0.686	2.25	1.016	3.33	10.9	24
Ki Mobility Tsunami ALX [96]	Rigid frame	0.559	1.83	0.508	1.67	9.1	20

Table 7.1 Examples of wheelchair types, sizes, and weights; maximum values are highlighted

7.1.2 Sizing Considerations

Mr. Bob Shaffer, a travel agent, specializing in travel for people with disabilities, confirmed previous research: most people with reduced mobility travel with a companion or caregiver [15,97]. While the RFP only required a configuration that could accommodate two passengers with reduced mobility, it was important that each person with reduced mobility could travel with a companion if they so desired. The team decided to design the cabin that could accommodate two passengers with reduced mobility and two passengers with full mobility as their caregivers. However, these two additional passengers will only be allowed to carry one personal item and one carry-on bag each to minimize weight.

For the cabin to offer two configurations accommodating either two passengers with reduced mobility and their two caregivers, or four passengers with full mobility, the team decided the best option was to have seats that could either be stowed or removed. The team wished the cabin to be fully contained, meaning that ideally, no items required for alternative configurations would be left at the departure locations. For this purpose, stow-away seats were deemed preferable. This comes with one main disadvantage: when these seats are stowed, they are an additional weight on the vehicle for no other use. However, the team believed that the benefit of having a self-contained vehicle was reasonable compensation. Therefore, all sizing decisions were made with two fixed seats and two seats that could be stowed or folded to leave space for wheelchairs.

7.2 Cabin Configuration Selection

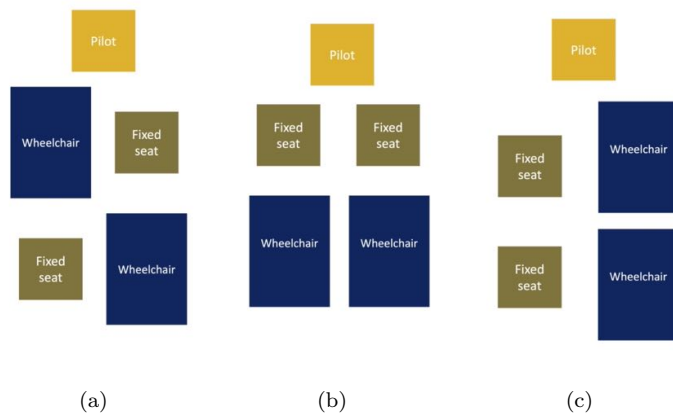


Figure 7.1 Cabin configurations considered

As stated previously, the team decided that both cabin configurations would include two fixed seats and two folding seats to permit wheelchairs to be installed and secured to the cabin floor. The cabin configuration was sized for the wheelchairs to accommodate the powered wheelchairs as they tend to be larger than the folding seats.

The team considered four arrangements of the wheelchairs in the cabin, shown in Figure 7.1. The first option was to have the fixed seats and wheelchairs in a diagonal arrangement, as shown in Figure 7.1 (a). While this configuration allowed for a smaller cabin width, it would require complicated ingress and egress, especially for the wheelchairs. Different access ramps would be required for each

wheelchair, adding weight and complexity to the vehicle. The team decided both wheelchairs should be able to access the vehicle using the same ramp, and examined the possibility of having the fixed seats in the front, and both wheelchairs in the back, with an access ramp at the back of the vehicle, as shown in Figure 7.1 (b). While this option solved the problem of ramp access, it required the cabin to be wider than for the



previous arrangement. Lastly, the team considered arranging the wheelchairs in a row, side-to-side with the fixed seats, as shown in Figure 7.1 (c). This would permit easy ingress and egress, give caregivers easy access to the passengers on the wheelchairs and would not require a cabin as wide as for design (b). The major concern in this seat arrangement was the possibility of a weight imbalance for the configuration without wheelchairs, but a simple center of gravity (CG) analysis varying the number of passengers and wheelchairs determined that the CG did not move significantly (see Section 13), so that the impact on vehicle weight and balance, as well as flight control design was minimal. This seat arrangement was considered the most beneficial and chosen for the cabin design.

Using this configuration, an initial cabin was sketched. A market analysis of the cabin volume was performed with the minimum cabin width defined with two wheelchairs and a 0.38 m (1.25 ft) aisle width to determine if the designed cabin volume was in the same range as current helicopters. A preliminary cabin weight was obtained accounting for four passengers and a pilot, luggage, four seats, and a ramp. Estimates of the cabin material, insulation and covering, as well as flight control weights, were obtained from historical data [98,99]. This initial gross weight estimate was used to perform the conceptual vehicle sizing (see Section 5).

Once the preliminary layout of the cabin was selected, the team used an augmented reality software, Augment3d [100], to test a life-size layout of the cabin and determine what changes would increase the comfort of *Balto's* passengers. An example of this recreation is shown in Figure 7.2. This experiment helped the team finalize the location of the seats, as these were initially too close to the wall and to the curved ceiling. The team also confirmed that the location of the side door and the luggage cabinets did not diminish the experience of the passengers in the front row. This technique was used again to validate the final cabin configuration, detailed in Section 7.4.



Figure 7.2 Virtual Reality recreation of the preliminary cabin layout

7.3 Seat Selection

7.3.1 Selection of the fixed seats

The two fixed seats, present in both configurations, were designed to be executive seats, to offer as much comfort as possible with weight and space considerations in mind. Indeed, it was important to include seats that are comfortable for people with physical disabilities (e.g. chronic pain), but also people with hidden disabilities (e.g. autism spectrum disorder). These seats were also required to be crash-worthy, while minimizing their weight. The team consulted with International Aircraft Services (IAS), who specialize in the maintenance of VIP and service helicopters, to find an optimal seat [101]. The VIP seat used in luxury Airbus AS 365 helicopters was selected, weighing 30 kg (66 lbs), only 3kg (6 lbs) more than the estimated value chosen in the preliminary sizing.

7.3.2 Selection of the folding seats

After the fixed seats were selected, the next step was to find which seats could be used for the stow-away seats. Multiple options were considered. First, the team explored the option of using jump seats, as used on aircraft for crew members or in buses to offer additional seating. These seats can be attached to the wall next to the proposed wheelchair locations, occupying minimal space when stowed, and can be deployed when there are passengers that require these seats. This posed a major problem: the four non-PRM configuration would have two comfortable seats and two much less comfortable seats. If this vehicle is to be used as a taxi, all proposed seats should offer a similar, and adequate, level of comfort. The jump seats were therefore discarded.

The team then considered the option of using folding seats, as is used in cars, from Sports Utility Vehicles (SUVs) to minivans. These seats would offer an acceptable level of comfort, and when stowed would leave space on top of them to place wheelchairs. Most folding seats, however, present a “bump” when folded into the compartments. This would be detrimental for the alternative configuration with wheelchairs, as it would



require additional ramps or covers that account for this bump. One type of folding seats did not have this problem is the Stow 'n Go™ system developed and patented by Chrysler Group [102]. This fold-in-the-floor system allows seats to be completely stowed within the cabin floor [103]. The folding mechanism is illustrated in Figure 7.3. When folded, the cabin floor has a completely flat surface, which would allow wheelchairs to access the cabin and be tied down on the floor.



Figure 7.3 Stow 'n Go™ folding mechanism (from Ref. 102)

7.3.3 Design of wheelchair tie-downs

This vehicle, unlike current air transport, allows passengers that require wheelchairs to remain in their wheelchairs during the flight. This permits a more comfortable flight for the passengers and accommodates the transport of wheelchairs that cannot be folded. It also eliminates the need to transfer passengers from their wheelchair to the seats in the cabin, as this can exacerbate injuries [15]. These wheelchairs need to be secured during the flight, just as they are in ground transportation. A study by van Roosmalen et al. found that individuals using wheeled mobility devices found the restraints in public transit uncomfortable and time-consuming and vastly preferred the restraints used in private vehicles [105]. As such, the team decided to model *Balto's* restraining system based on restraints used in private and family vehicles.

To secure a wheelchair, four tie-downs are required: two in the front and two in the back. Additionally, the passengers need a three-point seat belt while on their wheelchair. The resulting wheelchair tie-down and occupant restraint system (WTORS), shown in Figure 7.4, is composed of four main components: (1) floor attachment, (2) tie-down, (3) wheelchair attachment, and (4) occupant belt [104]. This system satisfies requirement 14 CFR 29 §29.785.

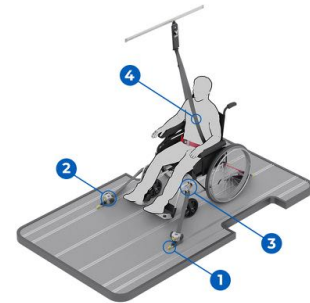


Figure 7.4 Components of the WTORS (from Ref. 104)

Floor attachment:

There are three different kinds of floor attachments: solo floor anchors, rails, or permanent bolts to the cabin floor. Solo floor anchors and permanent bolts to the floor are fixed and restrict the versatility of the wheelchairs that can be secured on board. Therefore, this vehicle uses rails. These are more invasive than the other two options, but offer increased flexibility. This is the best option to accommodate different wheelchair sizes, and to permit easy and effective reconfiguration.

For WTORS in personal vans, rails are offered as low profile or surface rails. For this vehicle, low profile rails are preferred, to minimize disturbance to the cabin floor as much as possible. These rails are flush with the floor, and have a height above the floor of only 0.004 m (0.013 ft) [106]. End caps are used to provide a smooth finish to the rails.

Tie-down:

The tie-down connects the wheelchair attachment to the floor, providing tension to restrain the wheelchair. There are a multitude of types of tie-downs [104]. The simplest one is the over-centre buckle, but the team decided this was not adapted to air travel; they are time-consuming and require the operator to move freely around the wheelchair, which is not possible in an enclosed cabin. The team decided to use a Quattro Express by BraunAbility. This tie-down is a spool of self-tensioning webbing inside a plastic casing. This



provides ease of use in confined spaces, and maximum security.

Wheelchair attachment:

Wheelchair attachments secure the wheelchair to the tie-down. They can be hooks, carabiners, or buckles. Since this attachment needs to secure the wheelchair in air travel while being easy to release, the team decided hooks and carabiners were not ideal. and decided to use a tongue and buckle wheelchair attachment, shown in Figure 7.5.



Occupant belt:

Figure 7.5 Buckle and tongue attachment (from Ref. 104)

The belt has two main components: the floor connection and the belt [104]. The belt floor connection is on a stalk, which is a metal wire encased in rubber. This raises the buckle off the floor, as opposed to standard buckles, allowing for an easier reach and buckling of the seat belt. The stalk is placed on a secondary rail placed inward of the tie-down rail, as this increases the effectiveness of the seat belt in case of a crash [107]. To conform to requirements 14 CFR §29.785, the belt is a static 3-point belt, including a lap and shoulder belt with a single point release, located on the stalk. The belt is locked on the wall using an upper anchorage point. For best crash protection, the upper anchorage point has to be located such that a shoulder belt angle of 55° with the wall is obtained, and it must be placed 0.9 m (3 ft) behind the occupant's shoulder [107]. As the optimal location of the upper anchorage point will change depending on the passenger, a rail similar to the floor surface rail described previously is used to increase flexibility [106, 108].

7.4 Final Cabin Configuration

The final cabin design is shown in Figure 7.6. It has two configurations: one with four regular seats, and a second with two fixed fixed and two locations for wheelchairs. The cockpit is separated from the main cabin by a thin wall, both to increase the pilot safety, as per the design objectives (see Section 3.1.1), and to shield passengers from the rotor flickers that shine through the windshield, preventing rotor flicker vertigo, which is explained in Section 2.3.

7.4.1 Cockpit layout

The cockpit, illustrated in Figure 7.7, is configured for a single pilot and conforms to 14 CFR §29.771 through §29.779 to provide a simple and intuitive piloting experience. All controls are obtained from a joystick, as proposed by Lombaerts et al. [109], which is located to the side of the pilot. This is modeled after the Unified Control Architecture used by Joby Aviation, who obtained a Part 135 Air Carrier Certification in May 2022 [110, 111]. In addition to simplifying the work done by the pilot, forgoing the use of pedals allow for a larger range of pilot heights specified in 14 CFR §29.777.

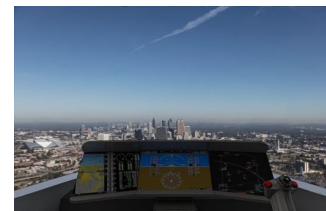


Figure 7.7 Cockpit view

Three screens in front of the pilot display all important flight information that is common in traditional aircraft to make training easier and more intuitive. Large windshields offer an ample view of the vehicle's exterior, permitting a safer flight.

A small compartment allows the pilot to keep a personal item stored in the cockpit during flight.

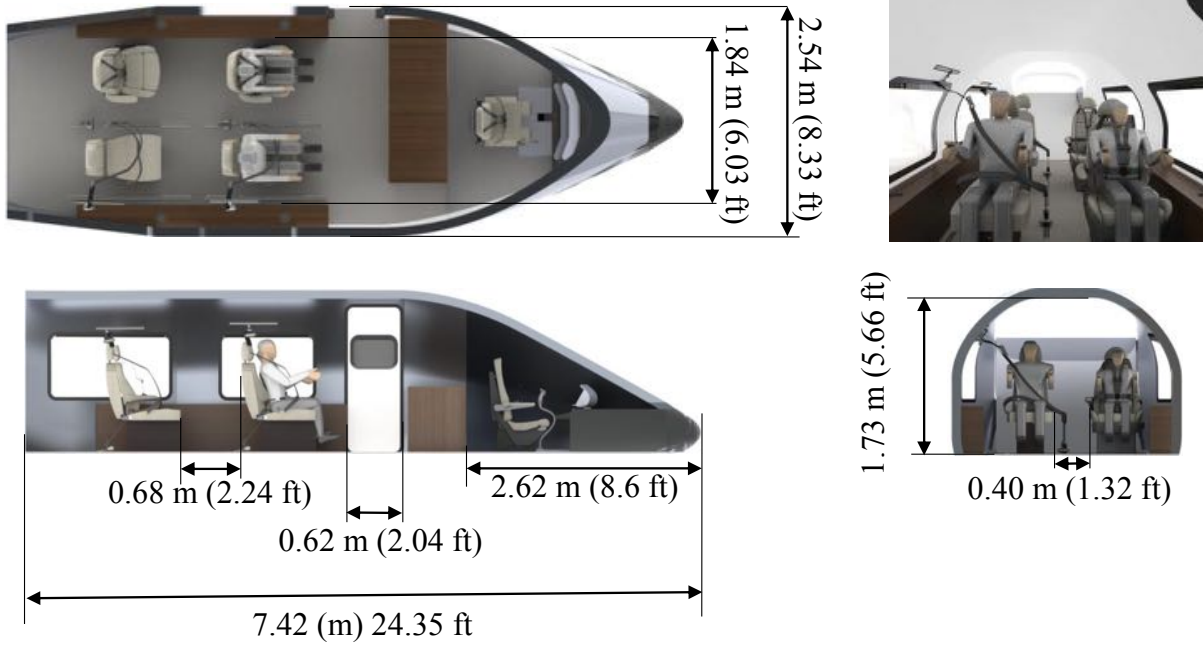
7.4.2 Main cabin layout

The executive seats are located on the left side of the cabin. Placed 0.76 m (2.5 ft) apart, they offer ample legroom to maximize passenger comfort. Their simple leather patterns have few seams and little texture and color changes to accommodate passengers with touch and light sensitivity (e.g., passengers with



Cabin Three View

Full Mobility Configuration Three View



Reduced Mobility Configuration Three View

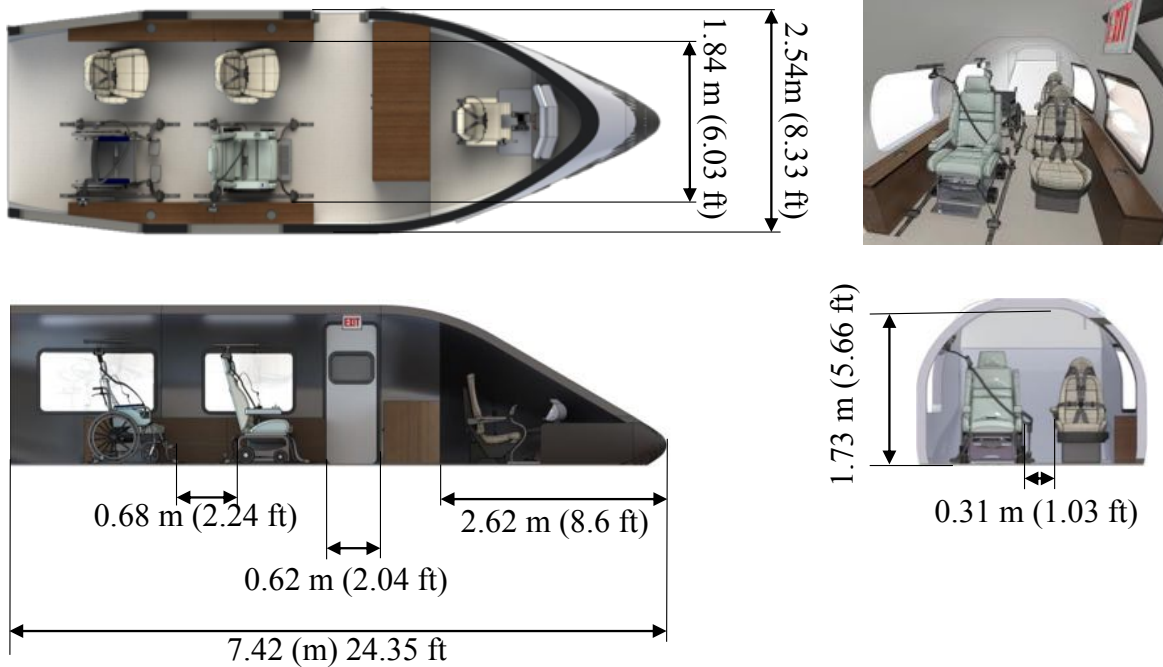


Figure 7.6



autism spectrum disorder). Their energy-absorption technology offers increased protection for passengers with physical disabilities. They are equipped with four-point harness with single-point release, satisfying requirement 14 CFR 29 §29.785. If a child is travelling on the *Balto*, the harness on these seats can be switched to a CARES child aviation restraint, a belt and buckle device recently certified for aviation use by the FAA [112].

The right side of the cabin can be reconfigured to accommodate either two wheelchairs or two regular seats. In the first configuration with two executive seats and two wheelchairs, the Stow 'n Go seats are stowed in their compartments, and the wheelchairs are positioned on top of them. Tie-downs are secured on the rails on both sides of the wheelchairs, and the inner rail is equipped with the seat belt stalk. In the configuration with two executive seats and two regular seats, the Stow 'n Go seats are deployed. For both configurations, the upper anchorage point is fixed at the optimum location for the current passenger, as defined in Section 7.3.3. The legroom in the right-side seats for both configurations is at least 0.6 m (2ft), and can increase in the two-wheelchair configuration depending on the wheelchair's length. The main aisle width is at least 0.38 m (1.25 ft), which satisfies requirement 14 CFR 29 §29.815. The Stow 'n Go seats are also equipped with anchors to secure small children booster seats approved for aviation use.

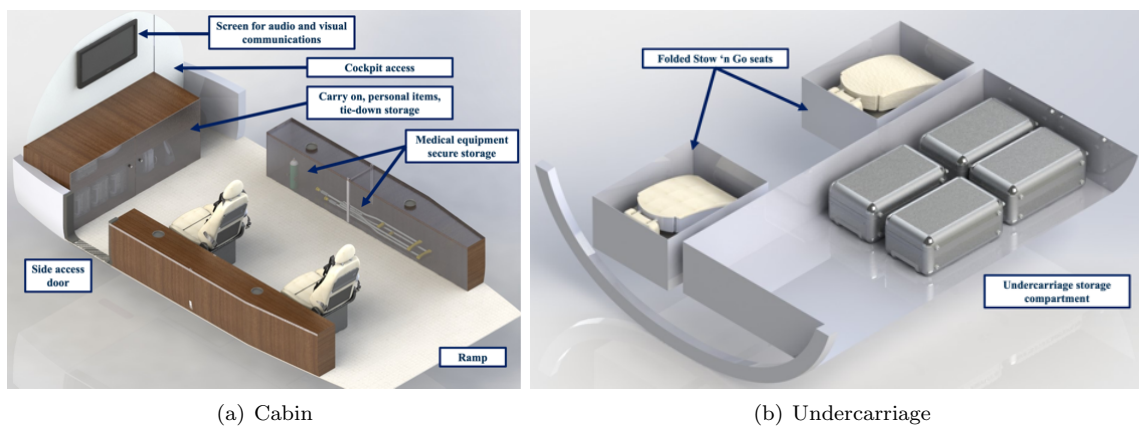


Figure 7.8 Cabin and undercarriage storage locations (wheelchair rails and folding seat compartments hidden for clarity)

The passengers' carry-on luggage and personal items are stored in the two baggage storage compartments at the front of the cabin, as shown in Figure 7.8 (a). When not in use, wheelchair tie-downs components, as well as complimentary noise-cancelling headphones, are also stored in these compartments. These are located at least 0.6 m (2 ft) from all the seats, allowing passengers to retrieve their bags in flight without inconveniencing other passengers. The compartments are closed with a sliding door, which is locked and secured during take-off and landing, satisfying requirement 14 CFR §29.787.

Checked bags and other oversized luggage (e.g. folded wheelchairs and strollers) are placed in an undercarriage baggage compartment, shown in Figure 7.8 (b) and accessed from the outside through the opening near the side door (Figure 7.9). The bags are loaded one at a time, and secured with straps to prevent them from shifting during flight. The cargo compartment conforms with 14 CFR §29.787.

A television screen placed on the wall at the front of the cabin allows the transcription of all audio cues into visual format, to conform with the accessibility requirements of *Balto*'s passengers. Wall-length storage compartments on both sides of the cabin, conforming with the external curvature, enable passengers to store any additional equipment they might travel with. These compartments, shown in Figure 7.8, are 0.53 m (1.74 ft) tall, 2.78 m (9.17 ft) long, and approximately 0.25 m (0.82 ft) wide (depending on the curvature). They can accommodate canes, crutches, and small health monitoring systems. A strap located on the interior of



Figure 7.9 Undercarriage storage compartment access door



these compartments allow passengers to secure oxygen tanks or other medical equipment that needs to be secured in flight. Access to these storage compartments is from the top and is designed so that a passenger in either the front or back row can open the storage without disturbing the other passenger. Built into the top of the side storage compartments are cupholders and an external lip so that they may also function similar to commercial aircraft tray tables, but with improved access for passengers with wheelchairs.

To increase on-board comfort, an AC unit is installed in the cabin. This also adds ventilation to the cabin, and satisfies requirement 14 CFR 29 §29.831.

A list containing the items that are included in each configuration is presented in Table 7.2.

	PRM configuration			Full mobility		
	Qty (max)	Mass, kg	Mass, lb	Qty (max)	Mass, kg	Mass, lb
Pilot	1	91	200	1	91	200
Pilot seat	1	16	35	1	16	35
Cockpit instruments	1	10	22	1	10	22
Screen	1	6	13	1	6	13
Passenger	4	408	900	4	408	900
Wheelchair	2	179	395	0	-	-
Carry on luggage	4	40	88	4	40	88
Personal item	4	20	44	4	20	44
Checked baggage	2	45	100	4	91	200
Fixed seat	2	59.9	132	2	59.9	132
Folding seat	2	40.8	90	2	40.8	90
Front baggage compartment	2	15	33	2	15	33
Side compartments	2	15	33	2	15	33
AC and ventilation system	1	3.6	8	1	3.6	8
PA system	1	1.8	4	1	1.8	4
Seat rails, tie-downs, seat belts	-	8.4	18	-	8.4	18
Total	-	959.5	2,115	-	826.5	1,822

Table 7.2 Items and passengers and their weights in each cabin configuration. The differences between configurations are highlighted in bold.

7.4.3 Cabin Entry Points

The passenger cabin has two entry points. A hinged ramp at the rear of the cabin is used as the primary access point. ACAA regulations require boarding ramps to have a slope equal or less than 1:4 [rise]:[run] for assisted boarding [113], which is the case of *Balto*'s ramp slope. The transition from the ramp to the cabin floor presents a change in level of 0.0038 m (0.0125 ft). This step is lower than the maximum allowed 0.0063 m (0.0208 ft) non-treated step from ADA regulations [114]. *Balto* is equipped with a passive hydraulic system to open and close the access ramp.

The second access point is the side door located ahead of the front fixed seat. This door requires a step stool to ingress and egress, as it is located 0.25 m (0.075 ft) above the ground. This step stool is stored in the underside compartment during flight.

The cabin has windows on both sides. These windows can be covered with shades to shield to flicker of the light through the rotor blades and prevent light overstimulation.

The side door, ramp, and windows conform to 14 CFR §29.783, §29.803, §29.805, §29.807 (4), §29.809, and §29.813.



7.4.4 Cabin Acoustics

Noise is already a major consideration when designing aircraft, especially those with rotary wings. *Balto* has the added constraint of being designed with comfort for all passengers in mind, including those that might have increased noise sensitivity (e.g., people with chronic migraines or people with autism spectrum disorder). As such, one of the cabin design objectives was to keep the noise level in the cabin below 70 dB.

The team investigated different options to reduce the noise in the cabin. Initially, an active noise-cancelling system was preferred. The team believed it would be lighter and more efficient than traditional acoustic foam. However, active noise control systems are usually programmed for either high or low frequency noises [115, 116], while rotorcraft produce both [117]. As such, an active noise-cancelling system would be complex and not as efficient as initially thought [117, 118]. The team therefore decided to return to the acoustic foam method. While these acoustic treatments come with a weight penalty, they offer high and low frequency noise reduction and are used in commercial aviation today.

For additional noise reduction, noise-cancelling headphones are offered to passengers who request them.

7.5 Operations, Ingress & Egress

Passengers:

Prior to passenger arrival to the launch site, they will be asked about special requests. Prior to every flight, *Balto*'s ground operations team will decide what type of configuration will be set for the vehicle. The online booking system caps passengers with reduced mobility to two per flight (as per the RFP requirement) to avoid over-booking.

Passengers with anxiety or fear of new spaces (e.g. autism spectrum disorder) can access an external website and obtain information about the flight, including a video detailing all details of a flight aboard the *Balto* and experience a virtual flight to reduce unexpected events and anxiety during flight.

The PRM configuration, described in section 7.4.2, is employed when at least one wheelchair will be used during the flight, or when two passengers or less are traveling. The full mobility configuration is used when no wheelchair is needed during the flight.

In the PRM configuration, passengers with wheelchairs board through the back ramp with the assistance of ground crew or their caregiver, as illustrated in Figure 7.10. The wheelchairs are secured using the WTORS described in section 7.3.3. The upper anchorage point and seat belt floor connection are set using the passenger's size ensuring maximum security and comfort. Once the wheelchairs are secured, the passengers are strapped in using the integrated three point seat belt.



Figure 7.10 *Balto*'s open ramp for boarding

In both configurations, passengers without a wheelchair may ingress through the ramp using the handrail or through the side door. Unless requested, full mobility passengers must fasten their seat belts on their own and adjust their seating for their comfort. Prior to take-off, the pilot will ensure that all seat belts and anchorage points are properly secured and ready for flight.

Passengers travelling with small children are required to bring child car seats that are approved for aviation use. These seats are secured using the anchors from the Stow 'n Go seats, as well as the seat belts.

Baggage and Personal Items:

Personal items and carry-on bags are secured in the front baggage compartments, and the doors to these compartments are secured for departure. For PRM passengers the personal items are stored by the pilot or their caregiver. The storage compartments were designed for easy access to passengers of all heights and mobility. Any additional personal items that cannot be stored in the front compartments, either due to size



(e.g. crutches) or function (e.g. oxygen tanks), may be stored and secured in the side compartments.

Checked bags and oversized items, like folded wheelchairs, strollers and prams are stored in the underside baggage compartment.

If passengers are traveling with service animals, they must stay near the passenger thorough the flight, and stay at their feet during take-off and landing.

Pilot:

Prior to every flight, the pilot is taken through a briefing on each of the special requirements of the passengers. Following the briefing, an exterior pre-flight inspection is done to ensure that the *Balto* is safe for the flight.

The pilot enters through the side door, and accesses the cockpit through the door located next to the baggage compartments. Once seated, he performs the interior pre-flight checklist.

Once all passengers are seated and the doors are closed and secured, a safety information video is played on the screen at the front of the cabin. Prior to departure the pilot enters the cabin to perform a safety check on the passengers.

In-flight:

Passengers are recommended to remain in their seats with their seat belt fastened, but they are allowed leave their seats to access the baggage compartments and retrieve personal items from their bags. Any pilot communications are transmitted through the PA system and transcribed into text displayed on the screen using a speech-to-text software.

Emergency Operations:

In case of emergency, the side door and ramp can be used as emergency exits, as per requirements 14 CFR §29.803 through §29.815. All the cabin windows, as well as the cockpit windshield, are push-out windows, can be used as emergency exits, and conform to requirements 14 CFR §29.805 and §29.807 (4). They exceed minimum dimensions specified in 14 CFR §29.807 (4) and are marked appropriately following requirement 14 CFR §29.811. The aisle width of 0.4 m (1.2 ft) enables unobstructed evacuations using any of the emergency exits, as per regulations 14 CFR §29.813 (b) and (c).

7.5.1 Requirement Compliance

Requirements from the 14 CFR 29 and those obtained from the cabin design objectives (see section 3.1.1) and the overview of specific needs to accommodate people with disabilities (see section 2.3) are presented in Table 7.3, along with the design solutions to meet them.



Requirement	Solution
§29.771-§29.775	The pilot compartment has a large windshield offering unobstructed view in both non-precipitation and precipitation conditions. The windows and windshield are made of stretched acrylic, which will not break into dangerous fragments.
§29.777, §29.779	The vehicle has a unified control system that consists of a joystick and a collective stick. The joystick movement is tied to the body rotation of the vehicle, and the collective follow the same intuitive controls are traditional helicopters.
§29.783	The ramp is located away from the rotating blades. The side door can only be opened when propellers and rotors are off to avoid injuries. Door handles are flush with the surface when closed, and visible when open to ensure easy direct visual inspection of the locking mechanism by crew members.
§29.785	The fixed seats are equipped with single release point safety harnesses utilized in traditional helicopters. The folding seats and wheelchairs use a WTORS that can be adjusted to ensure maximum security for the passengers, including a safety belt and shoulder harness with a single-point release.
§29.787	All baggage are secured using straps and are locked during take-off and landing. In emergency landing situations, the underside baggage compartment will not interfere with the safe evacuation of the vehicle.
§29.803-§29.813	The ramp, the door, the windows and the windshield can all be used as emergency exits for our Type IV vehicle. They are properly labeled as such with exit signs that meet or exceed the required font size. The threshold from the ground is less than 0.8 m (2.5 ft). The seat placement allows for easy and unobstructed evacuation of the vehicle.
§29.815	The cabin aisle width is no less than 0.38 m (1.25 ft), which equals the required width for a passenger capacity of 10 or less. The aisle is spacious to allow reduced mobility passengers to access their seats easily.
§29.831	The AC system is used as a ventilation system.
Comfort	Fixed seats are designed after the Airbus aircraft seats used in VIP configurations to increase comfort for passengers with reduced mobility (e.g. chronic pain). The seats do not have an aisle armrest to ensure easy transfer to the seat.
Light and rotor flicker shield	Windows are equipped with shades to cover the light coming from the outside of the vehicle to accommodate photosensitive passengers.
Caregivers	Both cabin configurations allow passengers to travel with a caregiver if they so desire.
Communication accessibility	All information is presented in audio and visual forms through signs, a vehicle PA system, and a screen located at the front of the cabin.
Noise	The noise while seated does not exceed 70dB with the <i>QuietBubble</i> system. Noise-cancelling headphones are provided to passengers that request them.
Textures, colors	Seats are made of leather with minimal seams. The cabin has a neutral color scheme to prevent over-stimulation.

Table 7.3 Cabin requirement compliance

t



8 Fuselage Aerodynamic Design

Once the initial cabin configuration was selected (see Section 7.2), a preliminary fuselage was designed around it. *Balto's* primary concern is the comfort of its passengers, so designing the cabin first and then constraining the fuselage to it ensured that the passengers (and particularly PRM) would have a safe and comfortable flight. Once the initial fuselage was designed, it was optimized for structural and aerodynamic performance.

Four iterative stages of the fuselage are shown in Figures 8.1 and 8.2.

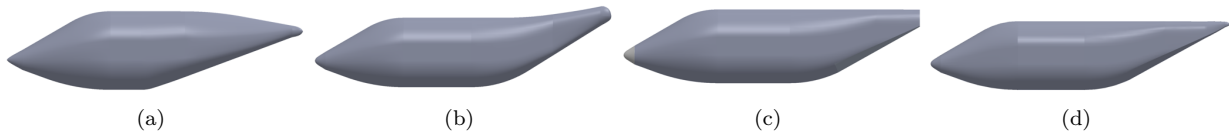


Figure 8.1 Fuselage iterative stages, side views

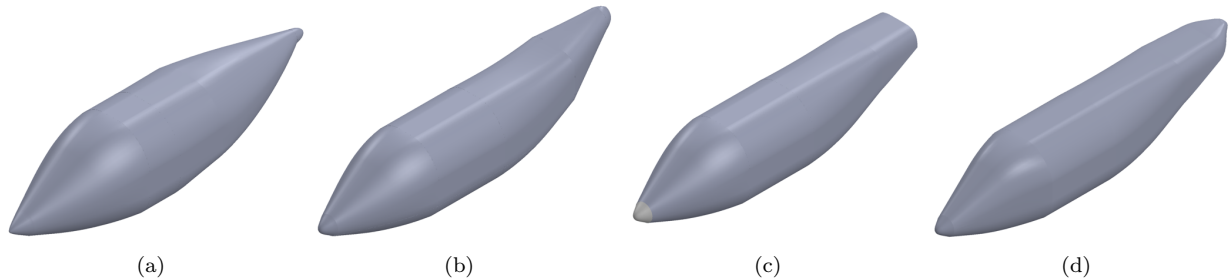


Figure 8.2 Fuselage iterative stages, isometric views

The first iteration of the fuselage, Figures 8.1 (a) and 8.2 (a), was designed around the initial cabin, optimizing the aerodynamic performance of the fuselage by shaping the nose and tail as points. While the tail had an aerodynamic shape, it also had a slope of 27 degrees from the fuselage to the tail tip. Greater ramp angle changes of more than 20 degrees are known to induce increased flow separation and therefore drag [119]. However, the team understood from the beginning that the ramp had to have a 1:4 [rise]:[run] slope, restraining the angle to obtain that ramp length. To mitigate flow separation while satisfying the RFP requirements, the fuselage was designed so that the angle change was progressive: an initial 15 degree angle was used, then an additional 12 degrees change was used to obtain the required 27 degree slope to meet the RFP and ramp constraints (i.e., meeting FAA and ADA requirements).

As the vehicle design evolved, the cabin was lengthened to include sufficient storage for bags and additional legroom for service animals and caregiver access. Moreover, the first *Balto* configuration had two wings, both with lifting rotors, requiring the tail to be raised so the rotor and wing wakes would not interact, yielding the fuselage shown in Figures 8.1 (b) and 8.2 (b). The empennage rise angle was sharpened, but computational analysis performed using FlightStream [88] indicated that there was no significant flow separation. However, this fuselage presented considerable structural constraints, as the keel beam had to be raised near the end. It was also determined that the empennage width should be kept almost constant for a secure access ramp into the cabin.

Morphing into a single-wing configuration, *Balto's* fuselage evolved again, as shown in Figures 8.1 (c) and 8.2 (c). The empennage was lowered to be level with the rest of the fuselage, enabling greater structural integrity of the airframe. The tail width was also kept almost constant throughout. This fuselage configuration had many benefits: the nose was aerodynamically shaped, the cabin length was optimal, and the empennage dimensions permitted a ramp that met FAA and ADA requirements.

This configuration presented a considerable disadvantage: the empennage had a blunt edge, creating flow



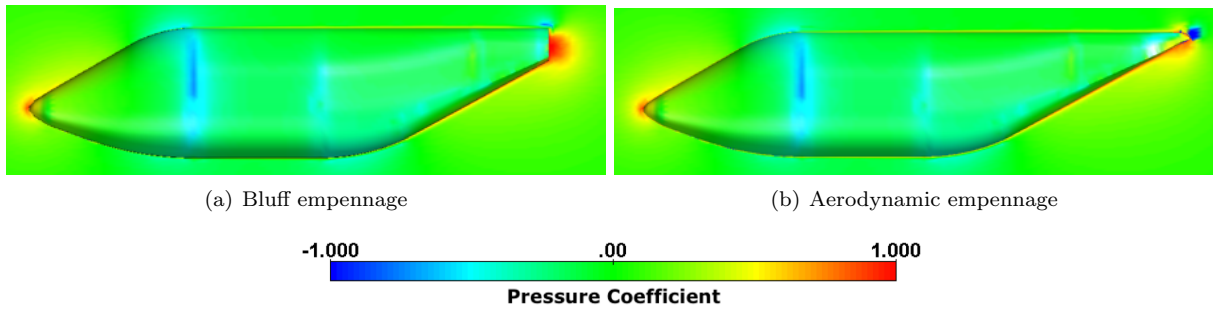


Figure 8.3 Pressure coefficient contours of the fuselage without and with fairing

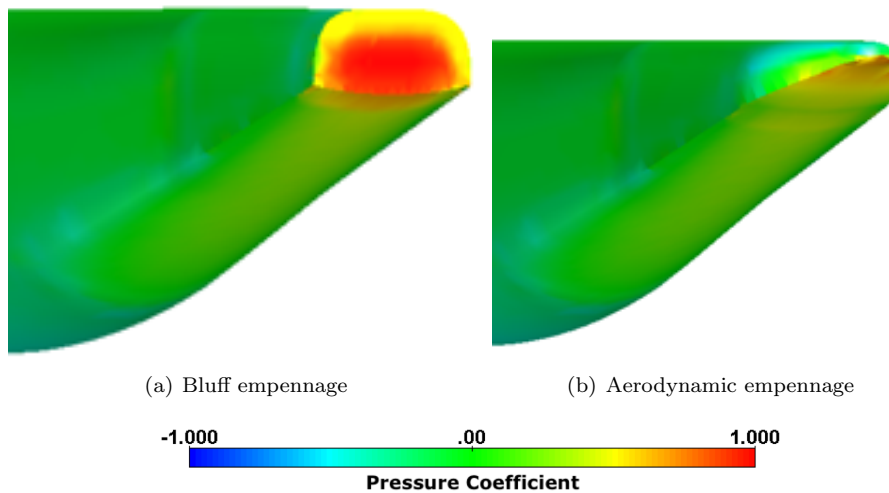


Figure 8.4 Pressure coefficient at the empennage without and with fairing

separation and drastically increasing the drag of the vehicle. To overcome this challenge, the team designed an aerodynamic fairing for the empennage tip, as shown in Figures 8.1 (d) and 8.2 (d). The aerodynamic effects of this fairing were analyzed with FlightStream and used to obtain a drag estimate of *Balto*'s fuselage with and without the added aerodynamic fairing. Resulting pressure coefficients at the cruise speed of 54 m/s (105 knots) are shown in Figures 8.3 and 8.4.

The contour plots show the effects of the aerodynamic fairing on the fuselage aerodynamic properties. The separation region (dark blue) at the latter part of the fuselage is much less pronounced in 8.5 (b) when the fairing is introduced, and the drag coefficient is reduced by 12% from 0.1190 to 0.1042. *Balto*'s final design used the fuselage presented in Figures 8.1 (d) and 8.2 (d).

Figure 8.5 shows that the 27 degrees angle change, with the 15 degree then 12 degree progression, delays significant flow separation as the flow convects from the bottom of the fuselage to the lower ramp.

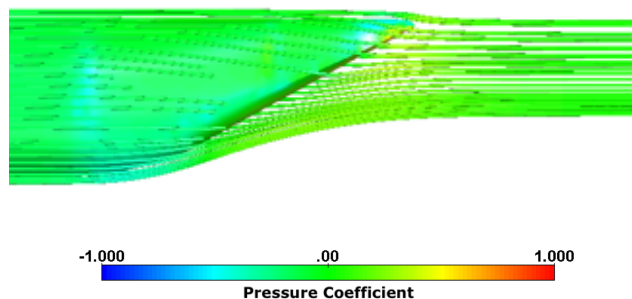


Figure 8.5 Streamlines around the aerodynamic empennage



9 Rotor Design

Balto features eight lifting rotors and two forward flight (cruise) propellers optimized for operation in each regime. Both flight regimes' decoupling helps avoid many design challenges, and compromises are seen on proprotors. The hover and cruise regimes are characterized by very different inflow environments. Therefore, having distinct blades for each flight segment permits a more optimal design for each flight mode.

For the hover regime, the inflow angles are small. Hence the optimum blade twist is smaller (compared to that of a forward flight propeller). If lifting rotors were used for axial forward flight (cruise condition), the effective angle of attack would decrease considerably, and more collective input (or more twist) would be required. This is because in the axial flow forward flight regime (propeller mode), the inflow angles are larger, and the ideal design for that flight regime features a higher twist than is expected for lifting or edgewise rotor.

The RFP defines variables that are to be studied in the design space of the lifting rotors and propellers. The constraints include the rotor radius (R), rotor chord (c), single linear twist rate (θ_{tip}), and taper.

9.1 Lifting Rotors

The mission requires the *Balto* to hover for 40 seconds in total, which constitutes about 1% of the entire mission time. As the *Balto* mission flies primarily in cruise, reducing the drag of the stopped propellers was one of the main design drivers for the system. Due to this flight regime consideration, the number of blades was limited to two, as with this rotor configuration, the blades can be stopped so that they are parallel to the freestream velocity (fuselage), minimizing their drag contribution during cruise. In order to reduce the battery power required for the lifting segment of the mission, the design focused on increasing the hover efficiency driven by the minimization of the disk loading (DL). The following subsection describes the design methodology for the lifting rotor design.

9.1.1 Methodology

The blade aerodynamic design was done using an in-house BEMT code described in Section 4.2.

The first step in the design process was to analyze the Mach number and Reynolds number across the rotor disk in hover. While it is not required by the RFP to account for transition from hover to forward flight, the same analysis was done on the lifting rotor in mid-transition. This analysis aimed to understand the flow characteristics in the hover regime for airfoil selection so that the goal of a “flying platform” (i.e., zero vehicle tilt over flight envelope) could be achieved for the passenger (and particularly PRM) safety and comfort.

After analyzing the flow regime, six airfoil families and twelve airfoils were selected for further analysis. These airfoils were selected based on their historical usage and their efficiency in the pertinent flow regime. An initial study was done with XFOIL, as the team was looking to capture the trends in 2D [86]. An investigation was also performed on a rectangular blade planform with dimensions outlined by the initial sizing.

A final three airfoils were selected for further consideration due to their similar results. These final airfoils were characterized using the in-house RANS CFD solver GTsim (see Section 4.1). For both the airfoil values found in XFOIL and GTsim, the Viterna Method [120] was later used to obtain the full sweep of values after separation occurs (-40 deg to +40 deg).

A rotor trade study was performed using the airfoil data obtained from GTsim (to provide C81 tables) and the self-developed S&D BEMT code. The twist rate (θ_{tw}), in-board taper ratio (TR_{in}), outboard taper ratio (TR_{out}), taper ratio transition location (TR_{trans}), and root cutout (R_{cut}) were all varied to achieve the optimal planform based on the constraints provided by the RFP. With a database from the over 500,000 blade planforms analyzed, a sensitivity analysis was performed using JMP software [121] to quantify the influence of each parameter on the rotor performance. From this evaluation, a final blade configuration was



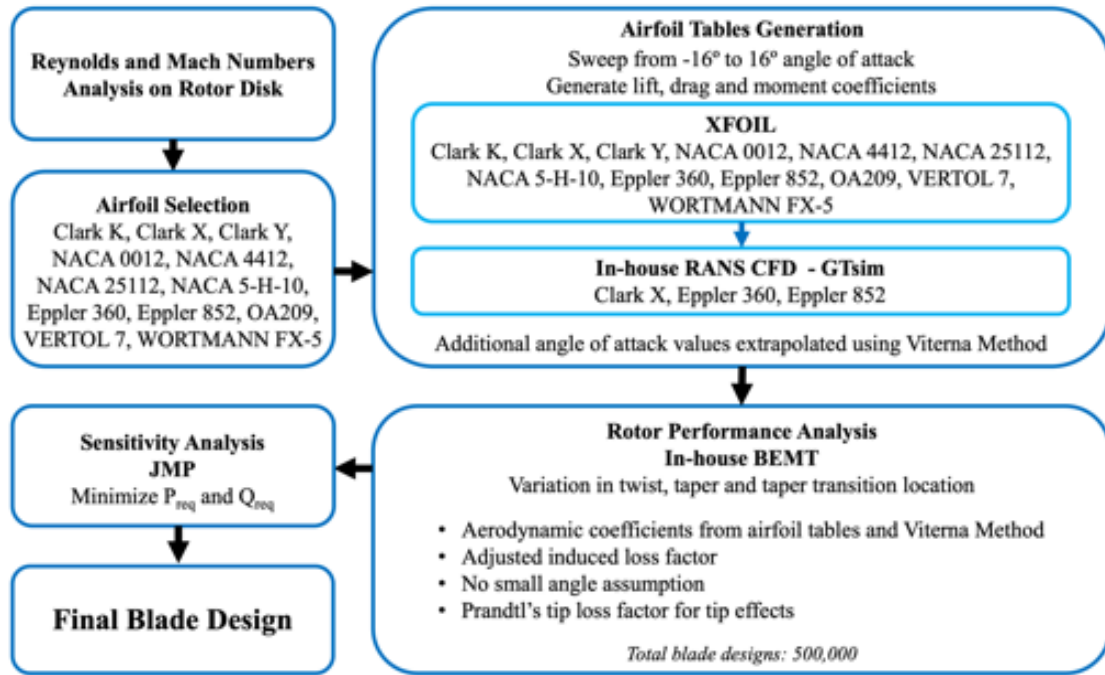


Figure 9.1 Schematic outline of the blade aerodynamic process

selected. The blade aerodynamics design process is summarized in Figure 9.1.



9.1.2 Airfoil Selection

The first step outlined in the methodology (see Section ??) was to characterize similarity parameter ranges over the lifting rotor disk, illustrated in Figure 9.2. The Reynolds number remains above 1×10^6 , which indicates that the airfoil operates in the supercritical range, and C_l and C_d will remain primarily constant across the radius. This change is negligible for the scope of the preliminary design, making it an unimportant design consideration. The Mach number remains below 0.3 ($M = 0.3$) across most of the rotor plane, with the exception of the advancing side blade tip, where the Mach number increases to 0.35 ($M = 0.35$). During transition from hover to forward flight, the Mach number range remains similar to hover due to the slowing of the rotor during this stage. As most of the rotor operates primarily in the incompressible regime with small forays into subcritical regime, the Mach number effects on the airfoil performance are considered negligible for this analysis.

Due to the size of the rotor (about 2 m diameter) and the predominantly uniform flow environment for hover and vertical flight, an airfoil with a high C_l/C_d across the entire blade radius is preferred. While introducing a second airfoil for the tip section of the blade could be beneficial from an aerodynamic perspective, the very low Mach numbers ($M = 0.3 - 0.35$) in the tip sections did not warrant transitioning to a thinner airfoil. Adding a transition region through this short span could overshadow the effects of a modified tip airfoil, also driving up manufacturing complexities and cost. For these reasons, maintaining the same airfoil throughout the radius of the lifting rotor blade was the preferred compromise from aerodynamic, structural, and manufacturing perspectives.

As described in Section 9.1.1, twelve airfoils across four families were selected for analysis. The selected airfoils feature a thickness-to-chord ratio (t/c) between 8% and 14%; this thickness range generally provides a higher C_l/C_d at lower angles of attack experienced in hover. In addition to the thickness-to-chord ratio, the zero-lift angle of attack was also investigated to help reduce the geometric twist requirement. Small-rotor aerodynamics have not been explored much in literature, so for the airfoil selection, an analysis of a baseline rotor was done in parallel using the BEMT code developed by the team. For the 3D case, a rectangular planform, two-bladed rotor with the radius prescribed by the self-developed sizing code was used. The rotor was equipped with the chosen airfoils, and their performance metrics were compared. The results of this analysis are shown in Figure 9.3. This approach enabled accurate prediction of the rotor and airfoil trends needed for the high-level selection.

Figure 9.3 (a) compares the lift-to-drag ratio of the airfoils (XFOIL data). The NACA 4412, Clark X, Clark Y, and Wortmann FX-5 have the best lift-to-drag ratio in the operating range of a conventional hovering rotor. Figures 9.3 (b) and (c) show how these airfoils perform with the previously described baseline rotor. This stage aimed to maximize power loading for a given disk loading and minimize the torque coefficient at a specific thrust coefficient. This analysis shows that the Eppler 360, Eppler 385, and Clark X provide the best rotor performance at the hover design point for the given rotor size.

After the initial study was completed, RANS CFD analysis using GTsim confirmed the trends and provided more accurate quantitative data. Figure 9.4 presents the C_l/C_d of the final three airfoils. The operating range was selected from historical data and computed for the rotors in the preliminary design. Figure 9.4 (a) shows that the Clark X and Eppler 852 airfoils have very comparable performance. The primary difference is that the C_l/C_d of the Eppler 852 has a sharp decrease past its maximum value, while the Clark X maintains its value and decreases with a smaller gradient. A smoother decline is beneficial, as

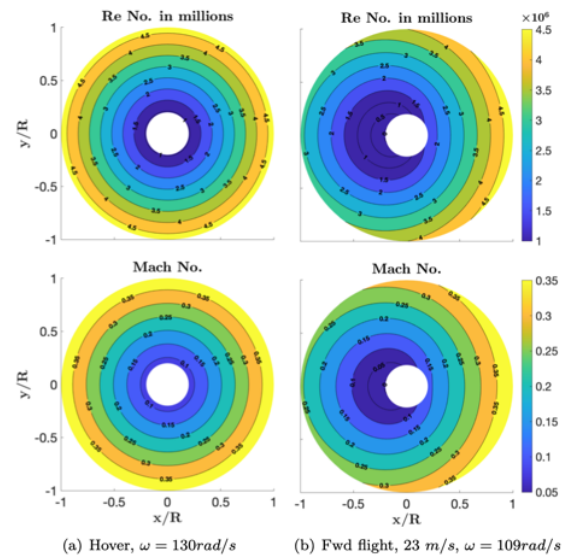


Figure 9.2 Reynolds and Mach numbers on lifting rotor disk for hover and transition speeds



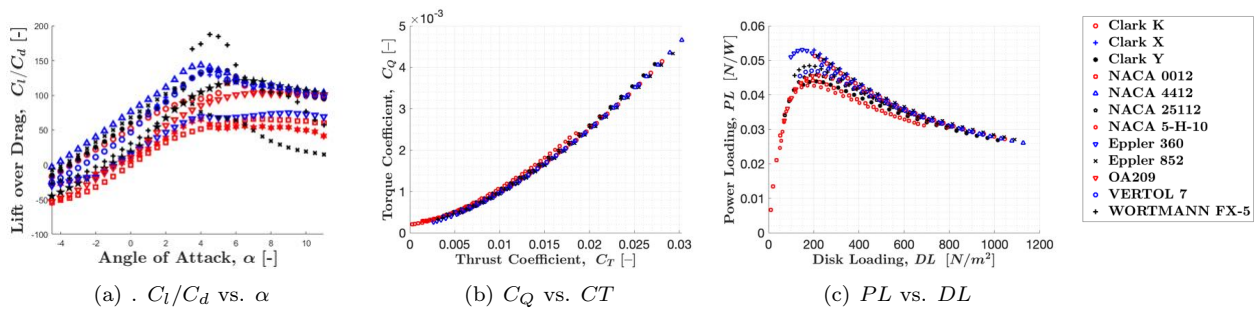


Figure 9.3 Performance characteristics for different airfoils

there may be instances during flight where the lifting rotor will be operating outside the defined angle of attack range shown.

The pitching moment was also of concern in the design as it directly impacts the lifespan of the blade. Results of the study of the effect of pitching moment coefficient are presented in Figure 9.4 (b). The Eppler 360 had the lowest pitching moment, but it is significantly poorer C_l/C_d in the operating range, eliminating it as the final airfoil. Ultimately, the Clark X airfoil was selected for the configuration. The C_l/C_d performance was comparable to the Eppler 852, but it had a lower pitching moment coefficient, making it the design choice for *Balto's* lifting rotor.

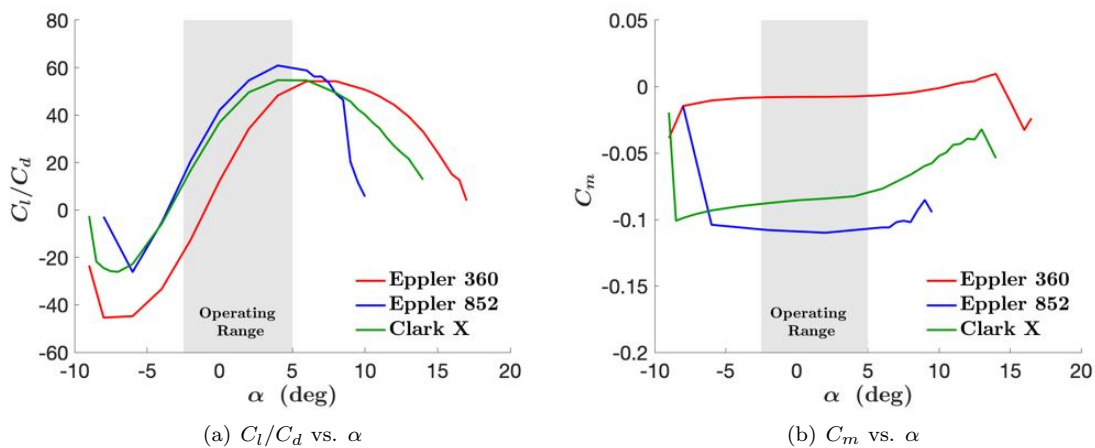


Figure 9.4 Lift-to-drag ratio and moment coefficient for airfoils Eppler 360, Eppler 852, and Clark X



9.1.3 Trade Study

To arrive at the final lifting rotor configuration, a trade analysis was performed as outlined in the methodology section (Section 9.1.1). An exhaustive search was done by varying every parameter in order to obtain a complete picture of the design space. Over 500,000 blade configurations were studied, and the results were compiled in a Pareto front presented in Figure 9.5.

The design point was selected where the Power Loading drops for similar hover Figure of Merit. Both efficiency metrics must be balanced in order to choose an optimal design. Compared to a larger rotor, the Figure of Merit is lower due to the increase of induced power losses caused by the low aspect ratio of the lifting rotors. Thus, the radius of the rotors was maximized at 1.21 m (4 ft), as there was a need for physical distance between each rotor to reduce wake interactions. This constraint led to higher-solidity rotors to maintain a blade loading (C_T/σ) of less than 0.12 ($C_T/\sigma \leq 0.12$).

A sensitivity analysis using the JMP software allowed for an understanding of the effects of individual parameters on the performance of the rotor. The two main factors were the radial twist rate (θ_{tw}) and the outboard taper ratio.

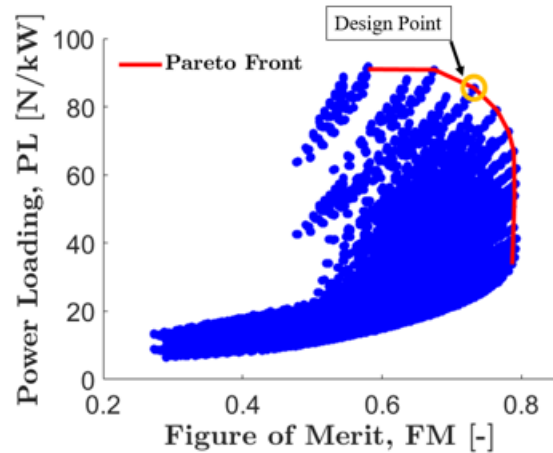


Figure 9.5 Design Space Pareto Front

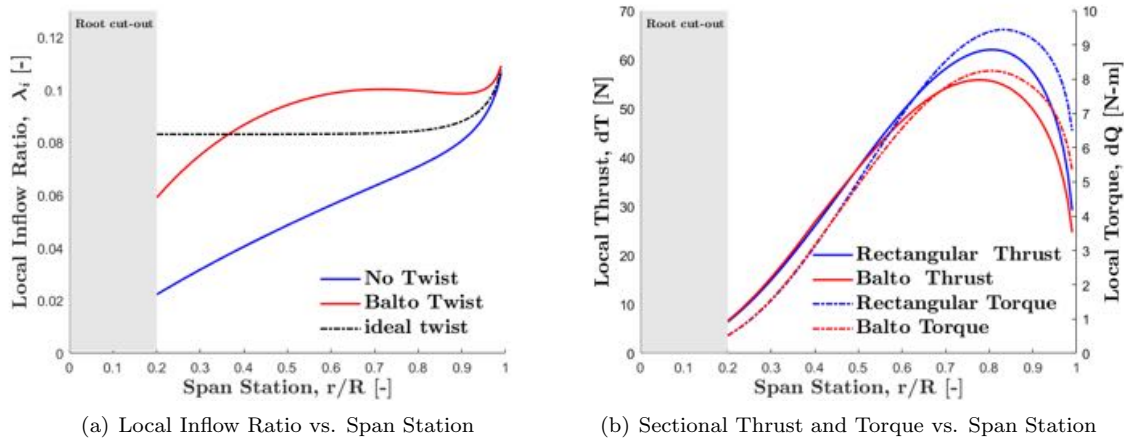


Figure 9.6 Balto's Design Point Blade vs. rectangular untwisted planform

Figure 9.6 compares a baseline rectangular, untwisted blade and the *Balto* optimized design. In Figure 9.6 (a), the application of linear twist to the *Balto* rotor design gave a more uniform inflow across the span. The ideal twist is referenced for comparison. In Figure 9.6 (b), the comparison between the local thrust is shown with the solid lines, while the torque comparison is identified with dashed lines. The designed blade, which has an outboard taper, shows a reduction of 13.4% in thrust relative to the baseline configuration, while the torque is also decreased by 17.72%. This improved reduction in torque increases the overall performance of the rotor and hence the vehicle.

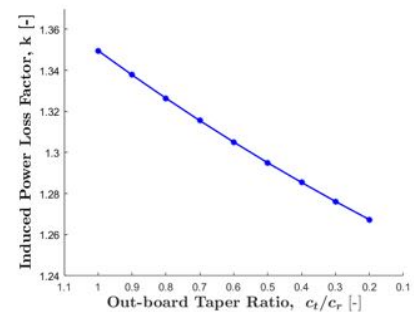


Figure 9.7 Induced Power Loss vs. Out-board taper ratio



The *Balto* lifting rotors have a bi-linear taper that was used to maximize the length of the rectangular planform on the blade inboard while minimizing tip losses and relieving the effects of the induced power factor, k , towards the tip. Figure 9.7 shows the effect that the outboard taper ratio has on this factor. As noted previously, this factor is higher than for conventional rotors due to the short blade aspect ratio. In Figure 9.7, the trend indicates that the induced power factor decreases significantly with taper ratio. The factor is reduced from 35% to 30.5% at the design point, effectively decreasing the power required for the same thrust by 5%. The final planform is discussed in the next Section.

9.1.4 Final Lifting Rotor Design

Balto's final lifting rotor configuration is a two-bladed design that features a linear twist and bi-linear taper for enhanced hover performance while having a low profile during the cruise stage. The Clark X airfoil, an improved version of the classical Clark Y, is applied across the entire radius, thus making the manufacturing of the blade simpler and more cost-efficient. The overall geometry of the blade is illustrated in Figure 9.8.

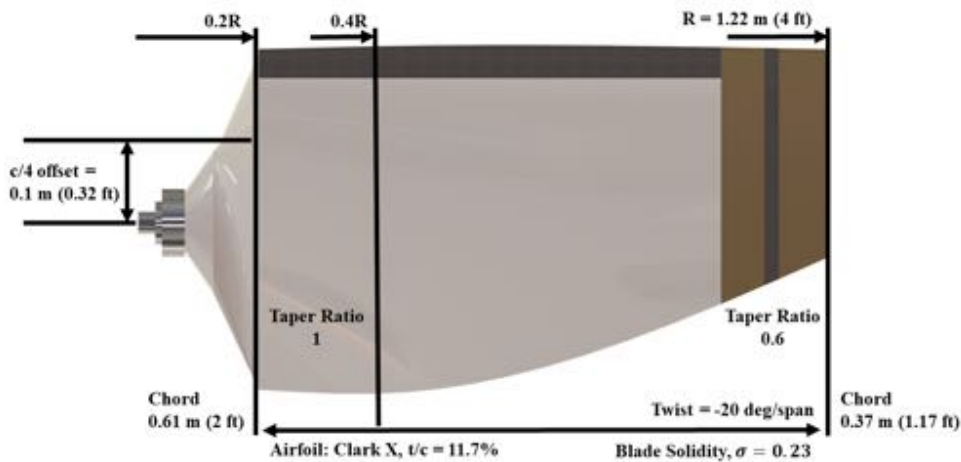


Figure 9.8 Blade Geometric Characteristics

The blade features an offset from the quarter chord line to alleviate the loads on the hub. As noted in Section 9.1.2, the Clark X has a nose-down pitching moment in the operating range of the rotor. This offset alleviates the torsional hub-load by 70% in the hovering condition due to the moment created by the thrust vector. The blade also has a bi-linear taper ratio that transitions at 40% of the radial station from 1 to 0.6 towards the tip of the rotor. A linear twist was applied to the span for increased efficiency in the hovering regime.

The performance metrics are outlined in Table 9.1.



Characteristic	Value (SI)	Value (English)
Tip Speed (Hover)	158 m/s	520 ft/s
Disk Loading (DL)	622 N/m ²	13 lb/ft ²
Power Loading (PL)	43.30 N/kW	7.27lb/HP
Blade Loading, C_T/σ	0.0965	0.0965
Induced Power Factor, k	1.305	1.305
Figure of Merit (FM)	0.74	0.74
C_T	0.0247	0.0247
C_Q	0.0028	0.0028
C_P	0.0036	0.0036

Table 9.1 Lifting rotor performance characteristics

9.2 Cruise Propellers

The two propellers on the *Balto* are the source of thrust during cruise portion of the mission. *Balto* spends over 80% of the mission time in this stage, making efficiency at cruise speed one of the main design drivers. (The RFP does not call for forward acceleration requirements.) The propellers on the *Balto* are capable of operating with variable pitch and with variable RPM, making it stand out from other UAM vehicles in its weight class. Having a completely independent cruise configuration permits the *Balto* to operate as a "flying platform" without any vehicle tilt in any flight stage, to ensure maximum comfort and safety for the PRM (that are generally more sensitive to loads on the body induced by any maneuvers). For the design and analysis of the propellers, an in-house propeller BEMT code was developed that is capable of taking into account high angles of attack and swirl effects produced in the wake. This code was validated against experimental data reported in McCormick [122].

9.2.1 Airfoil Selection

The initial airfoil analysis for the hovering rotor airfoil selection (Section 9.1.2) was also applied for the propeller airfoil. The analysis and historical data showed that due to its high lift-to-drag ratio, high $C_{l_{max}}$, and a low helical blade tip Mach number (so that compressibility effects would be secondary), the Clark series airfoils are used for the design. Further analysis explored new variations of the classical Clark Y airfoil, the Clark X, and Clark K airfoils.

Figure 9.9 compares the XFOIL generated data for all the variations considered. As with the lifting rotors, XFOIL was first applied in this preliminary stage to capture the trends, and then the data were refined and quantified using GTsim, an in-house URANS CFD solver (described in Section 4.1). When comparing the $C_{l_{max}}$, all airfoils performed the same. The figure indicates that Clark X has a higher C_l/C_d over most of the operating range, so it was selected as the propeller airfoil. The Clark X airfoil has a t/c of 11.7% and a camber of 3.3% at 40% of the chord.

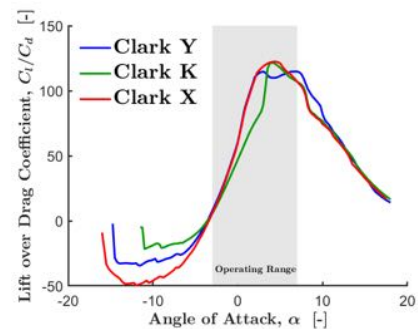


Figure 9.9 C_l/C_d vs. α

9.2.2 Trade Study

Similar to the analysis for the hovering rotor (Section 9.1.2), an exhaustive search across all the defined parameters was done to hone towards the most optimal planform. The trade space was limited by the RFP to the following parameters: radius (R), chord (c), inboard and outboard taper ratio (TR1 & TR2), taper ratio transition location (TR_{loc}), linear twist (θ_{tw}), and the tip speed (ΩR). During this analysis, over 300,000 blade configurations were analyzed and compared to maximize the propulsive efficiency during cruise. Further analysis near the design point fine-tuned the planform and maximized the propeller performance. While taper is studied in the design space, its purpose in this propeller design is to increase the overall efficiency of the propeller by helping with the compressibility effects as the helical tip Mach number is 0.38



at the cruise speed.

Propeller Radius:

The first parameter that was analyzed was the propeller radius. While a larger propeller usually provides better efficiency, the *Balto* maximum radius is capped at 1.2 m (3.84 ft) due to the location of the lifting rotor booms. The design point provided by the exhaustive search mentioned above identified a rotor with a radius of about 1 m (3.2 ft).

Figure 9.10 presents the analysis of the effects of varying the propeller radius at the cruise speed and RPM setting outlined by the initial analysis. The plot indicates that the efficiency is maximized at a propeller radius of 1.05 m (3.36 ft) and then drops for larger radii; the effect on performance is primarily observed when the propeller radius is smaller. The difference in performance between 1 m (3.2 ft) and 1.05 m (3.36 ft) is almost negligible (<0.1%). Therefore, the radius was kept to 1 m (3.2 ft) to save weight and for the propeller tips to be further away from the booms supporting the lifting rotors, reducing aerodynamic interactions.

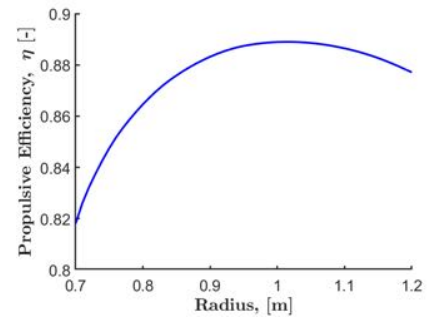


Figure 9.10 η vs. radius

Rotational Speed:

Unlike other propeller-driven aircraft, *Balto*'s system provides a variable pitch and variable RPM control regime that permits higher efficiency over an extended operational envelope. Figure 9.11 (a) depicts the overall efficiency of the propeller at the cruise rotational speed, while Figure 9.11 (b) shows the thrust produced at these speeds and collective settings and then matches it to the required thrust by the vehicle at the quoted advance ratio. From these figures it is seen that a constant rotational speed across the operational envelope of the vehicle will result in a variation of the propeller efficiency between 70% and 90%. While Figure 9.11 (a) purports an overall efficiency of 90% at the higher advance ratios, the thrust produced at that efficiency point is less than the required thrust. Therefore, if the rotational speed is kept constant and if the produced thrust is matched for the flight condition, the propeller propulsive efficiency is maxed out at 85%.

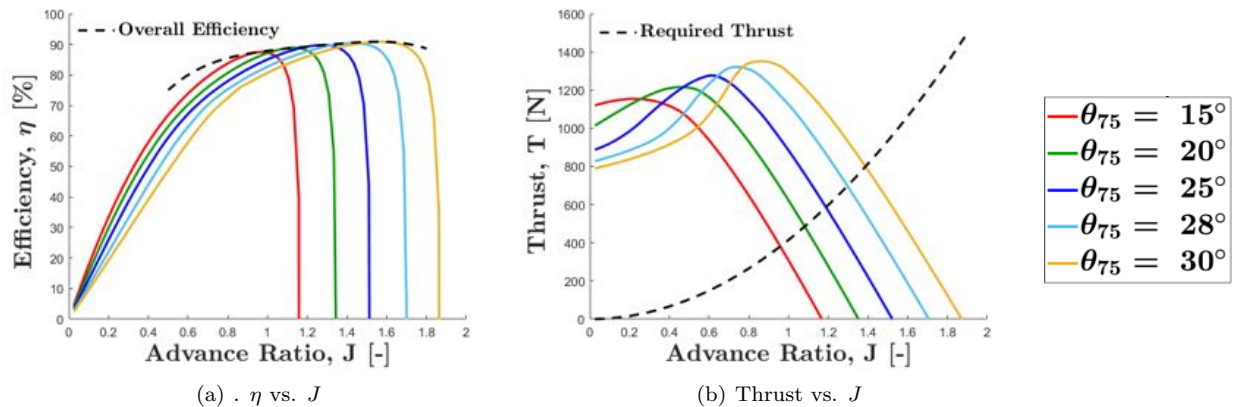


Figure 9.11 Operation in cruise condition, $\Omega = 120 \text{ rad/s}$

To take advantage of the variable RPM capability of *Balto*, a study explored the optimization of efficiency through the variation of rotational speed. Figure 9.12 illustrates how rotational speed changes affect the propeller efficiency at a given forward flight speed. By taking advantage of this variable RPM capability, *Balto* can

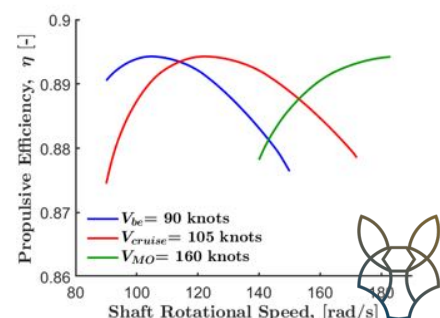


Figure 9.12 η vs. Rotational Speed. Collective trimmed to required thrust

maintain an efficiency of 89.4% across its operational cruise envelope.

Twist:

The effect of twist was investigated using the self-developed propeller BEMT code. Figure 9.13 shows the effect that the twist rate across the radius of the blade has on overall propulsive efficiency in the cruise condition.

The twist rate can enormously impact the performance due to the higher inflow angles experienced at high-speed axial flights. From Figure 9.13, it can be seen that the overall gains in performance plateau for a twist rate of greater than 50 degrees. This is in line with theory that outlines that the best efficiency will be obtained when the twist approaches a hyperbolic rate [122]. The *Balto* planform has a twist rate over the radius of the blade of -50 deg/R from the root to the tip for maximum efficiency in forward flight.

Taper Ratio:

A bi-linear taper was investigated as part of the trade space for the propeller to help the increase thrust in the in-board Section of the blade while reducing the torque in the outer portions.

Figure 9.14 presents the findings of this trade study. Due to the low helical Mach number of the blade ($M_h = 0.38$ in cruise), the effect that taper has on the efficiency is minimal. Overall, applying a taper ratio to reduce the size of the chord at the tip helps increase the overall efficiency, while increasing the chord in the inboard sections reduced the efficiency slightly for this propeller.

An exhaustive combination of possible inboard/outboard taper ratios was done to design the optimal planform shape. It was found that for *Balto*'s twist rate, an optimal planform shape has an inboard taper ratio of 1.5 with an outboard taper ratio of 0.4 starting at a transition location of $0.3R$.

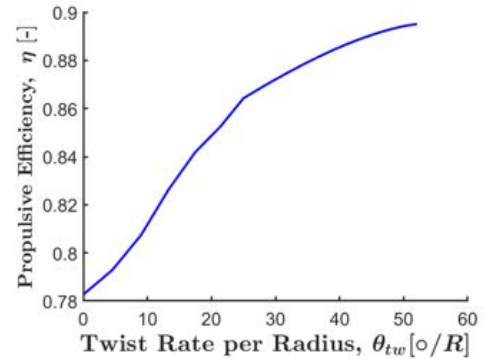


Figure 9.13 η vs. Twist Rate over Radius

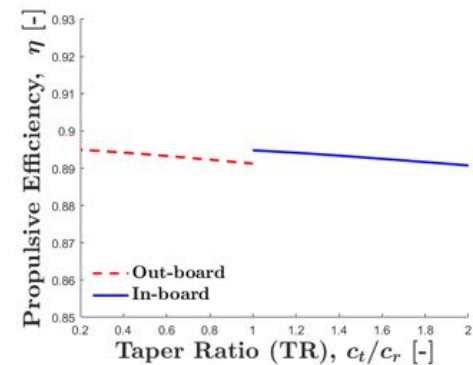


Figure 9.14 η vs. Taper Ratio (in-board & out-board)

9.2.3 Final Propeller Blade Design

Balto's final propeller design features a bi-linear taper and a linear twist across the radius. The design maximizes cruise performance at *Balto*'s design cruise speed of 105 knots. The final planform is outlined in Figure 9.15. The bi-linear taper ratio permits the maximization of lift in the inboard section where the rotational speeds are lowest while preventing the blade from stalling. The 50-degree twist over the radius provides a more uniform inflow across the radius, even with the high inflow angles.

The performance of the blade is outlined in Table

9.3 Hub Design

Balto features three different hubs for the variable RPM, variable pitch lifting rotors, and the variable pitch cruise propeller. Due to the relatively short radius of both the lifting rotors and the cruise propellers, the blades are attached directly to the hub without any hinges. A DC electric servo motor directly actuates the pitching mechanism through a set of 90-degree miter gears. The main design drivers for this device



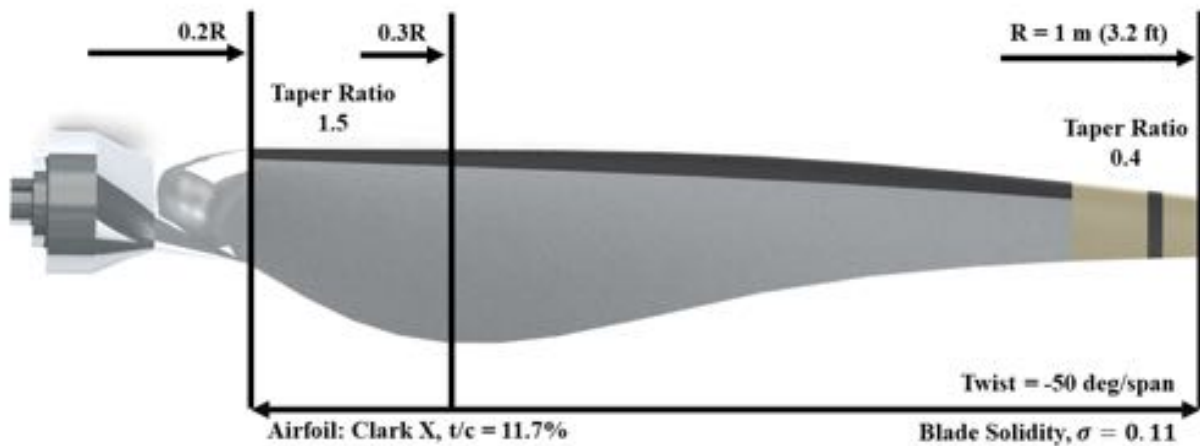


Figure 9.15 Propeller Blade Geometric Characteristics

Characteristic	Value (SI)	Value (English)
Tip Speed	120 m/s	393.7 ft/s
Helical Tip Mach Number, M_h	0.38	0.38
Advance Ratio, J	1.42	1.42
Propulsive Efficiency, η	0.89	0.89
Thrust Coefficient, $C_{T_{Prop}}$	0.136	0.136
Torque Coefficient, $C_{Q_{Prop}}$	0.034	0.034
Power Coefficient, $C_{P_{Prop}}$	0.215	0.215

Table 9.2 Cruise Propeller Performance at $V_c = 105$ knots

are mechanical simplicity and weight. This is achieved through the simple actuation system and material selection for weight optimization.

Lifting Rotor Hubs:

The lifting rotors have two hub configurations: variable pitch and constant pitch. Both configurations feature the same structure for streamlining the manufacturing process. The constant-pitch hubs have fixed attachment points instead of miter gears on the blade attachment points. The attachment point to the blade remains the same through the configurations. The blades are attached to the hub through an aluminum shank that transfers all the torsional and bending loads produced by the lifting rotor. Due to the absence of cyclic control, the hub experiences less transient loads than a conventional helicopter rotor, thus reducing its complexity.

The variable pitch hub, seen in Figure 9.16, features an aluminum casing with three miter gears and a DC electric servo for actuation. The gears are mounted on bearings to reduce friction and ensure precise transmission of movement to the blades. The 42A5-FX Parallel Shaft DC Gearmotor [123] coupled with an integrated 2:1 gearbox is used as an actuator for the system. This servo is self-locking which is beneficial in the case of a failure and steady-state operation since it does not have to be powered continuously. Due to the quarter-chord offset built into the shank, during hover, the effective torsional load at the hub is +15 N-m, giving the servo a margin of 150% to operate. The servo can provide a rotational speed of 126 degrees per second, providing quicker response than needed for emergency operations or other outlined maneuvers.

Cruise Propeller Hubs:

The cruise propellers feature a variable pitch mechanism on both propellers. The system resembles the system shown for the lifting rotor but with the capability to actuate four blades seamlessly. The actuation



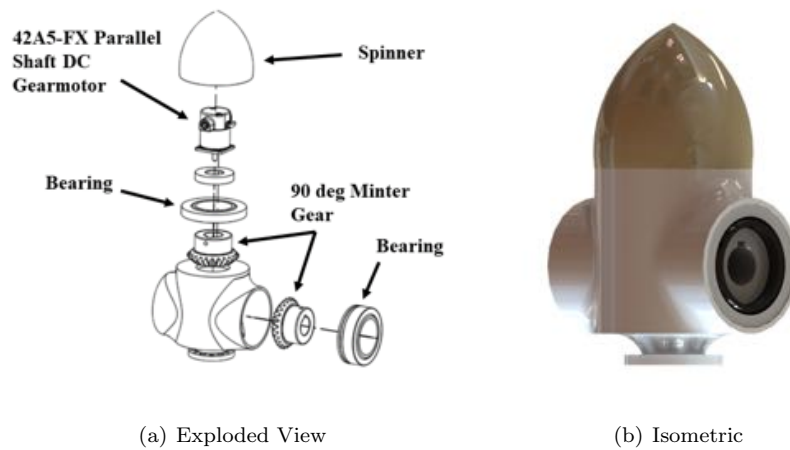


Figure 9.16 Hover Variable Pitch Mechanism

system is the same as the lifting rotors as the load requirements are fairly similar. Analysis shows that the servo has an operating margin of 60% at V_{MO} , and the rotational speed of the 42A5-FX Parallel Shaft DC Gearmotor provides enough speed for maneuvers. Having the miter gears ensures that all blades respond at the same rate. This reduces the transient loads that might be experienced by the hub. The system is shown in Figure 9.17.

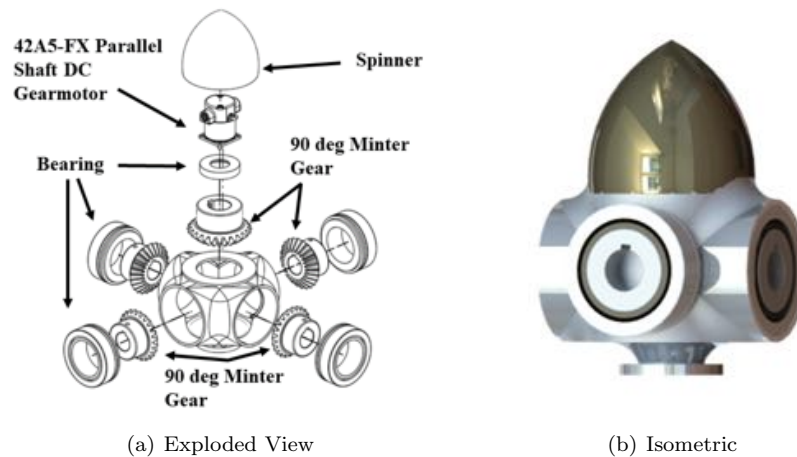


Figure 9.17 Cruise Variable Pitch Mechanism

Material Selection:

Weight optimization of the mechanism was of primary concern in the design. An analysis was done to reduce the weight of the miter gears being used in the system. Three materials were considered: Carbon Steel, Aluminum, and Nylon 66. The Carbon Steel and aluminum miter gears are readily available in the market, while the Nylon 66 are by order only. Previous studies have compared the three materials for usage in steering gearboxes and have proven that Nylon 66 was a good alternative [124]. The pitch-link application is fairly similar, which prompted the investigation. The study was modeled after the model/methodology presented in [124], and the results are shown in Table 9.3.



Characteristic	Carbon Steel 1144)	Aluminum 6061	Nylon 66)
Gear Weight	1.82 kg (4.02 lb)	0.63 kg (1.38 lb)	0.27 kg (0.50 lb)
Tensile Strength (Ultimate)	448 MPa (65 ksi)	310 MPa (45 ksi)	93.1 MPa (13.5 ksi)
Tensile Strength (Yield)	379 MPa (55 ksi)	276 MPa (40 ksi)	90 MPa (13.1 ksi)
Lubrication Needed	Yes	Yes	No
Bending Stress less than pinion stress	Yes	Yes	Yes
System Weight Reduction	-	-97.40%	-155.55%

Table 9.3 Material Comparison for Variable Pitch

The Nylon 66 material presented the required strength to operate under the limiting conditions that the pitch mechanism would experience during flight. The main pitfall of Nylon is its poor performance and tear in hot environments or high-speed operations. In the case of the variable pitch mechanism, the environment is not thermally challenging, the loads are usually steady, and the rotational speeds are low, generating a perfect environment for the N66 gears. The lifespan of these N66/P66 gears has been studied in controlled environments and quantified to be between 10^4 to 10^6 cycles [125]. While this is lower than other metals commonly used in gears such as aluminum, the self-lubrication, more cost-effective nature of the material, and the noise reduction due to less friction make these gears perfect for this application. An FEA analysis was done to corroborate the hand calculations and ensure that the material would not fail under the limit load case. The results are shown in Figure 9.18. The FEA showed that under limited load condition, the margin of safety was found to be 105 %.

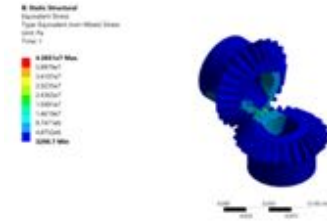


Figure 9.18 Nylon 66 Miter Gear FEA Cross-check

System Weight Overview:

The overall weight of the variable-pitch system was reduced by 155% with the implementation of the Nylon 66 miter gears. The other components were left constant as they are either off the shelf or industry standard. The housing of the mechanism is made out of aluminum 6061 and has an overall weight of 2.26 kg (5 lb), the 42A5-FX Parallel Shaft DC Gearmotor has a weight of 6.8 kg (15 lb) [123], the miter gears a weight of 0.26 kg (0.58 lb), and the bearings are 0.09 kg (0.2 lb). The overall weights of the variable-pitch configurations are reported in Table 9.4.

Lifting Constant Pitch	Lifting Variable Pitch	Cruise Variable Pitch
3.17 kg (7 lb)	9.62 kg (21.2 lb)	10.52 kg (23.2 lb)

Table 9.4 Total weight per pitch mechanism for all rotors

9.4 Blade Structure

Balto features similar blade sizes for both the lifting rotors and the cruise propellers. Due to this, the internal blade structure is shared across both types of blades to streamline the sourcing of parts and expertise through the manufacturing process. The blade structure has a carbon fiber spar with a square cross-section. The cross-section has rounded edges to improve the tolerances in the manufacturing process [126]. A circular cross-section was not selected as it would require more structure to attach to the skin of the airfoil. The core of the blade is made of Rohacell foam that provides the structure while adding minimal weight. This composite has been widely used in the aerospace industry, and it is a proven technology. The skin of the blade is made with $+/- 45$ deg carbon fiber layers that provide enhanced torsional stiffness for the blades. Finally, an erosion cover is put on the leading and trailing edges of the blade for enhanced protection. Figure 9.19 provides a visual representation of the description above.

To ensure good structural integrity, FEA was performed on both the lifting blades and the propeller blades. In both cases, the maximum loads that the blade would experience during operation plus an added 1.5 safety factor were applied. The results are shown in Figure 9.20. As the critical stresses occur on the



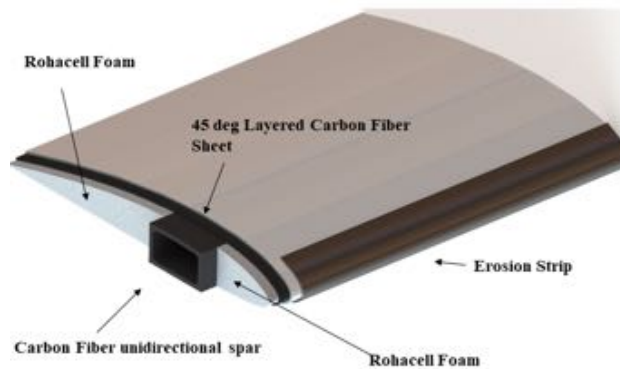


Figure 9.19 Blade Structure

carbon fiber of the cruise propeller blade, the material exhibits a safety margin of 57% under the critical condition. The lifting rotor blade had a safety margin of 60.14% under critical conditions.

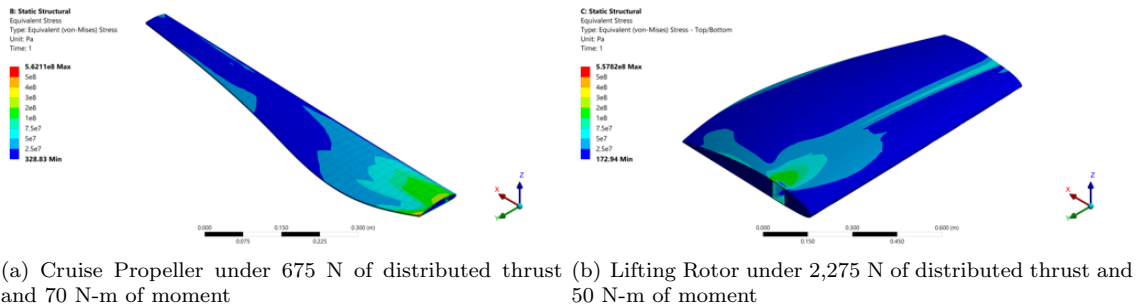


Figure 9.20 FEA Analysis for Blades

The designed blade structure proved to exceed the *Balto's* operational envelope providing additional safety. The final weights of the blades and the complete rotary system are shown in Table 9.5.

	Lifting Rotor		Cruise Propeller	
	Value (SI)	Value (English)	Value (SI)	Value (English)
Blade weight	4.78 kg	10.52 lb	1.2 kg	2.63 lb
Number of Blades	2	2	4	4
Rotor weight	9.56 kg	21.03 lb	4.79 kg	10.54 lb
Number of Rotors	8	8	2	2
Total	76.5 kg	168.28 lb	9.59 kg	21.09 lb

Table 9.5 Rotary System Weight

9.5 Lifting Rotor – Cruise Propeller Interaction in Transition

The interactional aerodynamics between the lifting rotors and the cruise propeller during transition has also been evaluated to ensure that the design will not encounter situations that may lead to higher vibratory loading or potential attitude changes. The analysis was accomplished using the FlightStream 4.5 software.



While the software does not capture the total effects from the wake interaction with the aft lifting rotors, it provides an accurate wake path, which is sufficient for the (design-stage) analysis intended here.

Figure 9.21 illustrates the wake interaction between the rotors. The front lifting rotors have less influence and interaction with the cruise propellers than the cruise propeller wake with the aft lifting rotors. From Figure 9.21 it can be appreciated that the cruise propeller wake affects half of the rotor disk of both aft rotors. In an initial iteration, the rotational direction of the aft propellers was set in a way that the convected wake of the rotor would increase the reverse flow region of the lifting rotor significantly. This would have a negative effect on the performance and the vibratory loads on the rotors. Therefore, for the final design, the rotational direction was set so that the advancing side of the rotor disk was aligned with the cruise propeller wake. While this interaction still creates a small thrust imbalance, it has significantly less impact on the blade's performance. In this configuration, the retreating side of the blade remains isolated from the wake interaction. This is important for the ride quality of the passengers, but also to minimize fatigue and associated costs during its life cycle

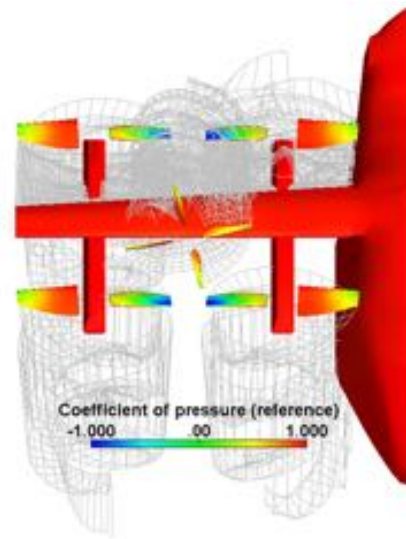


Figure 9.21 Wake interaction during transition flight, $V = 27\text{m/s}$

10 Aerodynamic Wing Design

Balto is designed to take off vertically and transition to level forward flight with no pitch change. It features a single propeller-blown wing that acts as the primary lifting device during cruise, and the main anchor point for the lifting rotors and propellers. While the wing generates most of the lift during cruise, it is also the most significant contributor to drag during axial flight. Therefore, the wing design must maximize the cruise performance while minimizing the planform area. Two main constraints present design challenges: (1) *Balto* must fit in a 15 m (50 ft) square footprint per the RFP; and (2) the lifting rotors and propellers must fit within the allotted footprint with minimal interaction. The following section details the wing aerodynamic design and methodology. Structural aspects of the wing are discussed in Section 11.4.

10.1 Airfoil Selection

Accounting for over 80% of the mission, *Balto*'s primary flight condition is cruise; therefore, it was paramount that the wing be designed to have high aerodynamic efficiency. Choosing an airfoil with a high lift-to-drag ratio C_l/C_d is the initial point for designing the wing. As safety and comfort of passengers during flight is also a primary concern when developing *Balto*, the final airfoil must have good stall characteristics (i.e., delayed or gentle stall) in particular pitching moment. Airfoils with a high thickness-to-chord ratio were also considered, as the design objectives called for efficiency in forward flight. The NACA 4412, Douglas/Liebeck LNV 109, Douglas/Liebeck LA 203, Wortmann FC 74-C15-140, and the Eppler E423 met the initial requirements and were further analyzed.

The initial step of the design process employed XFOIL, [86] to analyze the trends of the five airfoils at a Reynolds number of 3.5 million, *Balto*'s cruise Reynolds number. While the LNV 109 and the FX 74 had the



Parameter	Minimize/ Maximize	Weight
Root chord	N/A	-
Planform Area	-	3
L/D_i	+	4
C_M	-	2
Struct. Weight	-	1

Table 10.1 Wing planform parameters weights

Span		c_r/c_t			
		1	0.8	0.6	0.4
m	ft				
12.5	41	0	10.2	25.3	31.9
13.1	43	26.2	36.4	53.5	60.6
13.7	45	47.1	57.4	76.9	85.3
14.3	47	65.3	75.8	98.3	108.2
14.9	49	82.7	93.4	119.0	130.6

Table 10.2 Wing planform trade study results in percent

highest C_l/C_d , stall characteristics were abrupt, and thus they were discarded. Of the remaining airfoils, the NACA 4412, the LA 203, and the E423 presented the highest C_l/C_d values for airfoils with slower stall. Both were selected for a more detailed analysis using GTsim, an in-house state-of-the-art CFD solver described in Section 4.1.

Figure 10.1(a) confirms that the LA 203 and E423 airfoils have comparable C_l/C_d peaks. While the E423 airfoil reaches peak C_l/C_d at a lower angle of attack, the magnitude of its moment coefficient in Figure 10.1(b) is higher than the LA 203 airfoil, and it presents a less favorable drag bucket. Minimizing the moment coefficient was essential not to introduce more forces into the wing structure. The team selected the LA 203 airfoil for *Balto*'s wing based on its drag bucket, maximum L/D , and consistent and mild pitching moment over the cruise angle of attack range.

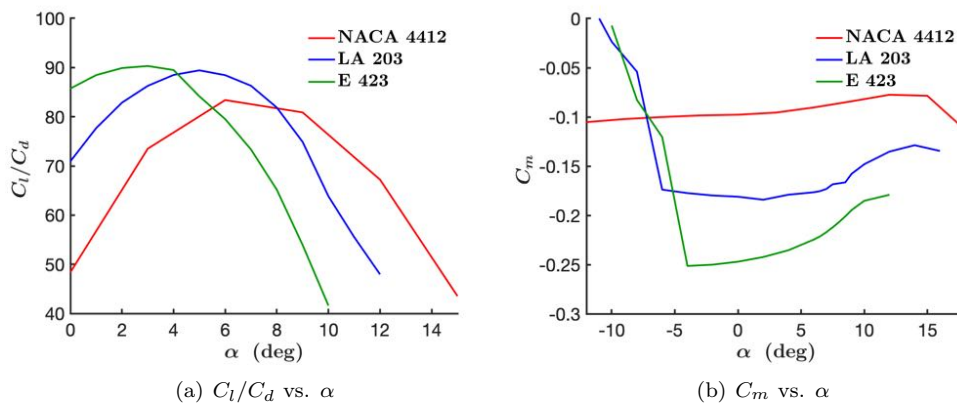


Figure 10.1 Lift-to-drag ratio and moment coefficient for airfoils NACA 4412, LA 203, and Eppler 423

10.2 Trade-study on Wing Planform Design

An in-house code was used to obtain possible planform designs for the wing. Further, AVL was used to derive wing data. Taper ratio and span values were varied and input into the code. For each combination, the lift was computed for a sweep of wing chords until the lift produced by the wing was equal to 110% of the GTOW at *Balto*'s cruise speed. Rotor-blown effects of the tractor propellers were included in the calculations. More than 400 wing planform variations were analyzed.

A trade study was then conducted on the resulting planforms. Four characteristics were observed and weighted to obtain a more accurate comparison: (1) overall planform area, (2) lift to induced-drag ratio, (3) pitching moment coefficient, and (4) associated structural weight. Each parameter was rated from 1 to 4, 1 being the least important and 4 being the most important (Table 10.1).

The smallest rectangular wing planform was chosen as the baseline for the trade study. Results of the trade study (Table 10.2) are provided as a percentage increase/decrease from the baseline. AVL and XFOIL



data were analyzed to capture the trends with a low computational cost. Aerodynamically, the most efficient planform would have been one with the largest span and the lowest taper ratio. However, manufacturability, structural considerations, and rotor placement constrained the taper ratio to be higher than or equal to 0.6, as any lower would present significant structural constraints. Due to the lifting rotor arrangement, the wing span was optimized for minimal bending moment arm of the outer lifting rotors and high aerodynamic efficiency. The selected planform, highlighted in blue in Table 10.2, scores higher than the baseline without sacrificing structural feasibility. The selected planform is 13.1 m (43 ft), with a taper ratio of 0.6.

10.3 Final Wing Design

The final wing design of *Balto* employs the selected wing planform described in Section 10.2 and illustrated in Figure 10.2. A dihedral was added for added control stability (see Section 14). Winglets were added at the tip of the wing to increase aerodynamic efficiency. These winglets reduce the induced drag produced on the wing, increasing the L/D of the wing. Moreover, the effective wing aspect ratio increases from 9 to 13, following the methodology outlined by Ref. 127.

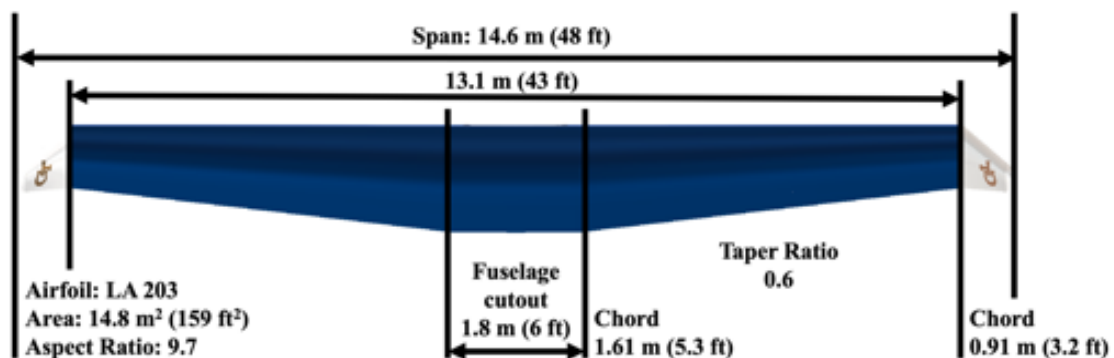


Figure 10.2 Velocity magnitude contours of the wing without and with propeller-induced flow at 105 knots

The wing planform was analyzed in FlightStream at the cruise velocity of 54 m/s (105 knots). Per Table 10.3, the wing (analyzed alone) only produces 21,515 N (4,837 lb) of lift, which is lower than the required 24,000 N (5,500 lb) of lift. When the propellers are added, modeled using an actuator disk, the propeller-induced flow over the wing increases the lift by 13% to reach 27,185 N (6,111 lb). This is 15% greater than the required lift for TOGW. The wing has an $L/D = 13$. The velocity magnitude contours at cruise speed are shown in Figure 10.3.

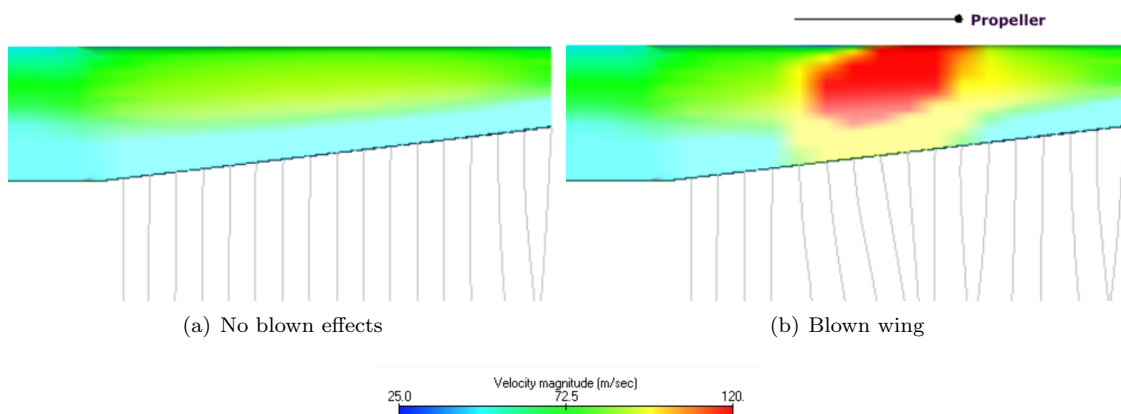


Figure 10.3 Velocity magnitude contours of the wing without and with propeller-induced flow at 105 knots



Propellers	C_L	C_D	L		D		L/D
			N	lb	N	lb	
Off	1.0	0.08	21,515	4,837	1,659	373	13
On	1.3	0.10	27,185	6,111	2,117	476	13

Table 10.3 Wing aerodynamic properties at 105 *knots* forward speeds without and with propeller-induced flow

11 Structural Design

11.1 Limit Load Definitions

To identify the loads associated with various maneuvers outlined in the RFP [5], limit loading conditions are defined following the procedure described in Section 15.6. The lift generated from the lifting rotors and/or the main wing are defined such that they meet the required accelerations at the aircraft's maximum weight. The loads and their corresponding locations on the aircraft are highlighted in Figure 11.1.

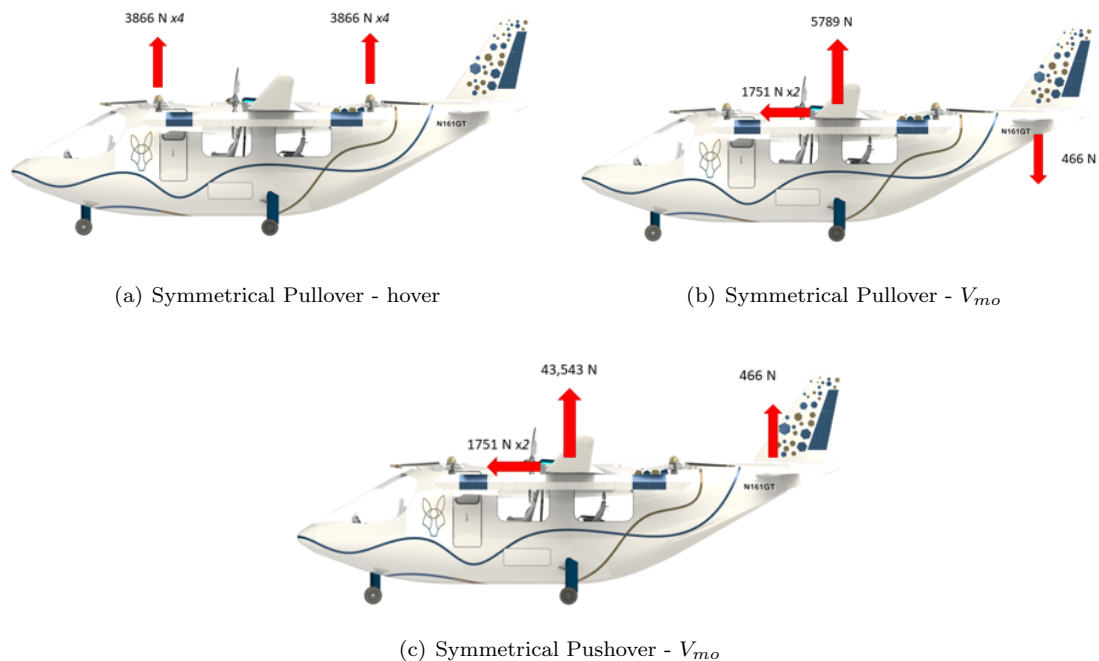


Figure 11.1 The magnitudes and locations of the loads in the three limit maneuver loading conditions

In the limit gust conditions, the aircraft is assumed to be subject to 9.1 m/s (30 ft/s) vertical gusts in level flight in compliance with 14 CFR 29. The gust induce a significant change in aerodynamic forces and moments; therefore, they need to be evaluated to ensure the physical integrity of the vehicle. To determine the change in aerodynamic loading, the procedure outlined in Ref. 128 is used.

The vehicle mass ratio and gust alleviation factors are given by:

$$\mu_g = \frac{2(W/S)}{\rho M G C_{L,\alpha}} \quad (1)$$



$$K_g = \frac{0.88\mu_g}{5.3 + \mu_g} \quad (2)$$

With these, the gust load factor is given by:

$$n_g = 1 + \frac{K_g U de V C_{L,\alpha}}{498(W/S)} \quad (3)$$

Finally, the lift is obtained as:

$$L = n_g W \quad (4)$$

Using Equation 11.1, the loads expected for the *Balto* encountering a 9.1 m/s (30 ft/s, upwards) transverse gust at cruise speed are $L = 41,591$ N ($L = 12,343$ lb) on the main wing. These calculations are repeated for the tail horizontal stabilizers and the negative gust. The remaining resultant forces acting on the aircraft are visualized in Figure 11.2.

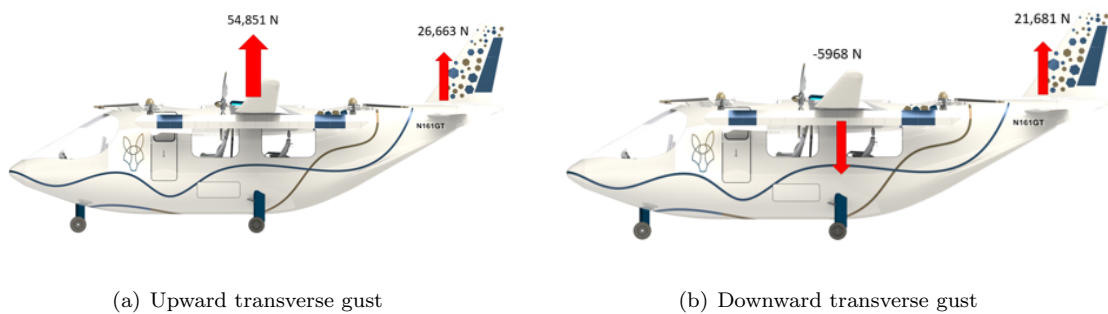


Figure 11.2 The magnitudes and locations of the loads in the two transverse gust conditions

Landing load conditions, both with max vertical load and with drag load, are also defined and presented in Figure 11.3. Furthermore, the hover rotors generate a lift equal to 2/3 of the maximum gross weight. The maximum vertical loads are obtained from the load-stroke curve as defined in Section 11.5.2.

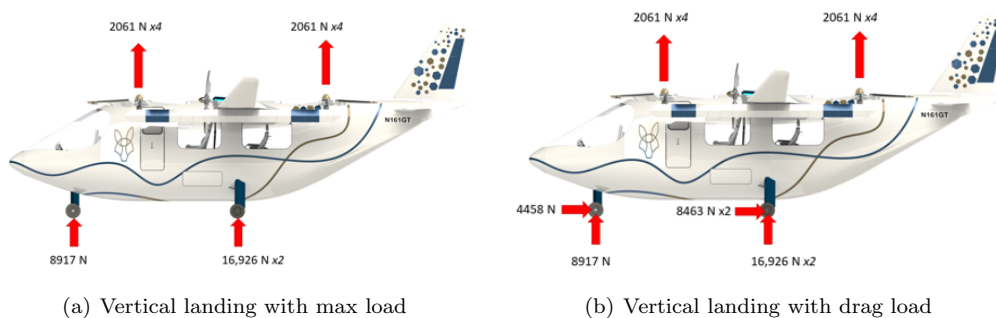


Figure 11.3 The magnitudes and locations of the loads in the two landing load conditions

In addition to the limit load definitions described in the RFP [5], an additional limit loading condition is developed to represent a rotor failure during hover. This condition assumes the failure of an outboard rotor which would induce the highest torsional moment on the wing. In response, the lost thrust is evenly distributed throughout the remaining 7 rotors. The resultant load on the aircraft is thus 3534.40 N (793.66 lb), acting vertically on all rotors locations except that of the outboard aft lifting rotor. While this condition is unlikely to occur due to the strong redundancy in our design, the assumption lets us assess the impact of force imbalance on the structural integrity of the vehicle.



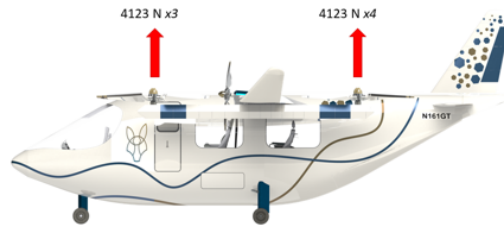


Figure 11.4 The magnitudes and locations of the loads in the rotor failure condition

11.2 Shear and Moment Diagram

Once the flight characteristics were defined for the aircraft, the different limit load conditions could be applied to the fuselage. The fuselage structure was simplified as a thin-walled Aluminium cylindrical body and the forces were applied at their respective locations to generate the shear and bending moment diagrams for the fuselage as presented in Figure 11.5.

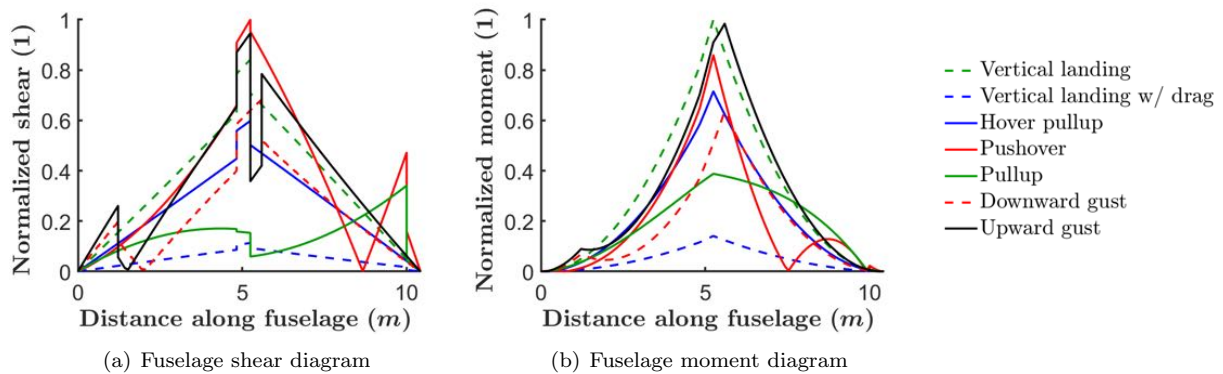


Figure 11.5 Total shear and bending moment diagrams for all seven limit loading conditions

As seen in the figure, it was observed that the most severe load conditions are the two landing loads and the upward gust condition in V_{mo} of 82.30 m/s (270 ft/s). In all of the limit load conditions, both shear forces and bending moments are most concentrated in the location of the nose and main landing gears and the wing. As such, it was deemed that these components and their connections to the fuselage to be the most critical sections to focus our design efforts and analyses.

11.3 Airframe Design

The *Balto* airframe model was designed in Solidworks [129]. The design consists of a total of 8 bulkheads joined by keel beams as seen Figure 11.6. Of the bulkheads, the two near the center of the aircraft are greater in thickness in order to provide the structural integrity needed to house the wing box attachment and the main landing gears. One near the nose is also reinforced for sufficient strength to house the nose landing gear. The remaining bulkheads were strategically placed to accommodate cabin necessities such as doors, windows, and checked bag storage. Thin separators were also placed for separation between the cockpit and the cabin.

Two sets of a pair of keel beams run along both the base and the ceiling of the airframe. The bottom keel beams support the floor, which will mount multiple passengers, their mobility aids, and possibly medical equipment. These are merged with the ramp support beams for better load distribution throughout the



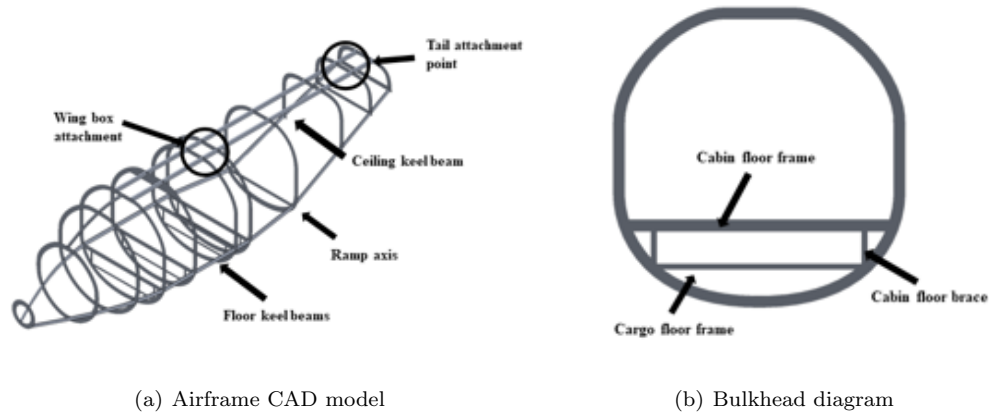


Figure 11.6 Airframe CAD model and description of different locations on the bulkhead cross-section

entire aircraft. As the wing, and consequently the wing box, is subjected to various types of high magnitude loads as discovered in Figure 11.5, a double keel beam is placed across the top of the aircraft to maximize structural support. Furthermore, the flat geometry of the crossbeams eases the incorporation of the ramp system and the tail. While the aerodynamic performance of such a fuselage configuration is not on par with smooth geometries, the addition of a smooth cone at the tail acts to mitigate the issue and the team's priority to provide the most optimal experience for PRM is better served with the shape. The upper double keel beam also provides a location for the triple joint to connect the horizontal and vertical stabilizers of the aircraft.

Aluminum-lithium alloy (2050-T84) was used for the bulkheads and keel beams. The material boasts a significantly higher yield strength (476 MPa, 69 ksi), Young's modulus, corrosion resistance than many currently available aluminum-based alloys, making it an ideal low density and high damage tolerance balance solution with great potential for weight reduction [130].

The CAD model was imported to ANSYS AIM 19.1 for finite element analysis [90]. All limit loading conditions were explored to ensure the structural integrity of the aircraft. The three most highly loaded cases are visualized in Figure 11.7 and all remaining results are outlined in Table 11.1. It was found that the airframe has a 14.15 % margin of safety at the highest loaded condition of vertical landing with drag loads, even with the loads being multiplied by a safety factor of 1.5 per RFP requirements [5].

Limit load condition	Max stress		Max stress location Material	Margin of safety
	MPa	ksi		
Vertical landing - max load	315.99	45.83	Landing gear box (Al-Li alloy)	50.64 %
Vertical landing - drag load	417.47	60.55	Landing gear box (Al-Li alloy)	14.15 %
Symmetrical pull-up - hover	59.78	8.67	Keel beam (Al-Li alloy)	696.25 %
Symmetrical pushover - V_{mo}	79.38	11.51	Keel beam (Al-Li alloy)	499.65 %
Symmetrical pull-up - V_{mo}	19.51	2.83	Keel beam (Al-Li alloy)	2339.77 %
Downward gust	77.44	11.23	Keel beam (Al-Li alloy)	514.67 %
Upward gust	108.49	15.72	Keel beam (Al-Li alloy)	338.75 %
Rotor failure	276.19	40.06	Bulkhead (Al-Li alloy)	72.35 %

Table 11.1 Maximum stresses and locations on the airframe at different limit load conditions



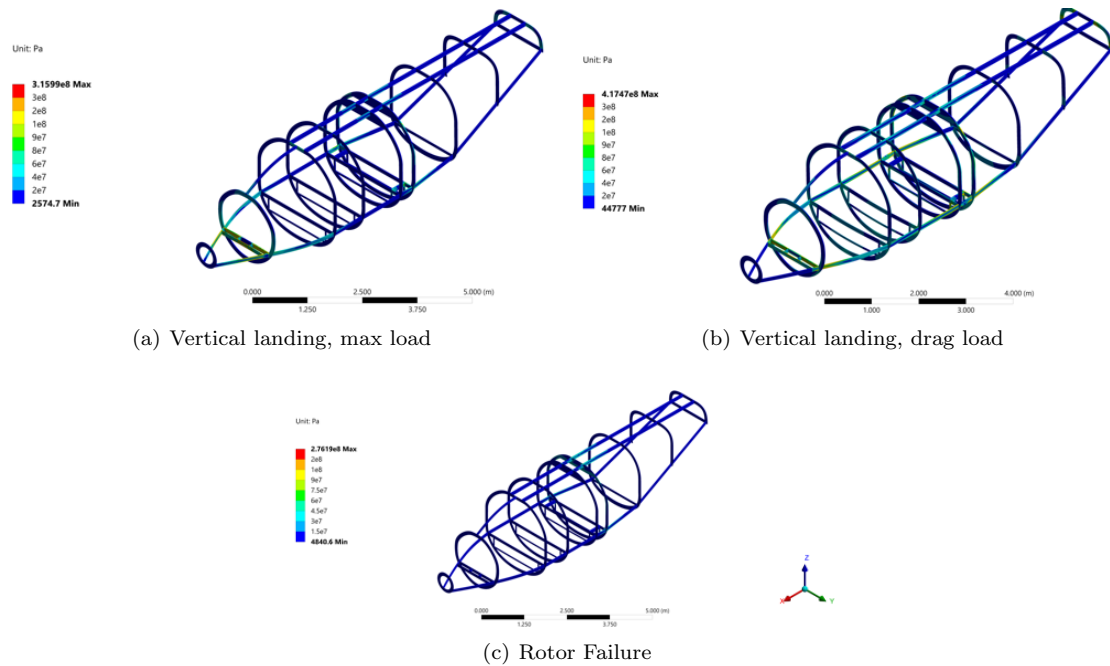


Figure 11.7 The Equivalent Von-Mises stress of the airframe at the three heavily loaded conditions: vertical landing with max load, vertical landing with drag load, and rotor failure. All loads are multiplied by safety factor of 1.5. All units are in Pascals.

11.4 Wing Structural Design

11.4.1 Wing Spar

Balto's wing acts as a lifting surface for the aircraft in cruise as well as the supporting structure for the cruise propellers and the lifting rotors. These lift/thrust devices span the entire wing and exert significant loads on the main spar. At different stages of the mission, the contributions from the individual load-inducing components vary drastically. Figure 11.8 shows all three different configurations of wing loads during hover, cruise, and transition.

In hover, only the lift from the lifting rotors exert forces on the wing. Figure 8(a) indicates that the two transverse point loads along the span create a bending moment about the \bar{i}_2 axis. The distances of each lifting rotor from the quarter-chord are not equal. The asymmetry results in a torsional moment about the \bar{i}_1 axis. In the cruise configuration (Figure 8(b)), the lift is generated solely from the wing, creating a bending moment about the \bar{i}_2 axis. This is the type of load a typical fixed-wing aircraft would undergo during flight. In addition to the distributed load, the thrust from the cruise propeller creates a bending moment about the \bar{i}_3 axis. During the early low-speed portion of the transitional phase (Figure 8(c)), the wing does not generate sufficient lift from the forward velocity of the aircraft to maintain flight, and thus the lifting rotors are incrementally slowed as forward flight speed increases. Consequently, the wing will experience forces from both lifting and cruise conditions. The magnitude of each individual component of forces should be smaller than either of the other two cases, as the lift is shared by both the wing and the lifting rotor, however.

The wing thus experiences significant bending moments from all three primary directions, of which the main spar must be capable of withstanding, in addition to loads from varying maneuvers with a safety factor of 1.5 per RFP requirements [5]. Meanwhile, the weight of the wing structure must be minimized. An analytical study was performed on three different possible configurations of the main spar: the box beam, the I-beam, and the C-section. The specific dimensions of each configuration can be seen in Figure 11.9.



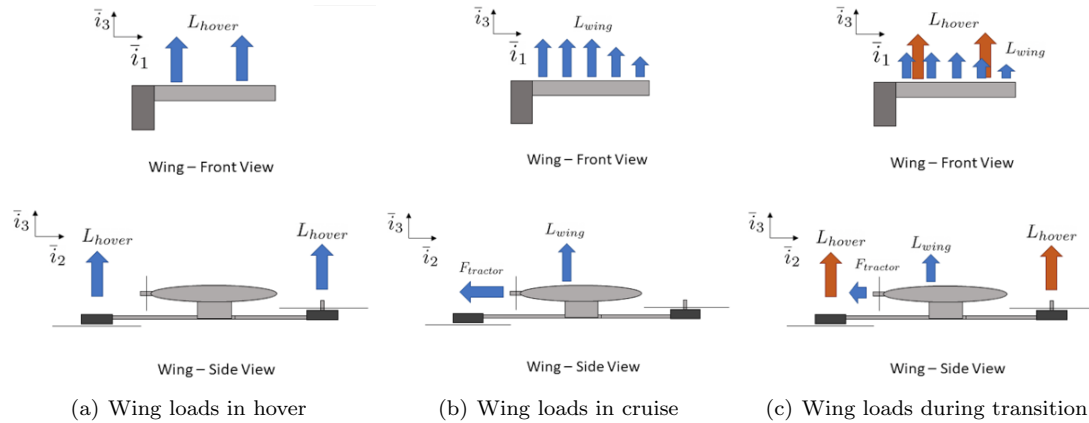


Figure 11.8 The types of loads that the wing experiences at various flight regimes

The goal of the study was to maximize the bending stiffness at the centroid per unit mass in all three axes ($H_{11}^c, H_{22}^c, H_{33}^c$).

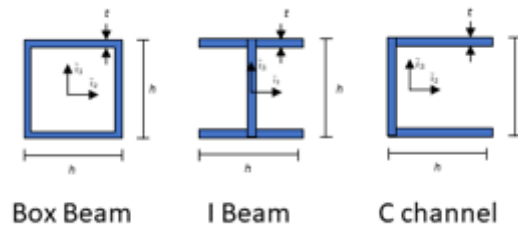


Figure 11.9 The dimensions for the three candidates of main spar cross-section

The results of the study are portrayed in Figure 11.10. The box beam outperforms the other two types significantly in bending stiffness about the \bar{i}_3 axis (bending by the cruise propeller). The difference in performance is even greater for the torsional stiffness about the \bar{i}_1 axis, as the box beam's stiffness is orders of magnitude greater than those of the other beams, as expected of a closed cross-section. While the bending stiffness about the \bar{i}_2 axis is not the highest, it remains on par with the other two configurations. Therefore the box-shaped cross-section was selected as the main spar. In our design, torsional stiffness is a critical property due to the presence of the lifting rotors front and aft of the wing. The magnitude of this torsional moment can further be exacerbated in case of failure of a single hover rotor, which may be a source of total structural failure of the main spar for the other two cross-sections. The selection of the box beam addresses this concern.

Aluminum lithium alloy (2050-T84) was used for the main spar, and to improve the structural efficiency of the box beam structure, a carbon uni layup with the spar caps were used in order to maximize the distance between the caps. The two shear webs attached to the spar caps (forming an enclosed box) were constructed with ± 45 degree cloth centered with the spar caps and ± 45 degree carbon cloth sandwiched between PVC foam for the skins.

11.4.2 Motor Boom

The motor boom is attached to the main spar of the wing and must support the forces generated by each lifting rotor. The hexagonal cross-section enables the division of the boom into two sections for optimal space utilization. The top section houses the motor and the motor shaft, while the lower half encases the electronic devices for the power train such as wiring and ESCs. As the beam undergoes a significant bending



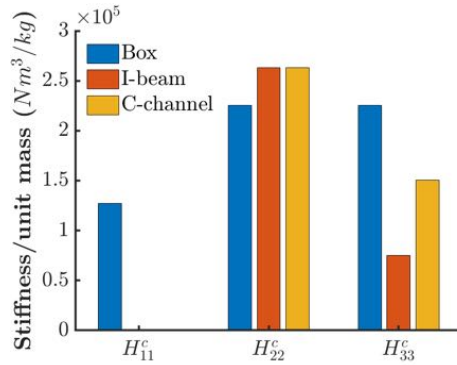


Figure 11.10 The bending stiffnesses in all three directions for the main spar cross-section candidates

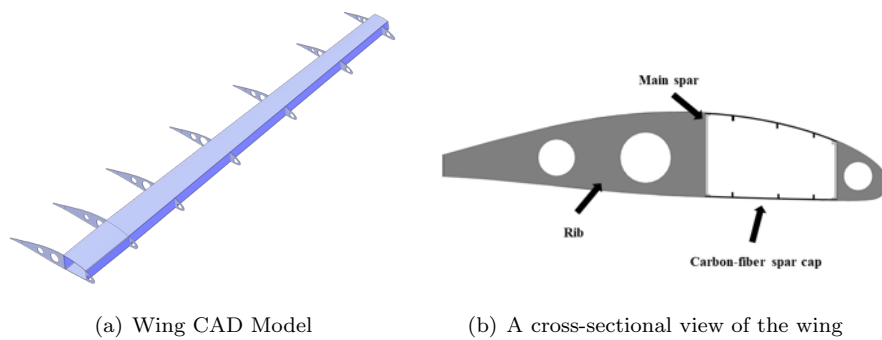


Figure 11.11 Wing CAD model and description of different locations on the wing cross-section

stress in hover and transition from hover to cruise, a truss structure is introduced to the beam in order to maximize the strength to weight ratio. The truss members are built from unidirectional carbon fiber-epoxy composites arranged in ± 45 degree angles, which have been found to be optimal for carrying both shear and torsional loads [131].

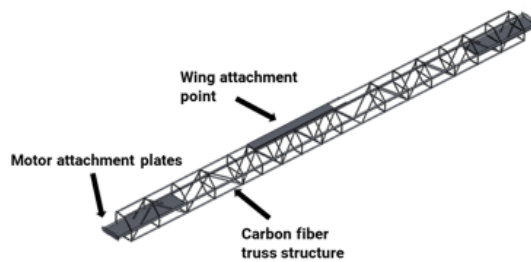


Figure 11.12 An isometric view of the motor boom structure. The wing attachment plate is joined to a rib-like structure which is connected to the main spar. The motors are mounted on top of the motor attachment plates on both sides of the boom.

11.4.3 Wing Assembly FEA

Finite element analysis on the assembly of the wing, the wing box structure, and the motor boom was performed to verify the structural integrity of these components together. As with the airframe, all limit loading conditions were explored. The three most highly loaded cases are visualized in Figure 11.13 and all



remaining results are outlined in Table 11.2. It was determined that the wing - wing box assembly has, at its most loaded condition, the safety margin of 13.58 % in addition to the RFP-required safety factor of 1.5.

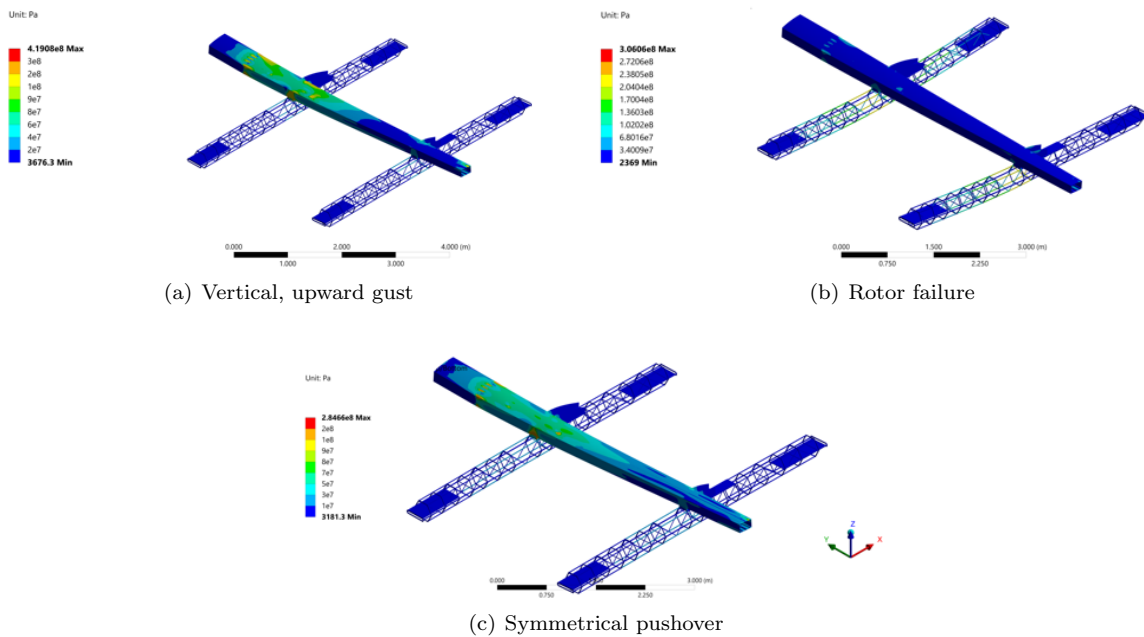


Figure 11.13 The Equivalent Von-Mises stress of the wing assembly at its three most heavily loaded conditions: the upward vertical gust condition, rotor failure condition, and the symmetrical pushover in V_{mo} . All loads are multiplied by safety factor of 1.5. All units are in Pascals.

Limit load condition	Max stress		Max stress location Material	Margin of safety
	MPa	ksi		
Vertical landing - max load	142.18	20.62	Motor boom truss (Carbon fiber)	533 %
Vertical landing - drag load	142.18	20.62	Motor boom truss (Carbon fiber)	533 %
Symmetrical pull-up - hover	286.67	41.58	Motor boom truss (Carbon fiber)	214.49 %
Symmetrical pushover - V_{mo}	284.66	41.29	Wing root (Al-Li alloy)	67.22 %
Symmetrical pull-up - V_{mo}	92.64	13.44	Wing root (Al-Li alloy)	413.82 %
Downward gust	83.16	12.06	Wing root (Al-Li alloy)	472.39 %
Upward gust	419.08	60.78	Wing root (Al-Li alloy)	13.58 %
Rotor failure	306.06	44.39	Motor boom attachment (Al-Li alloy)	55.53 %

Table 11.2 Maximum stresses and locations on the wing assembly at different limit load conditions

11.5 Landing Gear Design

Balto seeks to provide the most accommodating experience for PRM passengers. As such, the design process of the landing gear sought to minimize landing load transfer to the cabin to reduce any risk of spinal injuries of the passengers. The reduction of load transfer is also vital to prevent possible damage to any medical equipment that may be loaded on the aircraft with the passengers. While doing so, the ground clearance of the aircraft should be kept relatively so that the ramp length is minimized while complying ACAA regulations that require the ramp slope to be equal or less than 1:4 [rise]:[run] for assisted boarding [113].



11.5.1 Trade Studies

As part of the process to finalize the landing gear configuration, a preliminary study was conducted comparing the load transfer performance of a skid and a oleo-pneumatic landing gear. A drop test was conducted via an ANSYS explicit dynamic simulation. The undercarriage of a generic vehicle equipped with either a skid or a landing gear was impacted against the ground at a sink speed of 2 m/s (6.56 ft/s). The model of the skid was created in Solidworks and was imported to ANSYS. The wheeled landing gear was modeled as a spring-damper system with a spring constant (k) of 125 kN/m (713.77 lbf/in) and a damping coefficient (c) of $k/20$. Figure 11.14 illustrates the comparison between the acceleration felt by the passengers during impact for each type of landing device.

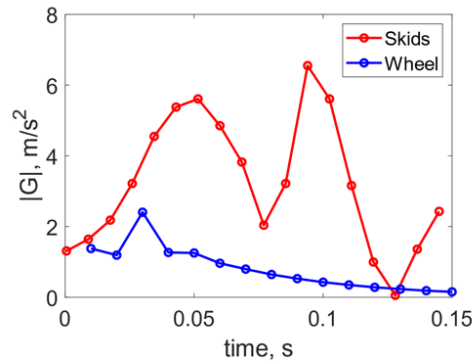


Figure 11.14 The acceleration in terms of gravitational acceleration of the aircraft during impact for the skid and the oleo-pneumatic landing gear

The acceleration experienced by the passengers is much greater for the skid compared to the oleo-pneumatic landing gear. While the skid resulted in a maximum acceleration of 6.559 gs, the landing gear experienced at maximum 2.405 gs. In addition to benefits in passenger comfort, the wheel also provides the added benefit of short landing capability, which improves the overall survivability of *Balto* and its passengers during emergency conditions.

While the oleo-pneumatic landing gear was selected due to its superb performance, another comparison studied the advantages and disadvantages of its retractability. An aerodynamic analysis using FlightStream, as shown in Figure 11.15, compared the C_{d_i} of the non-retractable and retractable configurations. The fuselage with retracted landing gears has a C_{d_i} of 0.104. Without retracting, the fuselage C_{d_i} became 0.133, a 27.64% increase.

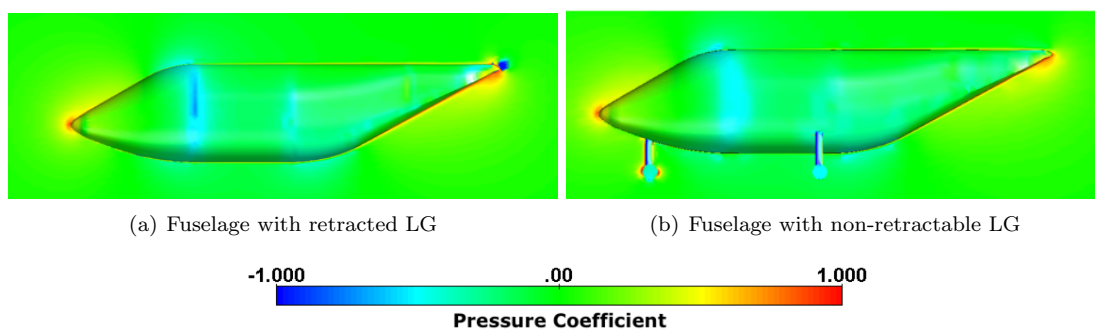


Figure 11.15 The contour plot of the coefficient of pressure around the fuselages of different landing gear retractability conditions at cruise speed of 54.02 m/s (177.22 ft/s)

While there is a noticeable decrease in the aerodynamic performance without retractable landing gears, other points of consideration constrain our configuration choices. As discussed in Section 11.5.2, the long



stroke of the strut required for maximized passenger comfort makes it difficult for the landing gear to be retracted into the undercarriage while maintaining enough space for checked-in baggage and the Stow 'n Go seat storage. Furthermore, retractable landing gears require actuation systems. For critical safety applications, such as the landing gear system, a distribution system along with centralized hydraulic power is required [132]. This severely increases the complexity and the weight of the system.

11.5.2 Landing Gear Characteristics

Based on results from the trade studies, *Balto* includes a three-point (tricycle) non-retractable oleo-pneumatic landing gear. The landing gear struts are extreme energy absorbing with a 0.6096m (2 ft) trailing arm stroke. This type of landing gear has been successfully integrated on the various Carter Aviation Technologies aircraft [133] and have proved their capabilities well. The extremely long stroke allows the landing gear loads to be distributed over the entire stroke and improve passenger experience while landing by minimizing sudden accelerations. This is key for PRM and other disabled passengers. The extreme energy absorption capability comes from the fact that the impact velocity is determined in the first 0.0254 m (0.083 ft, 1 in) of travel and then the needed pressure is applied to maintain a near constant deceleration over entire stroke. The pressure on the piston can be kept nearly constant despite varying impact velocities by loading a spring to the control valve. The technology was verified by drop testing by Carter Aviation Technologies [133, 134]. This behavior is replicated in Figure 11.16. Once the landing gear has fully compressed and the vertical velocity has stopped, the valve immediately closes for a slow rebound. This landing gear can be lighter than conventional gears because the peak loads can be less and evenly spread out over the entire stroke. The additional benefit of the landing gear is that the aircraft and all passengers regardless of their weight will see the same deceleration. This is an important element of the design as the weight of the aircraft can vary significantly depending on the medical equipment loaded onto the aircraft.

The derivation of landing gear behavior follows the procedure outlined by Raymer [135]. Assuming a shock absorber efficiency of 0.85, the resultant gear factor of 0.78 can be obtained at the 2 m/s (6.55 ft/s) sink speed provided in the RFP [5], given that the aircraft is generating a lift force of 2/3 of its weight. The load-stroke curve of the shock absorber at this sink speed for both a conventional single-stage oleo-pneumatic shock absorber (designed following Currey's procedure [136]) and the extreme energy absorbing landing gear is presented in Figure 11.16. The values were obtained assuming the static-to-extended compression ratio of 2.1/1 and compressed-to-static compression ratio of 1.9. These values were chosen to reduce the variation of floor height with aircraft weight. As the resultant gear load factor is much lower compared to conventional aircraft, the EEA permits either a significant weight reduction or improvement in energy absorption performance. The shock absorber, assuming a gear load factor of 2, can withstand up to 4.08 m/s (13.37 ft/s) sink rate. At the RFP's given rate of descent of 2 m/s (6.56 ft/s), the maximum vertical load is found to be 16926 N (3805 lbs). In order to maximize structural strength to withstand the vertical loads while minimizing the volume to reduce aerodynamic drag, Ti-10-2-3 alloy is used. The material has very high strength (0.2% yield strength of 1145 MPa, 166.07 ksi) and has very high fatigue life, making it a suitable material for landing gears [137].

The location of the landing gear was determined using pitch and roll angles for static stability following the design procedure outlined by Currey [136]. The nose landing gear is located 1.2192 m (4 ft) from the nose along the centerline. The main landing gear struts are located 1.2192 m (4 ft) laterally from the centerline. This configuration satisfies the minimum 30 degrees rollover angle with the center of gravity location of four-passenger configuration. Furthermore, the angles permit the locations of the landing gears to be such that they are located outboard from the cabin floor. This minimizes the risk of impact between the passengers in the cabin and the landing gear in case of extreme landing gear failure.

For crashworthiness concerns, the preloaded spring against the valve limits the maximum piston pressure to its yield pressure. This prevents the landing gear from failing in an extreme impact until the maximum energy possible at a constant pressure has been absorbed before yielding which gives the passengers the best chance for minimum injuries and maximum survivability.

The stresses that the main landing gear experiences was analyzed using ANSYS AIM 19.1 [90]. The results can be seen in Figure 11.17 and Table 11.3. It can be seen that the lowest margin of safety is very



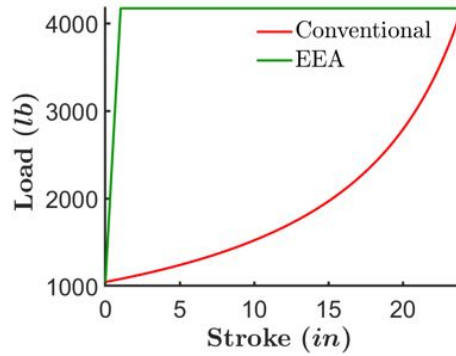


Figure 11.16 The comparison of the load stroke curve for a conventional landing gear and the extreme energy absorbing landing gear (EEA).

high during the vertical landing with drag load condition which indicates that the landing gear is safe at the RFP’s provided rate of descent. The high value of safety margin gives the pilot great flexibility when it comes to emergency landings.

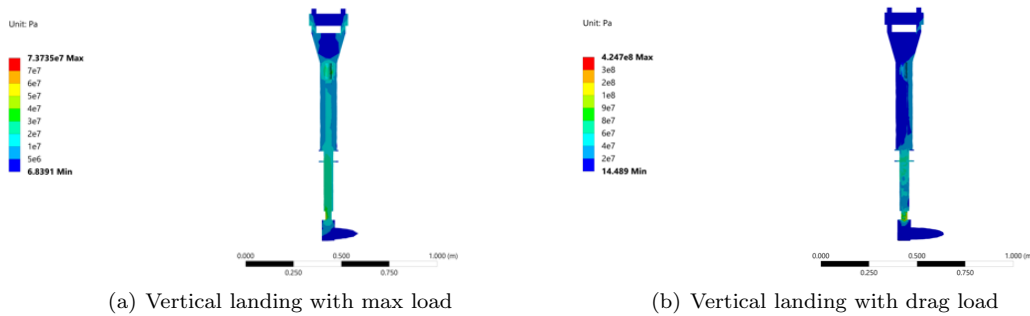


Figure 11.17 The Equivalent Von-Mises stress of the landing gear assembly for the two landing load conditions. All loads are multiplied by safety factor of 1.5. All units are in Pascals.

Limit load condition	Max stress		Max stress location Material	Margin of safety
	MPa	ksi		
Vertical landing - max load	73.74	10.70	Piston (Ti alloy)	1452.75 %
Vertical landing - drag load	627.97	91.08	Piston (Ti alloy)	170.05 %

Table 11.3 Maximum stresses and locations on the landing gear at different limit load conditions

11.6 Fatigue Analysis

While the rotating shaft of the lifting rotors is the most critically loaded rotating component of the aircraft, they only operate 40 seconds throughout the mission. The cruise propeller shaft operates under a much lighter load; however, they are used for 50 minutes. The team decided fatigue analysis should be conducted for both components.

This analysis was conducted using ANSYS AIM 19.1, and the shafts were constructed of structural steel, as shown in Figure 11.18 (a). The shaft material



Parameter	Value (SI)	Value (English)
Material	Structural Steel	Structural Steel
Density	7850 kg/m ³	15.23 slug/ft ³
Young’s Modulus	200 GPa	29007548 psi
Poisson’s Ratio	0.303	0.303
Yield Strength	250 MPa	36259 psi
Ultimate Tensile Strength	460 MPa	66717 psi
Fatigue Strength Index	0.95	0.95

Table 11.4 Shaft material properties

properties are shown in Table 11.4, and the corresponding S-N curve is presented in Figure 11.18 (b). The force and moment loads along with stresses and fatigue of the shaft were first analyzed for each flight segment, then for the entire mission. Equivalent von-Mises stresses were used, while the Soderberg theory for mean stress correction was applied to compute fatigue.

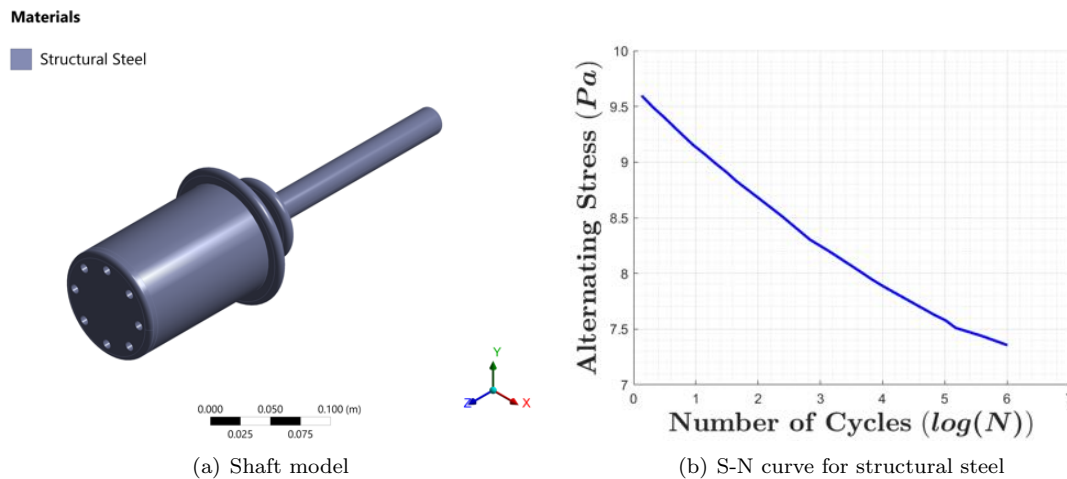


Figure 11.18 Rotating shaft model and corresponding material S-N curve used to determine fatigue damage

The resulting loads, and critical point stresses for each mission segment are given in Table 11.5. Fatigue related parameters including damage, life cycles, and safety factors are given in Table 11.6. The shaft performs beyond the necessary fatigue life of 20,000 missions for all cases.

Parameter	Force		Moment		Stress	
	N	lb	N-m	lb-ft	MPa	ksf
Hover 1	3061.25	688.19	424.4	313.02	22.31	465.95
Axial Climb	3061.25	688.19	480.125	354.12	27.90	582.70
Hover 2	3061.25	688.19	424.4	313.02	22.31	465.95
Cruise Climb	575.2	129.31	205.5	151.57	11.04	230.58
Cruise	759.3	170.70	308.0	227.17	16.46	343.77
Cruise Descent	551.0	123.87	193.3	142.57	10.34	215.96
Hover 3	3061.25	688.19	424.4	313.02	22.31	465.95
Axial Descent	3061.25	688.19	410.5	302.77	25.28	527.98
Hover 4	3061.25	688.19	424.4	313.02	22.31	465.95
Mission	-	-	-	-	58.12	1213.86

Table 11.5 Shaft loads and stresses

The stresses and safety factors for the shaft during the full mission are provided in Figures 11.19(a) and (b), respectively.



Parameter	Damage	Life Cycles	Safety Factor
Hover 1	1.791	670000	3.67
Axial Climb	1.92	625000	2.94
Hover 2	1.791	670000	3.67
Cruise Climb	0.9563	125000	7.47
Cruise	0.026	460000	11.45
Cruise Descent	0.39842	301000	9.25
Hover 3	1.791	670000	3.67
Axial Descent	1.1811	101000	3.24
Hover 4	1.791	670000	3.67
Mission	0.3150	50000	1.50

Table 11.6 Shaft fatigue damage accumulated during each mission segment

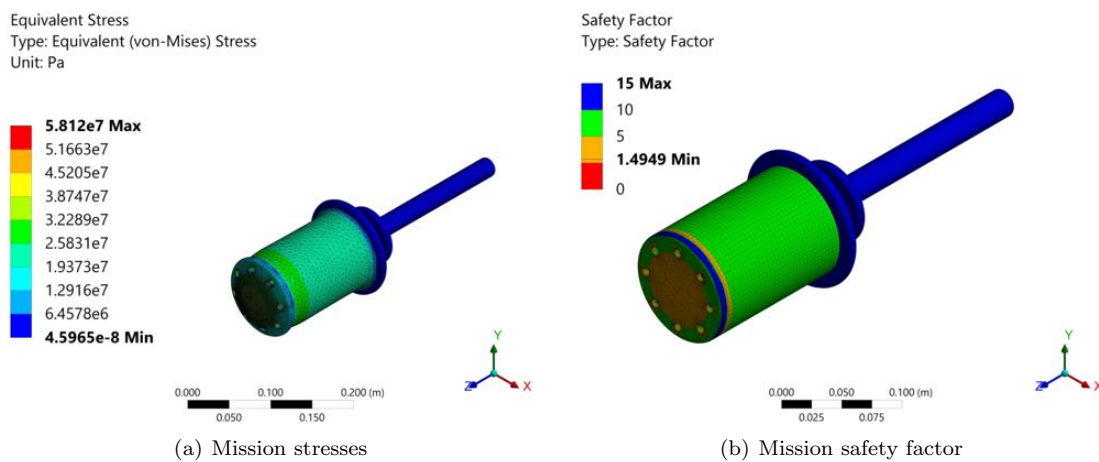


Figure 11.19 Fatigue simulation results

12 Powerplant System

12.1 Battery Selection

As an all electric vehicle, *Balto* will be powered by an ideal battery with a mass-energy density of 400 W-hr/kg (7.83 HP-hr/slug), as designated by the RFP. The mass-energy density means that, for every one kilogram of battery mass, the battery can supply 400 W for one hour (or one slug can supply 7.83 HP for one hour). While the mass-energy density is given, the battery spatial volume must be determined through examination of current technology. As an ideal battery, it is assumed that it does not generate any heat and the state of health remains unchanged during its lifespan. All calculations are made assuming 20 minutes of reserve battery based on battery consumption in the cruise portion of the mission.

Lithium ion (Li-ion) batteries are most commonly used for electric propulsion on both small and large scales. They are composed of cells in which lithium ions move from an electrode to a cathode through an electrolyte. Other battery types exist, such as Lithium Sulphur and Lithium Air, but their low technology readiness levels (TRLs) prevent their use in *Baltos* propulsion system. Lithium Air is still in the initial idea phase (TRL of one) while Lithium Sulphur is in the prototype stages with TRL of four [138]. Thus, Li-ion batteries were explored in more detail for implementation in the configuration.

Li-ion batteries have thermal runaway issues, meaning that they can catch fire if they become too hot. However, since the batteries onboard this vehicle can be assumed ideal (as per the RFP), thermal effects



are not considered. Li-ion batteries do not react well with water. Therefore, it is vital that watertight containment units are used to protect the battery.

The battery design process began with an investigation of potential cathode material types. An initial sweep of current technologies produced a selection of eight materials: Lithium Cobalt Oxide (LCO), Lithium Manganese Oxide (LMO), Lithium Nickel Manganese Cobalt Oxide (NMC), Lithium Iron Phosphate (LFP), Lithium Nickel Cobalt Aluminum Oxide (NCA), Lithium Titanate (LTO), Nickel Cadmium (NiCad), and Nickel Metal Hydride (NiMH). The material selection, and their benefits and drawbacks, is presented in Table 12.1. Important parameters of each material considered were mass energy density (capacity-related run times), mass power density (ability to deliver high currents), power cost density (cost per unit power), safety, performance, lifespan, and charging rate. For each material type an empirical study was conducted, with each parameter rated on a scale from 1 to 5, with 1 and 5 being the lowest and highest scores, respectively.

Parameter	LCO	LMO	NMC	LFP	NCA	LTO	NiCad	NiMH
Mass Energy Density	5	4	5	2	5	3	4	5
Mass Power Density	3	4	4	5	4	4	4	5
Safety	3	4	4	5	3	5	5	5
Performance	4	3	4	4	4	5	1	1
Lifespan	3	3	4	5	4	5	4	4
Cost	4	4	4	3	3	2	3	3
Charging Rate	3	3	5	5	3	5	4	4
Total	25	25	30	29	26	29	25	27

Table 12.1 Potential battery material comparison and selection (from Refs. 139–142)

LFP and LTO were considered to not be feasible options due to their low mass energy density. While having clear benefits, NiCad and NiMH were found to not be suitable due to performance issues. NiCad based batteries suffer from a memory effect: if they are not completely charged after every use, their charge level incrementally reduces, shortening their overall life span. Similarly, despite having a higher capacity and comparable safety level to NiCad and Lithium Ion (Li-ion) based batteries, NiMH based batteries have a weak cell effect. Weak cell effect manifests as quick-dying batteries, even when fully charged. LMO is seen to demonstrate a high power density, but perform poorly in comparison to LCO and NMC. LCO has excellent mass energy density, however, provides comparatively lower power.

After careful scrutiny of the various Li-ion cathode materials, the one chosen for use in the vehicle battery was NMC. NMC is a unique battery that can be tailored to serve as an energy or power cell. It has the second highest mass energy density, 220 kW-hr/kg with only NCA ranking higher at 260 kW-hr/kg. Most importantly it boasts a high safety and lifespan of upwards of 2000 cycles resulting in the best overall battery material. These are the main reason why NMC is one of the most commonly used in Li-ion batteries for electric power train applications today.

Typically, Li-ion batteries employ a graphite anode; however, the future of battery technology appears to be heading in the direction of lithium metal anodes, which would replace the usual graphite anode with a metallic base. A lithium anode gives a larger energy capacity to the battery. While they exist today and can provide the necessary mass energy density stated in the RFP, a metal anode is very volatile, and currently not feasible for electric propulsion. Additional research is also being done on solid state batteries, which replace the liquid electrolyte in Li-ion batteries with a solid medium, increasing energy storage and accelerating charging times. Solid state batteries, however, function at significantly higher current values than required for many electric propulsion

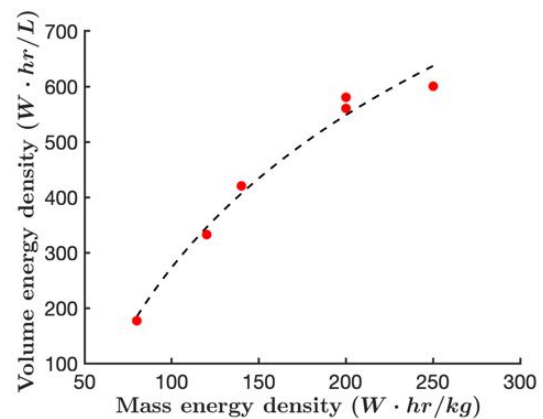


Figure 12.1 Trends for battery properties in existing technology



applications. Therefore, despite various avenues of anode materials, the team decided to stick with the commonly used graphite anode, which has a TRL of nine (commonly used in commercial applications), rather than on-going research with TRLs of five (prototyping and testing stages).

While the mass energy density was given in the RFP, the volume energy density had to be determined through examination of current technologies. Figure 12.1 shows the mass energy density and corresponding volume energy density of current batteries. With the curve fit of this data, for the given mass energy density of 400 W-hr/kg (7.83 HP-hr/slug), the volume energy density was determined to be 823.75 W-hr/L (4.18 HP-hr/gal). Additional battery parameters for the vehicle include a cell voltage of 4.0 V, charge and discharge rate of 1.0 C, life cycle of 2000 cycles and cost of \$400 per kW-hr (\$298.28 per HP-hr) with the cathode material, NMC, already detailed earlier. The battery mass required was found to be 349.95 kg (771.51 lb), which gives a total battery capacity on board 139.98 kW-hr (187.72 HP-hr). This battery mass is computed using the energy required for the mission (including reserve) and then accounting for an additional 10 % in energy required for avionics, flight controls and cabin systems such as lighting and air conditioning. It further accounts for an additional 5 % for potential vehicle power and energy losses.

The battery C-rate can now be calculated [143, 144] and is found to be 258.89 $A \cdot h$ or 3.40C. Similarly, the E-rate is 168.075 kW-hr. Given the cell voltage limit of 4.0 V, 175 cells are first to be connected in series creating a line, resulting in a maximum output 700 V. Multiple cell lines will then be connected in parallel to get a battery pack. Connecting the cell lines in parallel increases the capacity of the battery to the limit specified by the RFP. There are further phenomena to be considered, such as charge variation, voltage sag, and internal resistance, but the assumption of an idealised battery is used here (as per RFP) and so these effects are assumed as negligible.

12.2 Motor and Electronic Speed Controller Analysis

Balto features eight lifting rotors and two cruise propellers, each driven by at least one motor with an associated gear box. The power and torque requirements for each of the motors have been defined in Section 9. An extensive search was conducted to find a set of suitable motors for the prescribed mission, and the results are shown in Table 12.2. These motors were selected for analysis, as they have been already certified for aerial operations (TRL levels of 9) and have a proven safety record.

	MGM Compro		MagniX 650		EMRAX 348		EMRAX 268		EMRAX 208	
	SI	English	SI	English	SI	English	SI	English	SI	English
Maximum Power	80 kW	107 HP	640 kW	858 HP	380 kW	510HP	200 kW	268 HP	68 kW	91 HP
Maximum Torque	300 N-m	221 lb-ft	3020 N-m	2227lb-ft	1000 N-m	738 lb-ft	500 N-m	369lb-ft	140 N-m	103 lb-ft
Continuous Power	70kW	94 HP	560 kW	751 HP	210 kW	282 HP	107kW	143 HP	41 kW	55 HP
Continuous Torque	180 N-m	133 lb-ft	2820 N-m	2080 lb-ft	500 N-m	369 lb-ft	250 N-m	184lb-ft	80 N-m	59 lb-ft
Maximum Speed	12000 RPM	12000 RPM	2300 RPM	2300 RPM	4000 RPM	4000 RPM	4500 RPM	4500 RPM	6000 RPM	6000RPM
Voltage	400V	400V	500 V	500V	420V	420 V	250 V	250 V	120V	120V
Maximum Efficiency	95 %	95%	90%	90%	98%	98%	98%	98%	98%	98%
Maximum Mass	22.00kg	1.51slug	200.00kg	13.70slug	42.00kg	2.88 slug	20.00kg	1.37 slug	9.10kg	0.62slug

Table 12.2 Potential motors comparison and selection (Data collected from manufacturers and Ref. 145)

A Pugh analysis was performed for the surveyed motors. Torque, power, footprint, weight, efficiency, and type of cooling were all compared for each motor type. The team preferred an air-cooled system, as it is less complex and reduces the overall weight of the system. Further analysis honed in upon the the EMRAX 268 motor, which is completely air-cooled and features built-in motor stacking capabilities for enhanced power and torque outputs. Reduction in maintenance cost and enhanced ease of part sourcing during manufacturing is achieved by having the same motor for both the hover and forward flight propulsors.

Various electronic speed controllers (ESCs) were selected from the manufacturer's preferred product list to avoid incompatibility issues. The MGM Compro HBC 400, DANA TMC 200, and UniTEXK Bamo Car D3 were considered. The UniTEXK Bamo Car D3 was ultimately selected for the motor; this ESC can be brought in an air-cooled version, further reducing the complexity, and meets all power requirements from the motor. Additionally, EMRAX has suggested this controller as one of their preferred motor controllers.



12.3 Motor and ESC Placement

Placement of the motors and ESCs was carefully carried out in order to meet the design objectives of *Balto*. The four inner lifting rotors are variable RPM only, and have only one motor each; however, they will still have a gear box as shown in Figure 12.2 (a), for reasons detailed in Section 12.5. The four outer lifting rotors are both variable pitch and variable RPM controlled, and they are more critical than the inner variable RPM rotors, as they are required for moment control purposes. For redundancy and enhanced power and torque capabilities, the motors are stacked in pairs. The motors for the outer lifting rotors are placed side by side, as shown in Figure 12.2 (b), to reduce the profile of the supporting beam. The outer rotors already have higher control authority due to the variable pitch mechanism and longer moment arm (further from center of gravity). Hence, stacking these rotors will enhance the ability, through larger power and torque outputs, for a quick correction maneuver or in emergencies.

In the event of failure, the outer lifting rotors would have to take on additional load, thus it is important that power and torque capabilities can be increased during emergencies. The motor housing is the same for all lifting rotors, irrespective of whether they are stacked or not. The motors powering the two cruise propellers are also stacked for redundancy; see Figure 12.2 (c).

To maintain maximum motor efficiency at all times during flight, only one of the two motors in a stacked configuration will operate at any given time. The other motor is kept for redundancy purposes and activated only for emergency procedures.

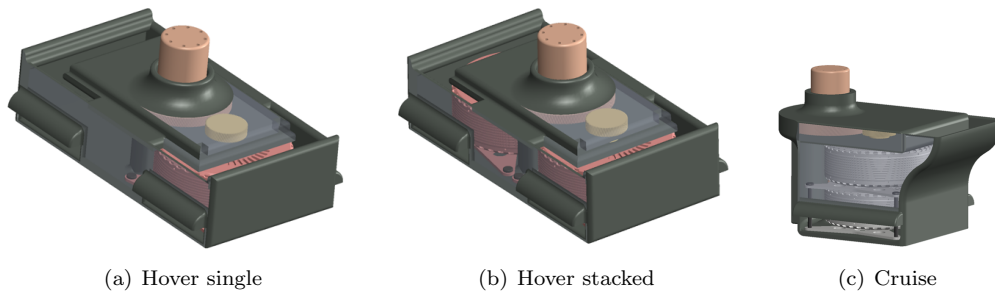


Figure 12.2 Hover and cruise motor gear boxes

Each motor has two ESCs. While this adds considerable mass, the redundancy eliminates the possibility of a single point of failure of the electrical power distribution system. It also reduces the chance of mechanical failure of the motor.

12.4 Wiring & Battery Placement

The following subsections detail the process to select the wiring material, as well as the methodology employed when designing the overall electric connections and cross-wiring for the vehicle.

12.4.1 Wiring Material

Electrical wiring is one of the heaviest components in modern day electrical aviation. As such, *Baltos* wiring was designed to minimize its weight.

The EMRAX 268 motors are able to operate in three different voltage configurations, low of 250 V, medium of 650 V and high of 800 V. Due to the limitations of the ESC equipment and the reduced motor performance at higher voltages, the medium voltage range was targeted for motor operation. Moreover, overall current being transferred into the system must be reduced in order to minimize wiring weight, hence the medium voltage range is better than lower. By Pouillet's and Ohm's Laws, minimizing the current and maximizing the voltage in the system permits *Balto* have a lightweight wiring construction, while also



decreasing losses during power transfer. The wire cross-sectional area was determined to be 95 mm^2 (0.1473 in^2), which is similar to the industrial wire size of AWG 0000 4/0.

Copper was selected as the wire material due to its low resistance, low weight, and high tensile strength. Moreover, from a manufacturing standpoint, copper is widely available and commonly used in various aviation applications. Copper wiring is available in two forms: stranded and solid. While stranded copper wires are more costly compared to their solid counterparts, they have increased resistance to vibrational loads and perform better at small wire lengths, making it more suitable for use in electromechanical assemblies, such as those here. H07RN-F rubber insulation will be applied to the stranded copper wire so that it can withstand voltage, temperature, and load requirements for the vehicle.

12.4.2 Wiring Diagrams and Battery Setup

Electronic Speed Controllers:

The wiring for a single and stacked motor with ESC redundancy is illustrated in Figure 12.4. Switches will be used to switch ESCs if necessary in the event an ESC or its wire connections fail.

Battery and Full Vehicle:

Figure 12.3 depicts the full vehicle wiring diagram from the top view and 12.5 is from the side. The only electrical components in *Balto* are in the cockpit, cabin lighting and systems, motors, control surfaces, doors and ramp.

The total battery mass is distributed across the vehicle in packs, both to ensure weight distribution, and to add redundancy balancing via cross-wiring which is done with the help of a power distribution board. Most of the battery weight is on the wings, because the lower portion of the fuselage beneath the cabin floor contains seats and cargo. Furthermore, keeping the battery closer to the motors reduces losses across cables. Two power distribution boards on the vehicle support the cross-wiring redundancy measure in the event of an electrical component failure. A power distribution board allows a single motor to be connected to multiple battery packs. Hence, in the event that there is an electrical failure (perhaps in a battery pack), the power distribution board allows the motor to draw power from other battery packs, ensuring a fully redundant system in the event of electrical component failure. Further, the power distribution boards help with rerouting the power to its intended motor. While the power distribution boards add 3.5 kg (7.71 lb) of additional weight and another potential point of failure, being another electrical component itself, the board itself is a redundancy measure, thus its failure would not be flight-critical.

12.5 Gear Box

Analysis performed in Section 9 identified that the torque requirements for the mission were higher than what the motors can provide at the design tip speed of 180.88 m/s (600 ft/s , 1430 RPM). The torque and power curve for the EMRAX 268 are given in Figure 12.6, where the motors would operate at an efficiency of 86%, increasing the battery weight. The best efficiency and torque output for the motor is achieved at a rotational speed of 3400 RPM ($1,425 \text{ ft/s}$), which would exceed the RFP specifications. Therefore, the addition of a gearbox is necessary to reduce the rotor rotational speed and to increase the torque output on the propeller shaft.

A gearbox of ratio 1:2.5 was designed to reduce the motor RPM from 3577 to 1431. This satisfies the RFP tip speed requirement, and surpasses the torque requirements with a continuous torque of $625 \text{ N}\cdot\text{m}$ ($460.98 \text{ lb}\cdot\text{ft}$). The gear box in Figure 12.2 is used in both lifting and cruise conditions. The lifting rotors, despite a side-by-side stacking configuration, only require one shaft since both motor gears are connected to the rotor gear. Furthermore, all gear box and motor housing designs allow for air to pass through freely enabling the motors to be air cooled in flight. This is done while ensuring that the gearbox remains closed to avoid any environmental influences affected gear performance.

Electrical motors' outer shells are disconnected from the internal magnetic coil, and gear shafts are



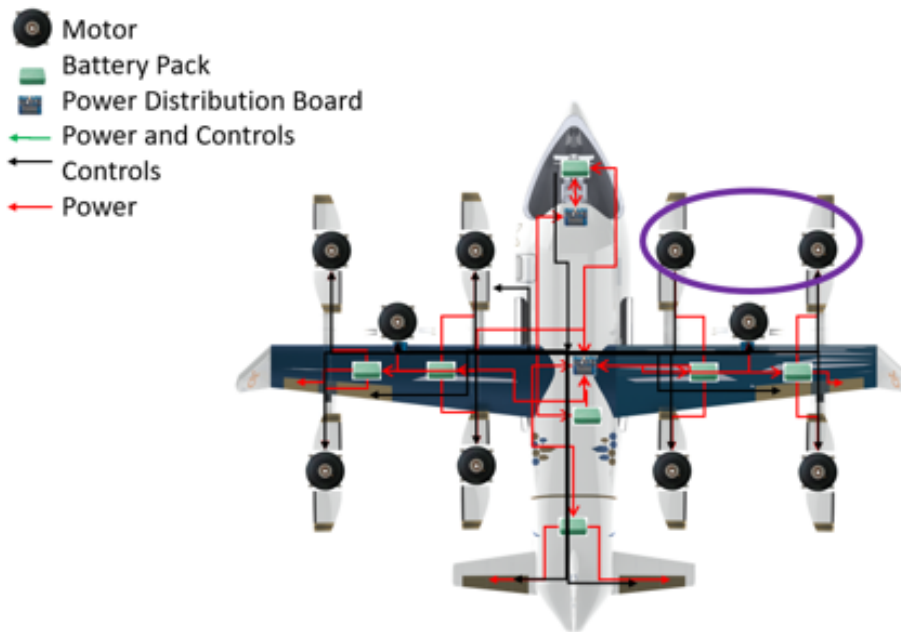


Figure 12.3 Full vehicle electrical wiring diagram, top view

connected to the outer shell. In the event of a motor loss, the gear shaft will not be hampered by the defective motor; the outer shell will spin freely. If a mechanical failure prevents the shell also from spinning, the given lifting rotor or cruise propeller will no longer be in use. This does not pose an issue since the vehicle is designed to fly with six lifting rotors and a single cruise propeller with rudder control as appropriate.

The gear box material was investigated, comparing copper, aluminum, and iron alloys, using information from Ref. 147. Copper gears are used for applications with large endurance requirements, while iron alloys are used when high material strength is needed. While these materials are attractive for this design, they both present considerable weight penalties. Aluminum gears are light, but do not have as high an endurance or material strength as copper or iron. An aluminum bronze alloy, also containing nickel and manganese, is used instead. The bronze ensures a higher material strength and endurance, while nickel and manganese reduce corrosion and environmental effects.

The team also explored the possibility of using thermoplastics, like acetal or nylon, for the gears. They are light and easy to manufacture, and they are self-lubricating, ensuring simplicity and improving maintenance costs. However, these materials are extremely brittle, and they are not yet ready for use in high-rotational-speed applications.

Five common gear types were considered for the gear box design, based on Refs. 148 and 149: spur, bevel, helical, worm and planetary. The team conducted an empirical study comparing manufacturing simplicity, design complexity, suitability for the vehicle purposes, noise, and efficiency on a scale of 1 to 5 (worst to best), and results are shown in Table 12.3. From this analysis, the gear type was chosen to be helical. Details of the gears are shown in Table 12.4.

All gearboxes have a backlash effect which needs to be considered [150, 151]. Backlash is the spacing between the gear teeth, or how much the output gear will move without the input moving [149, 152]. Optimum backlash spacing ensures that the grinding between gears is left to a minimum, increasing the gears' effective life span. While low backlash leads to gear binding and life span reduction, high backlash results in lower efficiencies and more probable gear damage. Using this information, the teeth design and backlash limit were designed following JIS B 1703-76 standard for helical gears an optimum gear spacing.

Lastly, the lubrication used in the gear box was investigated, using Ref. 153. *Balto's* gear boxes operate in high-speed, high-loading environments. Grease lubrication is therefore discarded, as it is used in low-speed



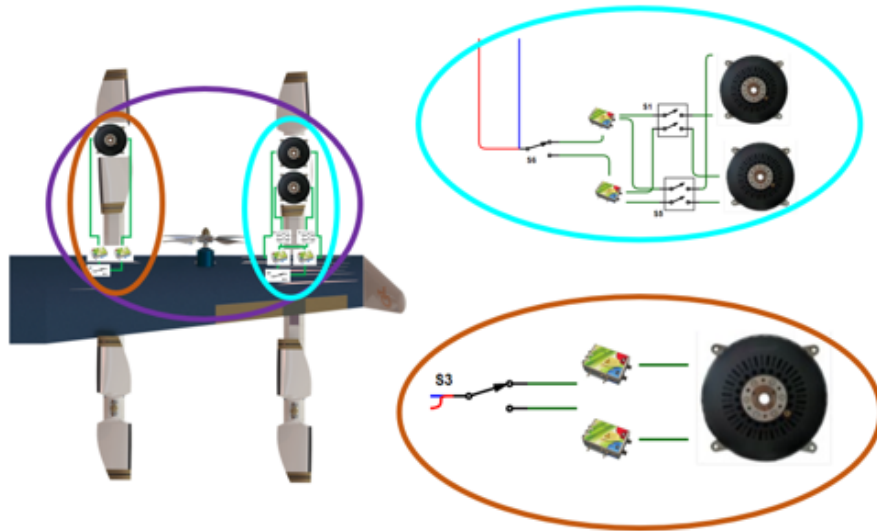


Figure 12.4 Full vehicle detailed electrical wiring diagram, top view, ESC wiring

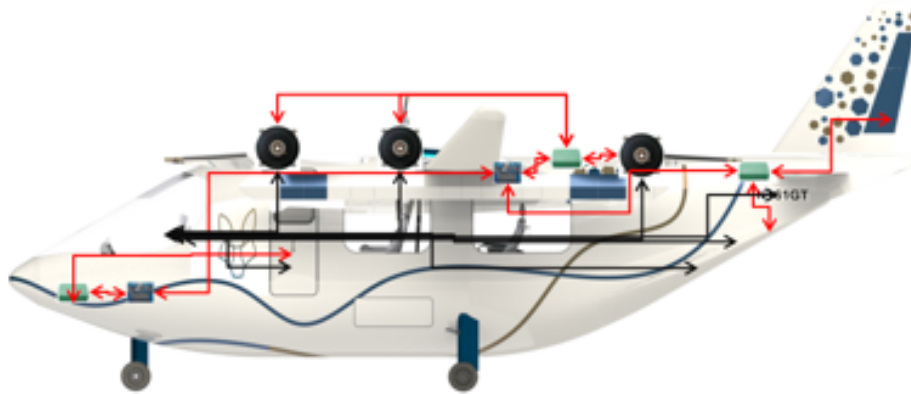


Figure 12.5 Full vehicle electrical wiring diagram side view

Parameter	Spur	Bevel	Helical	Worm	Planetary
Manufacturing	5	4	5	3	2
Complexity	5	4	5	4	3
Suitability	5	3	5	3	4
Noise	3	4	4	5	4
Efficiency	4	5	5	3	3
Total	22	20	24	18	16

Table 12.3 Potential gears comparison and selection

and low-loading applications. While forced oil lubrication performs better at high speeds, it is not very effective. The team decided to use oil splash lubrication, as it is effective in high speeds and high loading, and it is commonly used in helical gears. All factors were accounted for and the lubrication system was designed to specifications meeting the FAR 29.927(c)(1) standards for rotor drive systems [154, 155].



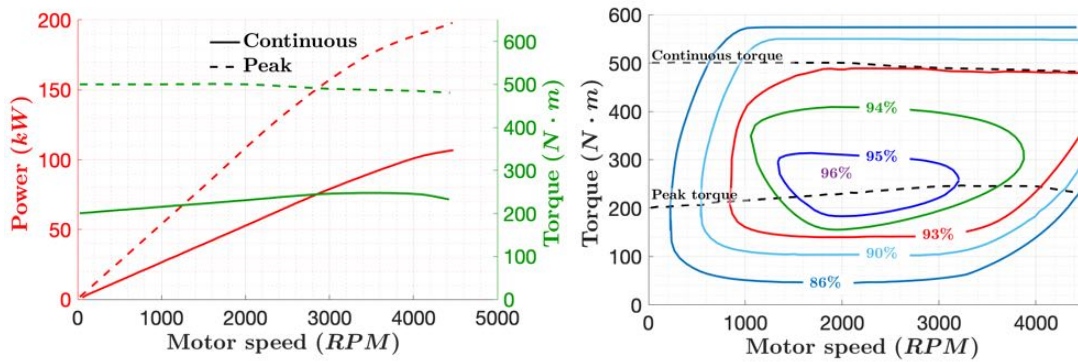


Figure 12.6 Performance plots for EMRAX 268 motor (adapted from Ref. 146)

	Pinion Input Driver Gear		Output Driven Gear	
	SI	English	SI	English
Type	Helical	Helical	Helical	Helical
Material	Aluminium Bronze Alloy	Aluminium Bronze Alloy	Aluminium Bronze Alloy	Aluminium Bronze Alloy
Teeth number	20	20	50	50
Face width	25 mm	0.9834 in	25 mm	0.9834 in
Diametral pitch	0.25 teeth/mm	6.35 teeth/in	0.25 teeth/mm	6.35 teeth/in
Pressure angle	20 deg	20 deg	20 deg	20 deg
Pitch diameter	80 mm	3.15 in	200 mm	7.87 in
Mass	2.27 kg	5.00 lb	4.21 kg	9.29 lb

Table 12.4 Potential gears comparison and selection

12.6 Powertrain Operational Considerations and Maintenance

Today's technology enables a 100 kWh battery to be charged in 20 minutes assuming a 240 kW [156,157]. Our total battery is a much larger (139.98 kWh), but extrapolating the same and account for any charging inefficiencies, the full battery will still be charged in less than 45 minutes. Therefore, the charging can be accomplished within the loading and unloading time, avoiding additional downtime of the vehicle. Charging ports are available on the wing locations to charge the battery packs directly; this will further save time since the whole battery pack is not being charged via a single port. Batteries maintain maximum efficiency when constantly charged from 20% to 80%, which will take 50% of the charging time. This efficiency is maintained to some degree on board the vehicle since the reserve battery is 21 % of total battery mass. Thus in an ideal flight scenario, the battery will never be completely drained and will require charging from 20 % to 100 %. This reducing charging time and increasing battery life span when compared to charging from 0 % to 100 %

With regards to safety, the biggest issues with Li-ion batteries is thermal runaway, which is not considered (as per RFP). Thus, the biggest concern is ensuring the battery does not come into contact with fluids. This will be achieved via watertight containers for the battery packs. The containers will be made of lightweight material and coated with common watertight substances such as polyurethane or thermoplastics. Furthermore, the power distribution boards will be equipped with pyrotechnic-squib-triggered fuses to prevent the failure of the entire electric system should the board fail.

Maintenance of the motors, speed controllers and batteries will be conducted on a regular basis between every flight to ensure no damages. This will include the inspection of control surfaces and any critical electrical points on board, such as power distribution boards. Additionally, there will be provisions on the wing (close to charging ports) to open up the wing surface should battery servicing or replacement be required. Sample locations of these hatches for servicing of the batteries, wires, lifting rotors, gearboxes and cruising propellers are shown in red in figure 12.7.



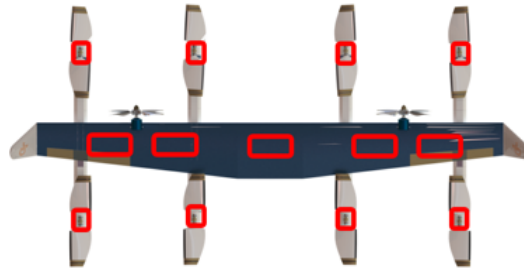


Figure 12.7 Potential maintenance hatches marked in red

The entire system is highly reliable, being electric with the numerous redundancies and additional safety measures already added on board. This does not come at the expense of efficiency, as every component is still operating at least at 95 % efficiency or above, indicating that the overall propulsion system is efficient and optimal for its designed purpose.

13 Weight Breakdown and CG Analysis

The vehicle component weights were tabulated and used to locate the center of gravity. Center of gravity calculation assumes all components are point masses.

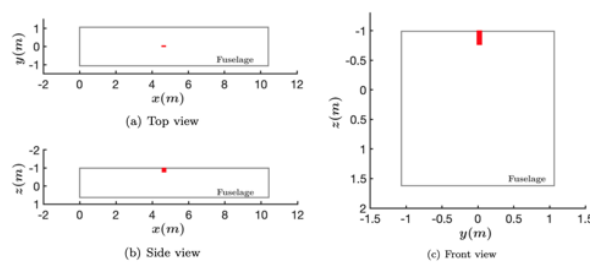


Figure 13.1 *Balto's* CG travel for different cabin arrangements (in red) with respect to the fuselage box (in grey)

The center of gravity of the vehicle is tabulated in Table 13.1 for the two limiting configurations: the PRM configuration with the pilot, no passengers, and no bags, and the full mobility configuration with the pilot, four passengers, and all bags. The locations are given in standard aircraft orientation, with north east being down and the origin at the vehicle nose. Figure 13.1 indicates the CG travel inside the fuselage - drawn as a box for illustration purposes - and how it moves with different cabin arrangements:

- Only the pilot and no bags
- A full non-PRM configuration
- A non-PRM configuration with only left seat occupied
- A full PRM configuration
- A PRM configuration with two wheelchairs, no caregivers
- A PRM configuration with one wheelchair and one caregiver, both in the front seats and the back seats



Configuration	Gross Mass		Center of Gravity					
	kg	lb	x		y		z	
			m	ft	m	ft	m	ft
Only pilot, no bags	2100.2	4620	-4.53	-14.86	-0.01	-0.02	-1.00	-3.39
Four passengers, all bags	2668.0	5870	-4.60	-15.10	0.02	0.06	-0.87	-2.86

Table 13.1 Location of *Balto's* center of gravity

Configuration	Mass Moments of Inertia											
	I_{xx}		I_{yy}		I_{zz}		I_{xy}		I_{xz}		I_{yz}	
Only pilot, no bags	3878.9	2860.9	2670.9	1970.0	5554.6	4096.9	0.873	0.644	2338.7	1725.0	-0.369	-0.272
Four passengers, all bags	4848.7	3576.19	3338.7	2462.5	6943.3	5121.1	1.0914	0.805	2923.4	2156.2	-0.461	-0.34

Table 13.2 *Balto's* moments of inertia

Figure 13.1 shows how the CG travel is considerably smaller than the fuselage. Minimal CG travel is due to the weight of the batteries being located in the wings, as discussed in Section 12. Similarly, *Balto's* mass moments of inertia are located in Table 13.2.

Balto's weight breakdown is provided in Table 13.3.



	Mass, kg	Mass, lb
<i>Balto</i>	<i>2491.9</i>	<i>5870</i>
AERODYNAMICS	229.80	506.64
Wing Skin	105.51	232.61
Horizontal Tail Skin	25.49	56.20
Vertical Tail Skin	12.74	28.09
Rotor Blades	76.48	168.61
Propeller Blades	9.58	21.13
STRUCTURES	733.04	1608.21
Wing	138.32	304.94
Rotor Boom	24.47	53.95
Horizontal Tail Boom	34.62	76.32
Vertical Tail Boom	17.28	38.10
Airframe	297.72	656.36
Fuselage Skin	61.59	132.28
Landing Gear	96.94	209.35
Ramp	62.10	136.91
BATTERY	349.96	771.51
Hover	16.21	35.74
Hover Climb	17.00	37.48
Cruise Climb	2.98	6.57
Cruise	176.37	388.84
Cruise Descent	7.15	15.77
Hover Descent	21.75	47.95
Mission	273.28	602.49
Reserve	76.67	169.02
PROPULSION	332.8	733.69
Motors	200.00	440.92
Electronic Speed Controllers	108.8	239.86
Gear Box	14.40	31.75
Variable Pitch Mechanism	9.60	21.16
ELECTRONICS	20	44.09
Power Distribution Boards	4.00	8.82
Wires	16.00	35.27
Avionics	0	0
CABIN	150.8	331
Seats	101	222
Seat belts, tie-downs, rails	8.4	18
PA system	1.8	4.0
AC/ventilation	3.6	7.9
Front compartments	15	33
Side compartments	15	33
Screen	6.0	13
COCKPIT	26	57
Seat	16	35
Screen & Switchboard	10	22
PAYLOAD	649.5	1432
Passengers	498.9	1100
Baggage	150.6	332

Table 13.3 *Balto* mass and cost

14 Flight Mechanics and Control

A simplified model of the vehicle's flight dynamics in hover is developed and will be used in Section 15 to demonstrate that the hover rotors provide enough control authority to satisfy hover maneuvering requirements. For cruise, longitudinal and lateral linearized models are derived. The empennage and control surfaces are sized. It is then proved that longitudinal and lateral handling qualities are satisfactory.

14.1 Hover Analytical Dynamic Model

The equations of motion of *Balto* during hover are derived as follows. The force equation is written as:

$$m\dot{\mathbf{V}}^e + m\boldsymbol{\omega}^b \times \mathbf{V}^e = m\mathbf{g} + \mathbf{F}^a + \sum_{i=1}^n \mathbf{T}^i \quad (5)$$

The moment equation is:

$$\sum_{i=1}^n \mathbf{s}^i \tau_E^i + \mathbf{I}^b \dot{\boldsymbol{\omega}}^b + \sum_{i=1}^n \boldsymbol{\omega}^b \times \mathbf{s}^i J^i \Omega^i + \boldsymbol{\omega}^b \times (\mathbf{I}^b \boldsymbol{\omega}^b) = \boldsymbol{\tau}^a + \sum_{i=1}^n \mathbf{r}^i \times \mathbf{T}^i \quad (6)$$

For each lifting rotor i , the equation of motion is:

$$J^i \dot{\Omega}^i = \tau_E^i - \tau_D^i \quad (7)$$

The equations are simplified to study the control power for vertical agility so that the aircraft is constrained to vertical translation only. The flat-plate model is used to estimate the vertical drag of the wing [158]; it is approximated as $D_{v_w} = \rho V^2 S$. Vertical drag due to the fuselage is $D_{v_f} = \frac{1}{2} \rho V^2 C_{D_{v,f}} S_f$, where $C_{D_{v,f}}$ is the fuselage vertical drag coefficient and S_f is the fuselage area from the top view. Since helicopter fuselage cross-sectional drag coefficients are averaged at around 0.5 without addition of sponsons or stub-wings [72], 0.5 can be used for $C_{D_{v,f}}$.

14.2 Cruise Analytical Dynamic Model

In cruise, *Balto* operates like a conventional fixed-wing aircraft since the eight lifting rotors are turned off. *Balto*'s control surfaces are the aileron, elevator, and rudder. The equation of motion in the state space form is linearized about the trim condition in cruise. Since the Mach number in cruise is below 1, it can be assumed that the Earth is flat and non-rotating. Further, it can also be assumed that there is no wind. The two propellers counter-rotate. For each propeller, the magnitude of the angular momentum at cruise condition is estimated to be 17.35 kg-m²/sec (411.7 lb-ft²/sec). Any gyroscopic moments due to propellers are neglected.

The linearized equation of motion expressed in the stability axes can be decoupled into longitudinal and lateral dynamics according to Refs. [159, 160]. The partial differential terms (such as X_u) in the system dynamics matrix are stability derivatives, while those in the control dynamics matrix (such as X_{δ_e}) are control derivatives. The estimation method for control and stability derivatives follows [159], [161]. In equilibrium, the states are $u_0 = V_{cruise}$, $v_0 = w_0 = 0$, $p_0 = q_0 = r_0 = 0$, $\phi_0 = \theta_0 = 0$. The aerodynamic and propulsive forces along the three axes are $X_0 = mg \sin \theta_0$, $Y_0 = 0$ and $Z_0 = -mg \cos \theta_0$ respectively. The moments due to aerodynamic and propulsive forces are $L = M = N = 0$. The longitudinal dynamics can be defined as:

$$\dot{x}_{lon} = A_{lon} x_{lon} + B_{lon} u_{lon}, \quad (8)$$

where

$$x_{lon} = \begin{bmatrix} \Delta u \\ \Delta w \\ \Delta q \\ \Delta \theta \end{bmatrix}, u_{lon} = \begin{bmatrix} \delta_e \\ \delta_T \end{bmatrix}, \quad (9)$$



$$A_{lon} = \begin{bmatrix} \frac{X_u}{m} & \frac{X_w}{m} & 0 & -g \cos \theta_0 \\ \frac{Z_u}{m-Z\dot{w}} & \frac{Z_w}{m-Z\dot{w}} & \frac{Z_q+mu_0}{m-Z\dot{w}} & \frac{-mg \sin \theta_0}{m-Z\dot{w}} \\ \frac{1}{I_y} \left[M_u + \frac{M\dot{w}Z_u}{(m-Z\dot{w})} \right] & \frac{1}{I_y} \left[M_w + \frac{M\dot{w}Z_w}{(m-Z\dot{w})} \right] & \frac{1}{I_y} \left[M_q + \frac{M\dot{w}(Z_q+mu_0)}{(m-Z\dot{w})} \right] & -\frac{M\dot{w}mg \sin \theta_0}{I_y(m-Z\dot{w})} \\ 0 & 0 & 1 & 0 \end{bmatrix}, \quad (10)$$

$$B_{lon} = \begin{bmatrix} \frac{X_{\delta_e}}{m} & \frac{X_{\delta_T}}{m} \\ \frac{Z_{\delta_e}}{m-Z\dot{w}} & \frac{Z_{\delta_T}}{m-Z\dot{w}} \\ \frac{1}{I_y} \left[M_{\delta_e} + \frac{M\dot{w}Z_{\delta_e}}{(m-Z\dot{w})} \right] & \frac{1}{I_y} \left[M_{\delta_T} + \frac{M\dot{w}Z_{\delta_T}}{(m-Z\dot{w})} \right] \\ 0 & 0 \end{bmatrix} \quad (11)$$

The lateral dynamics equation can be defined as:

$$\dot{x}_{lat} = A_{lat}x_{lat} + B_{lat}u_{lat}, \quad (12)$$

where

$$x_{lat} = \begin{bmatrix} \Delta v \\ \Delta p \\ \Delta r \\ \Delta \phi \end{bmatrix}, \quad u_{lat} = \begin{bmatrix} \delta_a \\ \delta_r \end{bmatrix}, \quad (13)$$

$$A_{lat} = \begin{bmatrix} \frac{Y_v}{m} & \frac{Y_p}{m} & \left(\frac{Y_r}{m} - u_o \right) & g \cos \theta_0 \\ \left(\frac{L_v}{I'_x} + I'_{zx}N_v \right) & \left(\frac{L_p}{I'_x} + I'_{zx}N_p \right) & \left(\frac{L_r}{I'_x} + I'_{zx}N_r \right) & 0 \\ \left(I'_{zx}L_v + \frac{N_v}{I'_z} \right) & \left(I'_{zx}L_p + \frac{N_p}{I'_z} \right) & \left(I'_{zx}L_r + \frac{N_r}{I'_z} \right) & 0 \\ 0 & 1 & \tan \theta_0 & 0 \end{bmatrix}, \quad (14)$$

$$B_{lat} = \begin{bmatrix} \frac{Y_{\delta_a}}{m} & \frac{Y_{\delta_r}}{m} \\ \left(\frac{L_{\delta_a}}{I'_x} + I'_{zx}N_{\delta_a} \right) & \left(\frac{L_{\delta_r}}{I'_x} + I'_{zx}N_{\delta_r} \right) \\ \left(I'_{zx}L_{\delta_a} + \frac{N_{\delta_a}}{I'_z} \right) & \left(I'_{zx}L_{\delta_r} + \frac{N_{\delta_r}}{I'_z} \right) \\ 0 & 0 \end{bmatrix}, \quad (15)$$

$$\dot{\psi} = r \sec \theta_o \quad (16)$$

$$I'_x = (I_x I_z - I_{zx}^2) / I_z \quad (17)$$

$$I'_z = (I_x I_z - I_{zx}^2) / I_x \quad (18)$$

$$I'_{zx} = I_{zx} / (I_x I_z - I_{zx}^2) \quad (19)$$

The dynamic models Eq. (8) and (12) are used to simulate the cruise dynamics and study the control power for attitude change in cruise.

14.3 Tail and Control Surface Sizing

14.3.1 Horizontal Tail Sizing and Longitudinal Stability

The horizontal tail is sized based on historical data of fixed-wing aircraft. The tail arm is around 50% to 55% of the fuselage length for an aircraft with wing-mounted engines. Whereas aircraft with aft-mounted engines, the tail arm is approximately 45% to 50% [162]. *Balto* has a fuselage length of 10 m (32.95 ft). In addition, *Balto* has electric engines for cruise propellers mounted at the leading edge of the wing and lifting rotors attached to the wing via booms. With 45% of the given fuselage length, the tail arm is 4.49 m (14.73 ft). There is not much room to increase the tail arm since the tail quarter chord location is already close to the end of the fuselage.

The horizontal tail volume ratio is used to size the area. In cruise, *Balto* operates at a Mach number smaller than 0.25. The low Mach number cruise mission gives a horizontal tail volume ratio at a lower end



Aircraft Type	V_H
Sailplane	0.50
Homebuilt	0.50
General aviation–single engine	0.70
General aviation–twin engine	0.80
Agricultural	0.50
Twin turboprop	0.90
Flying boat	0.7
Jet trainer	0.70
Jet fighter	0.40
Military cargo/bomber	1.00
Jet transport	1.00

Table 14.1 Horizontal tail volume ratio adapted from Ref. 162

Type	AR	λ
Fighter	3-4	0.2-0.4
Sailplane	6-10	0.3-0.5
Others	3-5	0.3-0.6

Table 14.2 Horizontal tail aspect ratio and taper ratio adapted from Ref. 162

of different types of aircraft based on Table 14.1. Additionally, the pitch stiffness due to the wing is already negative for *Balto*, which contributes to the dynamic stability. Thus, V_H could be smaller, as indicated by Eq. 20.

$$C_{M_\alpha} = C_{M_{\alpha,f}} + C_{L_{\alpha,w}} \frac{x_{cg} - x_{ac,w}}{\bar{c}} - \eta_H C_{L_{\alpha,H}} V_H \left(1 - \frac{d\epsilon}{d\alpha}\right) \quad (20)$$

A V_H of 0.5 yields a horizontal tail area of 2.58 m² (27.7 ft²). As a result, the static margin is 0.23 which is highly stable. A stable vehicle ensures comfort of the persons with reduced mobility during flight.

Table 14.2 was used as a guideline to determine the aspect and taper ratios of the horizontal tail. The taper and aspect ratio were chosen to be 0.5 and 5, respectively. A smaller aspect ratio would result in the tail root chord extending beyond the aft end of the fuselage. The leading-edge sweep of the horizontal tail was selected to be 5 deg more than the wing sweep as suggested by Ref. 162. The benefit to this selection is that the tail will stall later than the wing and at a higher critical Mach number than the wing. Since the leading-edge sweep of the wing is 0 deg, the leading-edge sweep of the tail is 5 deg. Wind-tunnel experiments and/or refined high-fidelity computations using CFD on high-performance computing are recommended to further refine the horizontal tail planform.

We verified that handling qualities conditions are met with these horizontal tail dimensions by studying the longitudinal mode characteristics. There are two sets of complex conjugate eigenvalues of the form $\lambda = n + / - i\omega$. The set with the smallest natural frequency corresponds to the phugoid mode and the other to the short period mode. For each eigenvalue, the following parameters are examined:

- The natural frequency $\omega_n = \sqrt{(n^2 + \omega^2)}$.
- The damping ratio $\zeta = -n/\omega_n$.
- The period $T = 2\pi/\omega_n$.
- The time to half or double $t_{1/2} = 0.693/|n|$

The following criteria must be met [161] to satisfy an acceptable level of handling qualities for all longitudinal modes:

- All longitudinal dynamic modes are stable
- Short period mode damping ratio between 0.35 and 1.30
- Phugoid damping ratio above 0.04 for level 1 (Good), above 0 for level 2 (Acceptable), or Phugoid period greater than 55s for level 3 (Poor)



- short period natural frequency vs. short period damping ratio in the acceptable range from Figure 14.1.

Longitudinal modes characteristics are determined from the matrix in Eq. 10. The resulting parameters for the selected horizontal tail are summarized in Table 14.3. All eigenvalues have negative real parts; therefore, the modes are stable. Short period mode damping is within the required range, and together with its frequency, it falls in the acceptable region as depicted by the red dot in Figure 14.1. Phugoid damping is between 0 and 0.04, satisfying the damping level 2 requirement outlined above. Therefore the longitudinal handling qualities of the vehicle are deemed acceptable.

eigenvalue	Mode type	Mode	ω_n ($rad.s^{-1}$)	ζ	Period(s)	$t_{1/2}$ (s)
-0.0140 +/- 0.4521i	oscillatory	phugoid	0.45	0.031	13.89	49.5
-1.7300 +/- 3.7477i	oscillatory	short period	4.13	0.42	1.52	0.41

Table 14.3 Longitudinal modes results for the selected horizontal tail

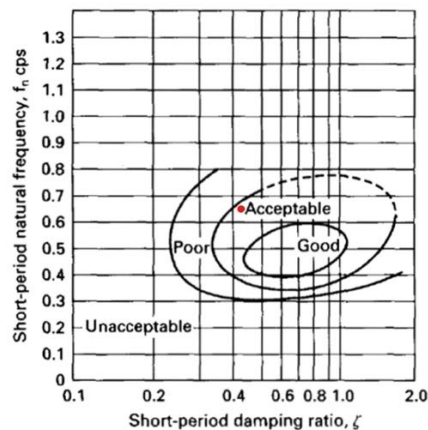


Figure 14.1 Short period mode flying qualities, red dot identifies *Balto's* results

14.3.2 Vertical tail Sizing and lateral stability

The vertical tail is sized by examining the lateral dynamic mode stability. For the lateral dynamic modes, there are two real eigenvalues of the form $\lambda = n$, and one set of complex conjugate eigenvalues of the form $\lambda = n + j\omega$. The real eigenvalue with the shortest time to half or double corresponds to the Rolling mode, the other real eigenvalue corresponds to the Spiral mode, and the set of complex eigenvalues corresponds to the Dutch Roll mode. For each eigenvalue, the following parameters are surveyed:

- For the complex eigenvalue, natural frequency $\omega_n = \sqrt{(n^2 + \omega^2)}$.
- For the complex eigenvalue, the damping ratio of $\zeta = -n/\omega_n$.
- For the complex eigenvalue, the period is $T=2\pi/\omega_n$.
- The time to half or double is $t_{1/2} = 0.693/|n|$

The following criteria must be met to satisfy level 1 handling qualities for all lateral modes [161]:

- All lateral dynamic modes are stable
- Spiral mode minimum time to double amplitude: 20 seconds



- Roll mode maximum time constant: 1.0
- Dutch roll mode minimum damping ratio: 0.19
- Dutch roll mode minimum natural frequency: 1.0
- Dutch roll mode minimum damping ratio and natural frequency product: 0.35

Lateral modes characteristics are determined from the matrix in Equation 14 for vertical tail surface S_v , ranging from 1 m^2 (10.8 ft^2) to 4 m^2 (43 ft^2). These limits have been set using conventional aircraft vertical tail volume historical data from [163]. The vertical tail volume is defined as $V_V = \frac{S_v l_v}{S b}$, where S_v is the vertical tail surface, l_v is the distance from the CG to the aerodynamic center of the vertical tail, S is the wing area, and b is the wingspan. The minimal value for V_V is 0.03, and the maximal value is 0.09.

Figure 14.2 provides lateral mode characteristics. The maximum vertical tail size to satisfy the spiral mode handling quality requirement is 1.5 m^2 (16 ft^2) with a span of 2 m (6.6 ft). This value is taken as the initial vertical tail size to allow the broadest possible area for rudder control surface and was validated when it satisfied rudder sizing requirements in Section 14.3.3.

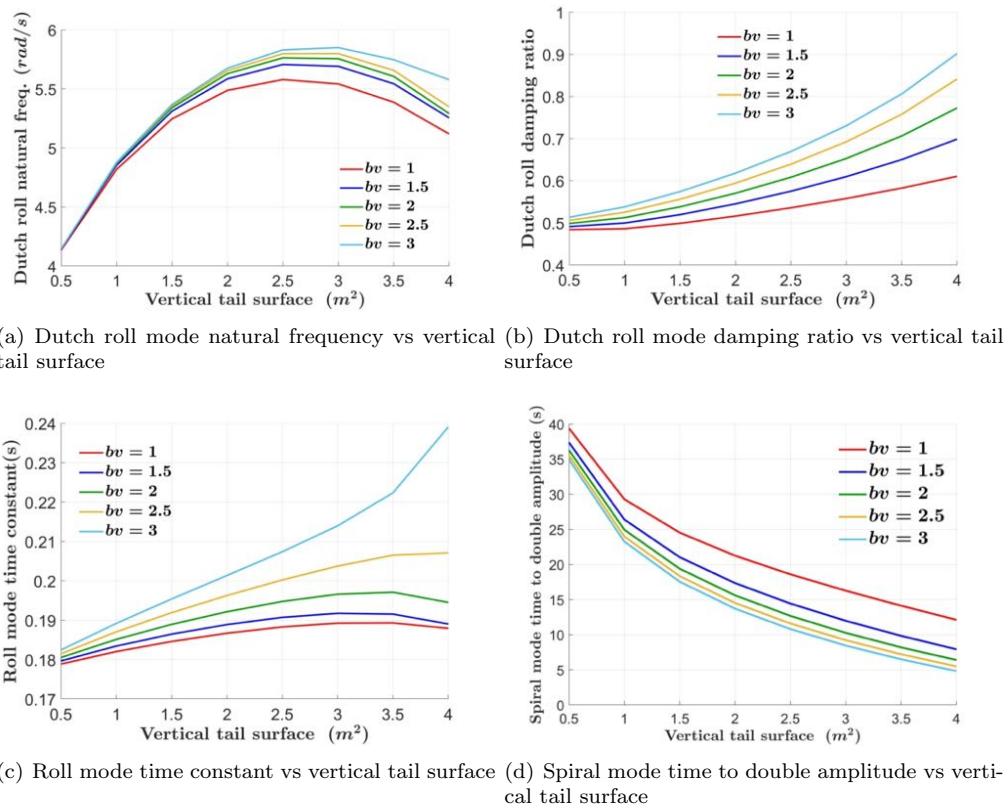


Figure 14.2 Lateral mode characteristics depending on vertical tail surface S_v and span b_v

Lateral modes parameters for the selected vertical tail are summarized in Table 14.4. All eigenvalues have negative real parts; therefore, the modes are stable.

14.3.3 Control Surfaces

Aileron: The ailerons are sized based on historical guidelines and the roll attitude change requirement from RFP. The ailerons span around 50% to approximately 90% of the wingspan. Chordwise, the ailerons are



eigenvalue	Mode type	Mode	ω_n ($rad.s^{-1}$)	ζ	Period(s)	$t_{1/2}$ (s)
-0.034	non-oscillatory	spiral	-	-	-	20.3824
-5.3002	non-oscillatory	rolling	-	-	-	0.1307
-2.8638+/-4.5063i	oscillatory	dutch roll	5.3393	0.5364	1.1768	0.2420

Table 14.4 Lateral modes results for the selected vertical tail

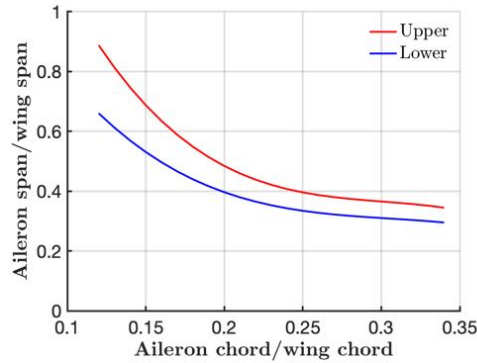


Figure 14.3 Historical guidelines of aileron sizing recreated from Ref. 162

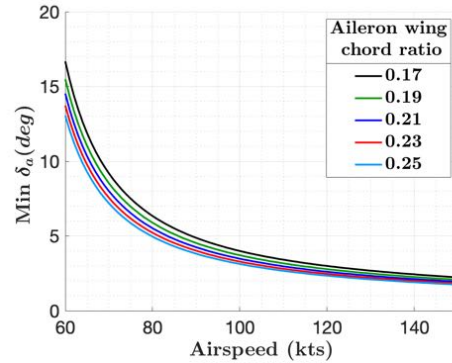


Figure 14.4 Minimum aileron deflections for roll attitude change with respect to forward speed

tapered by the same ratio as the wing so that the spars are straight-tapered due to a constant percent chord of the control surfaces [162]. Thus, the ailerons are designed to start from 60% to 90% of the wingspan. As shown in Figure, the aileron-wing chord ratio is guided by historical data 14.3. Also, the aileron chord is usually around 15% to 25% of the wing chord [162]. The effect of the aileron-wing chord ratio is studied under the roll agility requirement, which requires the aircraft to have sufficient control power to roll 10 deg from trim within 1.5 sec in a cruise condition. As shown in figure, 14.4 the minimum aileron deflection to achieve the roll agility requirement is smaller given a cruise speed with a larger aileron chord. At lower cruise speed, the differences in minimum aileron deflection are more significant among various aileron chords. As a result, the chosen aileron chord was 25% of the wing chord.

Elevator: Elevator sizing is also based on historical guidelines and the RFP-designated pitch agility requirement. Given that the static margin is larger than 0.15 - implying high stability [160] - a relatively large control surface is needed for pitching. From Table 14.5, elevators are around 25% to 50% of the tail chord [162]. The elevator chord was chosen at the higher end of the range and was designed to be 45% of the tail chord. Since the elevator area regulates the elevator control power, the effect of various elevator areas on achieving the pitch agility requirement is studied. The requirement states that the aircraft should have control power to make a 10 deg pitch change from trim in cruise within 1.5 sec. The minimum elevator deflection to achieve the requirement is plotted against a range of elevator areas. From Figure 14.6, as the elevator area increases, the minimum elevator deflection required to satisfy the minimum pitch agility decreases. However, a larger elevator area needs a more powerful electric motor, which could increase weight and cost. Thus, elevator area is chosen to be $0.927 m^2$ ($9.98 ft^2$). The time required to achieve minimum pitch agility for the selected elevator area with various deflections is shown in Figure 14.7. [162]

Aircraft	C_e/C
Sailplane	0.43
GA single engine	0.45
GA twin engine	0.36
Jet trainer	0.35
Fighter/attack	0.30*
Jet transport	0.25**

*Supersonic usually all-moving tail without separate elevator

**Often all-moving plus elevator

Figure 14.5 Elevator-wing chord ratio adapted from Ref. 162



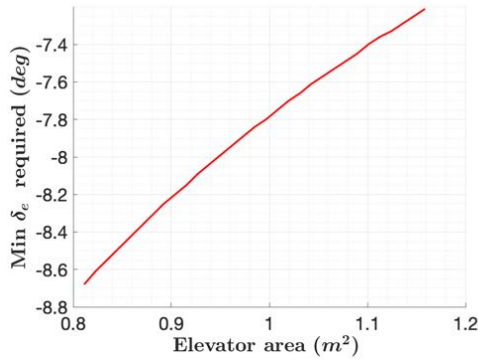


Figure 14.6 Effect of elevator areas on achieving pitch agility

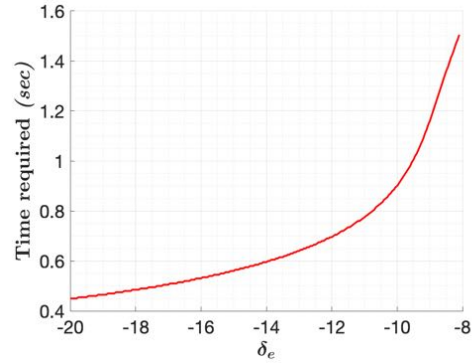


Figure 14.7 Time for 10 deg pitch change for the selected elevator area

Rudder: The rudder must satisfy the following requirements:

- There shall be sufficient rudder authority to defeat the yawing moment generated by asymmetric thrust due to engines failing at low speed.
- There shall be sufficient control power to achieve attitude changes from trim of 6 deg heading within 1.5 seconds at 1220 m (4000 ft), ISA +20 °C.

From historical data [164], it was assumed that the ratio of rudder span to vertical tail span is 0.7, and the ratio of rudder chord to vertical tail chord is 0.5. With the previously sized vertical tail, the rudder span is 1.4 meters (4.6 feet), and the rudder chord is 0.375 meters (1.2 feet). The maximum rudder deflection is +/- 30 degrees.

From Ref. 164, to trim a twin-propeller aircraft in case of engine failure, the required rudder deflection is calculated from Equation 21.

$$\delta_r = \frac{T_L y_T}{-q S b C_{n_{\delta_r}}} \quad (21)$$

where T_L is the operative engine thrust, y_T is the distance from the operating engine to the fuselage centerline along the body y-axis, q is the dynamic pressure, S is the wing area, b is the wingspan, and $C_{n_{\delta_r}}$ is obtained from Equations 22, 23.

$$\tau_r = 1.129 * \left(\frac{c_r}{c_V}\right)^{0.4044} - 0.1772 \quad (22)$$

$$C_{n_{\delta_r}} = -a_V * V_V * \eta_V * \tau_r * b_r / b_V \quad (23)$$

where c_r is the rudder chord, c_V is the vertical tail chord, b_r is the rudder span, b_V is the vertical tail span, a_V is the vertical tail lift curve slope, V_V is the vertical tail volume, η_V is the vertical tail dynamic pressure ratio. From Equations 21-23, Figure 14.8 depicts the required rudder deflection for speeds ranging from 26 m-s⁻¹ (85 ft-s⁻¹) to 77 m-s⁻¹ (253 m-s⁻¹) and for vertical tail surfaces from 1.5 to 3 square meters (16 to 32 square feet). For the chosen vertical surface of 1.5 square meters (16 square feet), the maximum rudder deflection of +/-30 degrees is sufficient to counter the moment generated by the loss of one engine in cruise. It is also the minimum acceptable area needed to handle engine out at 26 m-s⁻¹ (85 ft-s⁻¹). Therefore, the initial vertical tail sizing from Section 14.3.2 with the rudder dimension ratios chosen is satisfactory.

Equation 12 is discretized to simulate the response to rudder deflection.

$$x_{lat}(t + dt) = \dot{x}_{lat}(t) \times dt + x_{lat}(t) = (A_{lat}x_{lat}(t) + B_{lat}u_{lat})(t) \times dt + x_{lat}(t) \quad (24)$$

with $u_{lat} = [0 \ \delta_r]^T$ and where δ_r is the rudder deflection. The time required to perform a +/- 6-degree heading shift was determined at 121.9 m (4000 ft) and ISA + 20C at cruise speed for rudder deflection angles ranging from -5 to -30 degrees. Figure shows 14.9 that a rudder deflection magnitude of 10 degrees is



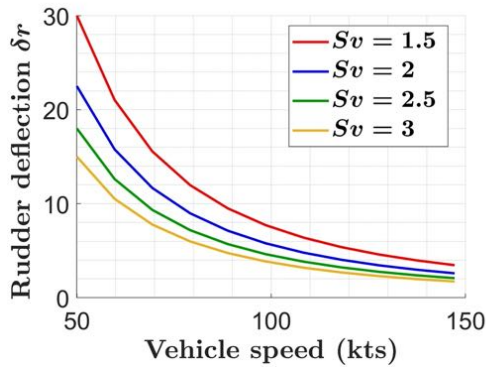


Figure 14.8 Rudder deflection required to counter engine loss depending on cruise speed and vertical tail surface

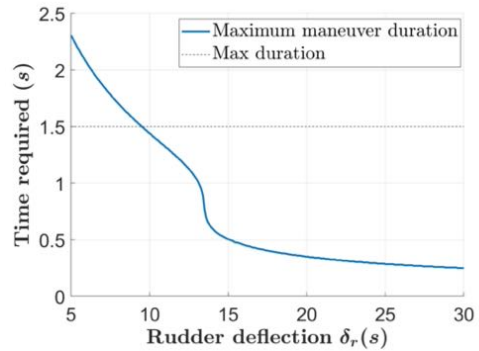


Figure 14.9 Time required to achieve +/- 6 degree change of heading for different amplitudes of rudder deflections

sufficient to shift the heading by 6 degrees in less than 1.5 seconds. Therefore both rudder requirements are satisfied with the current vertical tail and rudder.

15 Vehicle Performance & Maneuvers

In designing *Balto*, a multi-rotor compound eVTOL, excellent performance in both the lifting and cruise stages of the mission is sought after. Thus, the vehicle must find a good point of compromise to have both high disk loading and power loading for its rotors. The mission also requires *Balto* to travel in hot and high conditions [5], which are demanding; the lower air density and higher ambient temperatures effect the aircraft performance negatively in forms of reduction in lift generation and climb rate. Such conditions and design objectives presented a challenge for the team. Analysis of the performance of the vehicle throughout all stages of the mission will be discussed in the following subsections.

15.1 Power Required Curve

The configuration of *Balto* is atypical compared to standard fixed-wing aircraft and rotary wing vehicles. 15.6 displays the power required curve for *Balto*, with the lifting available and cruise available power delineated by back and blue horizontal lines, respectively. It can be seen that, in hover and low-speed flight, the power curve exhibits similar behavior to that of a conventional rotorcraft. As the aircraft gains speed and the wing becomes the primary lift generation mechanism, the power curve behaves similarly to that of a fixed-wing aircraft. As such, the power required in higher forward flight velocities is much smaller than a rotorcraft, it can be concluded that *Balto* enjoys the benefits from both types of aircraft.



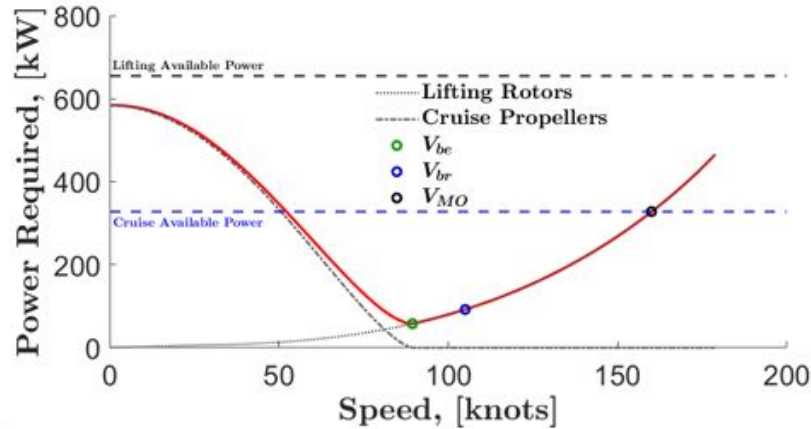


Figure 15.1 Power required curve with lifting rotor and cruise propeller available power

Due to the unique configuration of *Balto*, the calculation for best endurance speed (V_{be}) and best range speed (V_{br}) was unconventional. The graphical approach, outlined by Anderson [79], resulted in a large range of values for V_{be} and V_{br} . A more analytical method was employed for a more accurate result. The best endurance speed was found to be 46 m/s (151 ft/s) and the best range speed was 54 m/s (177 ft/s).

15.2 Hover Ceiling

Figure 15.2 shows the maximum operating altitudes with respect to the range of gross weights. At the lowest gross take-off weight configuration of 2100 kg (4629.71 lb), the ceiling is approximately 5000 m (16,404 ft). The trend is very linear with the aircraft weight and the HOGE ceiling reduces to 1000 m (3280 ft). However, the motors double-stacked for redundancy can also be used in emergency to greatly increase the ceiling height to approximately 7000 m (22965 ft).

From Figure 15.3, the required power for hover out-of-ground effect can be seen as a function of the flight altitude. The trend for all three configuration is identical. The increase in required power is relatively linear with the altitude until 5000 m (16404 ft), after which there is a rapid increase in the required power with respect to the altitude. The intersection between the the power required curve and the available power level were used to identify the HOGE ceiling at the three main aircraft configurations.

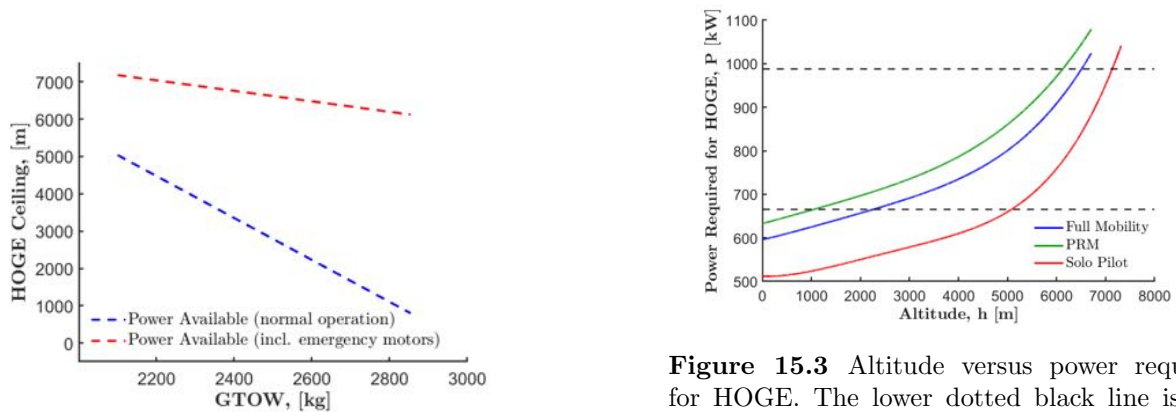


Figure 15.2 HOGE ceiling versus GTOW

Figure 15.3 Altitude versus power required for HOGE. The lower dotted black line is the power available during normal operation conditions. The higher dotted black line is the power available when all motors are utilized.



15.3 Service Ceiling

The service ceiling is defined as the altitude at which the maximum continuous power available results in a climb rate of 30.48 m/min (100 ft/min) at the forward speed for minimum power in compliance with the RFP [5]. Figure 15.4 shows the values for *Balto*. It is found that the lowest service ceiling occurs for the PRM configuration at the density altitude of 10,820 m (34,600 ft) and the highest ceiling occurs for the solo pilot configuration at 14020 m (44,864 ft).

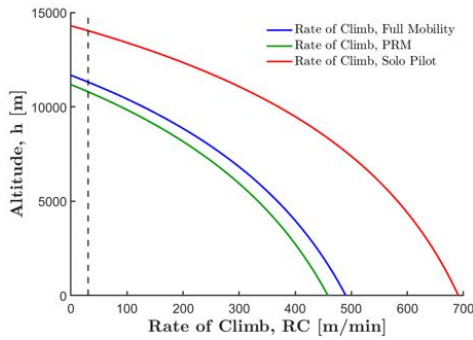


Figure 15.4 Service ceiling

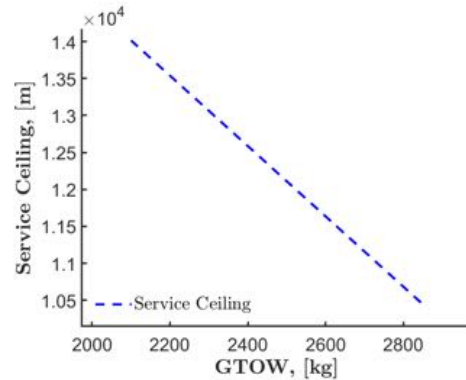


Figure 15.5 Service ceiling vs. GTOW

Examination of Figure 15.5 shows a linearly decreasing relationship between the service ceiling and the GTOW. The service ceiling is at a maximum value of 14,000 m (45,932 ft) when GTOW is at a minimum of 2,000 kg (4,409 lb). As the GTOW increases to 2,800 kg (6,173 lb), the service ceiling is reduced to 10,500 m (34,449 ft).

15.4 Maneuvers

The inboard lifting rotors (delineated in red) vary in RPM; the outboard lifting rotors (blue) vary in both pitch and RPM. Figure 15.6 plots rate of climb against variable collective and RPM. Maximum climb speed (3.5 m/s (12 ft/s)) of the lifting rotors, regardless of variable RPM or collective pitch, exceeds the RFP-prescribed RPM of 0.8 m/s (2.6 ft/s).

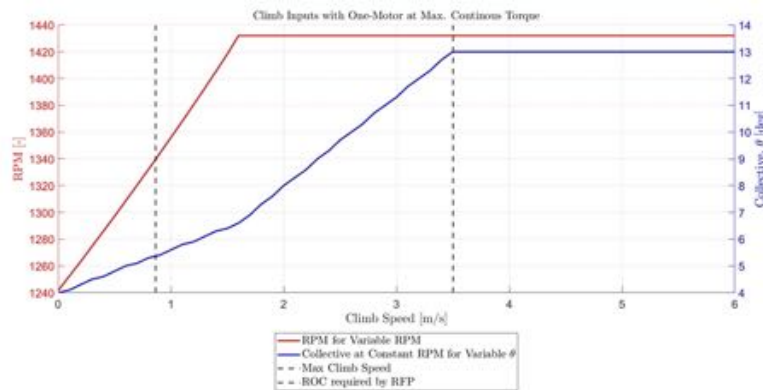


Figure 15.6 Power required curve with lifting rotor and cruise propeller available power



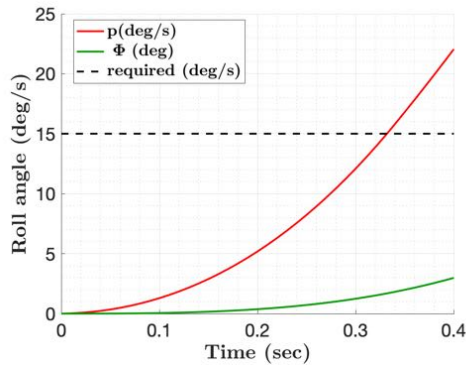


Figure 15.7 Variation of roll angle and roll rate with time for a roll maneuver in hover with wind

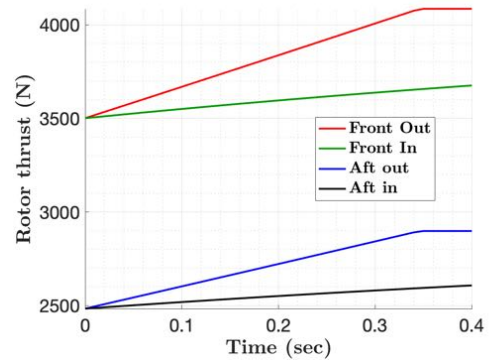


Figure 15.8 Variation of rotor thrust with time for a roll maneuver in hover with wind

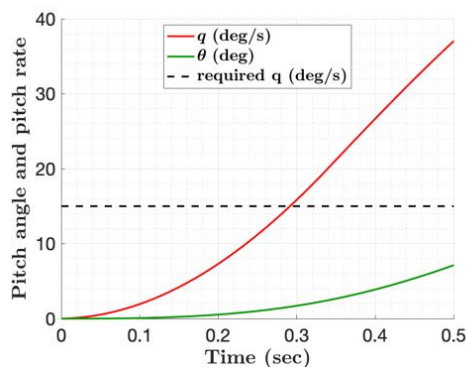


Figure 15.9 Variation of pitch angle and pitch rate with time for a pull-up in hover with headwind

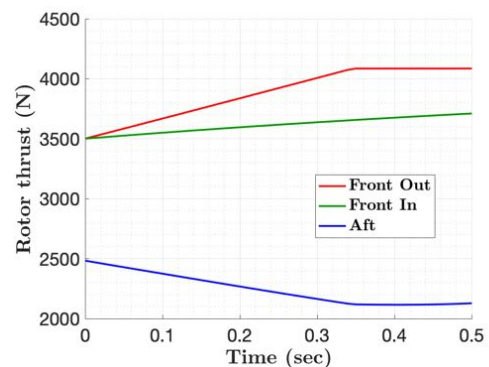


Figure 15.10 Variation of rotor thrust with time for a pull-up in hover with headwind

15.5 Results for Minimum Measures of Agility

15.5.1 Angular Rate Control in OGE Hover

In order to demonstrate that hover control power is sufficient to generate angular rate responses within 1.5 seconds of at least 15 deg/sec in pitch, roll, and yaw with a wind of 31.48 km/hr (17 knots) simulations have been ran. For rotations on all three axes, the required time is well below the 1.5 seconds maximum limit.

Roll:

Figures 15.7 and 15.8 present the response to a roll maneuver and the required thrust control in hover with wind.

Pitch:

Figures 15.9 and 15.10 present the response to a pull up maneuver and the required thrust control in hover with wind.

15.5.2 Vertical Agility in OGE Hover

To demonstrate whether the vertical agility requirement is satisfied, two simulations of vertical acceleration in the OGE hover condition are performed. The first simulation limited the max continuous torque and



the maximum continuous power of the lifting rotors. In the second simulation, the lifting rotors are limited by the maximum continuous power and the peak torque, but were allowed to exceed maximum continuous torque. As shown in Figure 15.11(a), *Balto* is able to accelerate vertically from $1g$ to more than $1.25g$ within 1.5 seconds whether the lifting rotors are limited by the maximum continuous torque or not. With the maximum continuous power constraint only, it takes *Balto* 0.85 seconds to vertically accelerate from $1g$ to $1.25g$. The variable-pitch lifting rotors change the pitch angle from 4.05 deg (0.0706 rad) to 7.08 deg (0.1235 rad) with a constant rate of 5 deg/s and maintain the pitch angle at 7.08 degrees . The discontinuity of the acceleration curve in Figure 15.11 (a) results from the variable-pitch lifting rotor reaching maximum continuous power limit. The thrust generated by each lifting rotor during vertical acceleration is shown in Figure 15.11 (b).

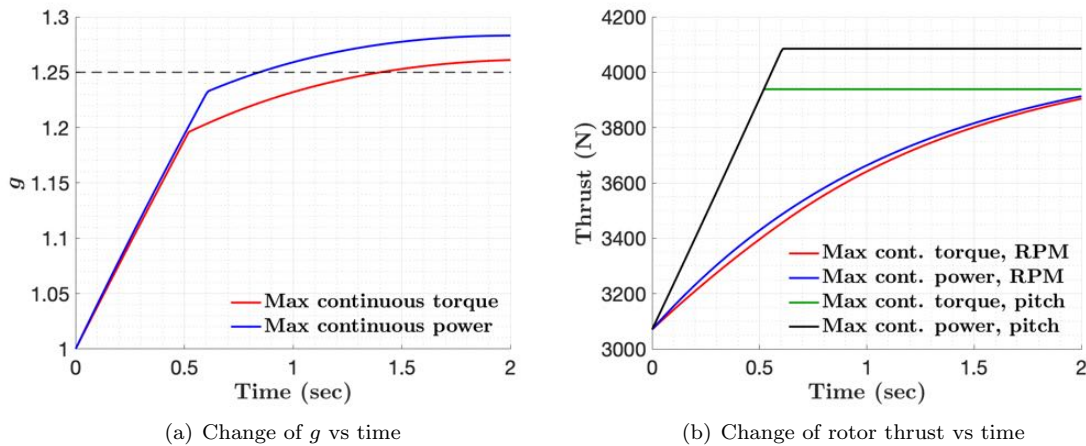


Figure 15.11 Change of g values and rotor thrust values in the vertical acceleration

15.5.3 Attitude change in cruise

Roll: With minimum aileron deflection of 5.9 deg , *Balto* is able to achieve 10 deg roll from trim in cruise condition within 1.5 sec. The trajectories of some lateral states from trim with 5.9 deg aileron deflection are shown in 15.12(a).

Pitch:

With minimum elevator deflection of 8 deg , *Balto* is able to achieve 10 deg pitch change from trim in cruise condition within 1.5 sec. The trajectories of change of pitch angle and pitch rate from trim with -8 deg elevator deflection are shown in Figure 15.13.

Yaw:

From the discretized model developed in Section 14.3.3, with minimum rudder deflection angled of 10 deg of magnitude, *Balto* is able to achieve 6 deg heading change from trim in cruise condition within 1.5 s as presented in Figure 14.9. Figure 15.14 shows the yaw angle and yaw rate variation for a -15-degree rudder deflection.

15.6 Limiting Maneuvering Load Factor

Since the lift mainly comes from the wing of *Balto* in cruise with lifting rotors idle, the limiting maneuvering load factors are defined in accordance with 14 CFR 25, paragraph §25.337. The limiting maneuvering load factors due to pitch change of 10 deg from trim in cruise within 1.5 sec at 1219.2 m (4000 ft ISA +20



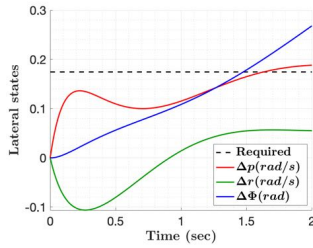


Figure 15.12 Lateral state trajectories in rolling

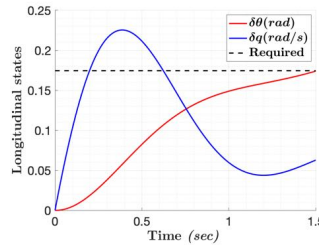


Figure 15.13 Pitch angle and yaw rate variation with time for a -15-degree rudder deflection

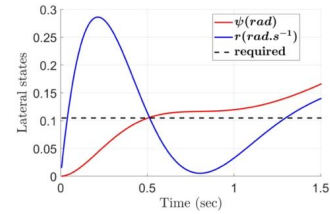


Figure 15.14 Yaw angle and yaw rate variation with time for a -15-degree rudder deflection

deg C, is obtained as follows. From the longitudinal dynamic equations 8, the change in aerodynamic forces along aircraft body-z direction (downward relative to the aircraft) is $\Delta Z = Z_u \Delta u + Z_w \Delta w + Z_q \Delta q + Z_{\dot{w}} \dot{w}$. Then, the limiting maneuvering load factor for pitch maneuver is $n = \frac{-(\Delta Z + Z_0)}{W}$. The negative sign results from the definition of body z-axis.

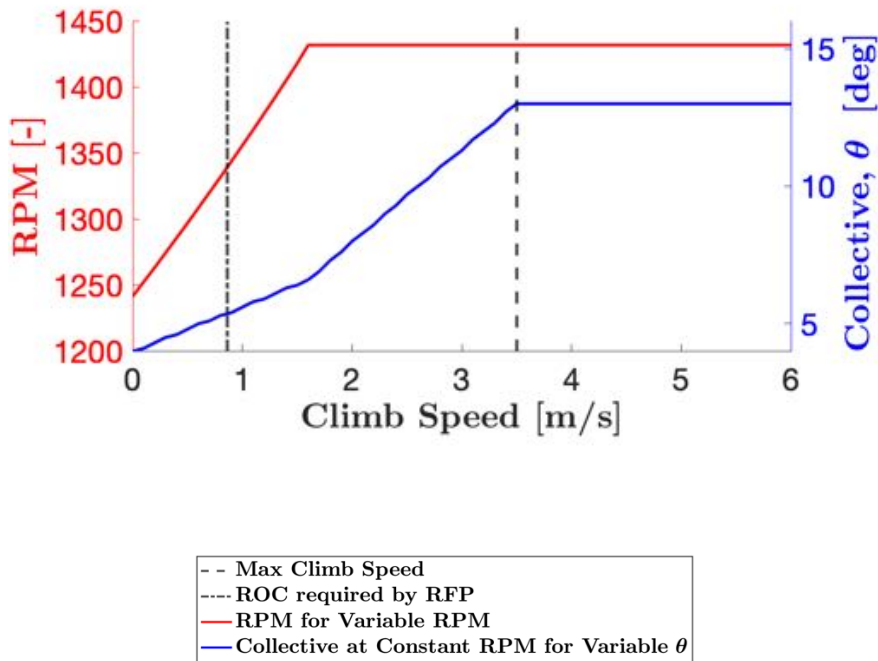


Figure 15.15 Climb inputs with one motor at max. continuous torque

16 Acoustics

While reducing the noise levels in the cabin is of interest for any passenger transport vehicle, it is especially critical that a vehicle designed to transport individuals with disabilities comfortably has low acoustic transmissibility. This requirement is especially true for individuals with hidden disabilities, like hearing impairment, ASD, and low vision, since noise exposure can irritate these conditions and make it



more challenging to access accommodations. In the case of low vision or blindness, individuals may be reliant upon hearing verbal instructions or queues. 3.1.1 The noise footprint should be no greater than 70dB, about as loud as a dishwasher or shower to mitigate the discomfort of the passengers, and based on the design objectives presented in section [165].

The sound footprint of the chosen design was evaluated using FlightStream’s acoustics toolbox [166]. The sound pressure level (SPL)

$$SPL(dB) = 20 \log_{10} \frac{p_{rms}}{p_{ref}}, \quad (25)$$

where p_{rms} (Pa) is the effective acoustic pressure amplitude and p_{ref} is the reference acoustic pressure, is calculated using the acoustic pressure recorded at desired noise observing points in the unsteady solver. $P_{ref} = 2 \times 10^{-5}$ is ostensibly the audible limit of the human ear [167].

The SPL of the eight rotors in hovering conditions 16.2 is evaluated at 12 stationary microphones evenly distributed around a circle with a 5 m (16.4 ft) radius, and the origin is at the intersection between the x- and y-plane 16.1. The eight rotors are divided symmetrically in the four quarters of the x-y plane. The microphones’ plane is offset by 5, 10, and 20 m (16.4, 32.8, & 65.6 ft) from the rotors’ plane.

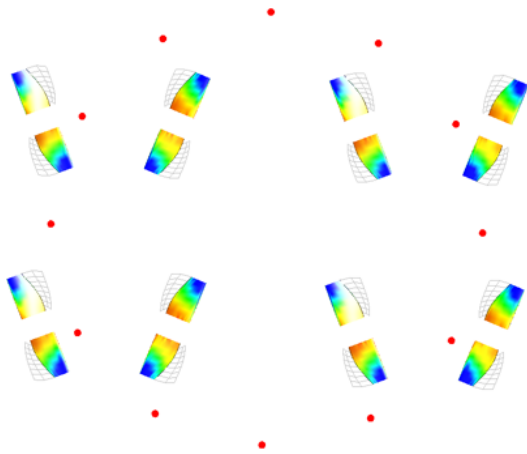


Figure 16.1 Hover acoustics test setup (top view). Microphones are represented with red spheres

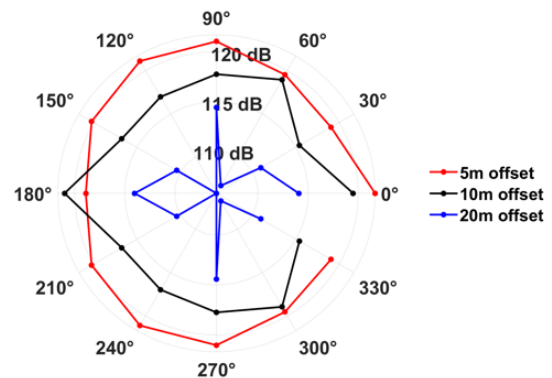


Figure 16.2 Sound pressure level at various vertical heights below the rotors

The computed SPL at a 5 m (16.4 ft) vertical distance from the rotors 16.2 is as loud as a chainsaw or leaf blower. Therefore, the cabin will contain acoustic padding in selected zones to reduce acoustic transmission. Zones are assigned based on lifting rotors’ proximity to the fuselage and the effect of the noise itself. In addition, the aircraft is designed so that the operative parameters are not conducive to noise. While there is no direct correlation between tip speed (proportional) and number of blades (inversely proportional) regarding noise levels, there is, however, some relationship [77]. With that in mind, the vehicle spends the vast majority of its time in cruise, where there are only two cruise propellers, with more blades than the lifting rotors and lower tip speeds. The higher number of rotor blades and the smaller tip speed will effectively lead to a positive impact on the noise levels. Furthermore, the lifting rotors are only two-bladed, which have low blade vortex interactional effects, thus reducing noise levels in the mission’s hover and axial motion segments. There are also active noise reduction mechanisms available such as active flaps, advanced blade design and manufacturing, and BluePulse [168], which can help reduce noise levels in flight, increasing comfort.



17 Lifecycle Cost Analysis

Conducting a lifecycle cost analysis is fundamental to assessing whether *Balto* can be feasibly used as an Air Taxi in the UAM and AAM vertical lift sectors. Cost per flight mile must be affordable and comparable to estimated industry prices for standard UAM flights. The cost analysis of *Balto* was performed using the cost modules within the open-source sizing code that was utilized in the design of Airbus’s Vahana [169], a single-seat, all-electric, tilt-wing vehicle demonstrator [170].

Examination of *Balto*’s acquisition cost, operating cost, and maintenance cost will help ensure that *Balto* has satisfactory economic performance over its service life. Sections 17.1 to 17.3 detail the cost. Subsection 17.4 will compare *Balto* to other competing UAM alternatives.

17.1 Acquisition Cost

The acquisition cost of a vehicle is comprised of the expenses incurred when obtaining new equipment [171]. Total acquisition cost of *Balto* includes, but is not limited to, the cost of airframe tooling, materials, batteries, motors, avionics, landing gear, and any additional medical or safety equipment used onboard. The cost breakdown for each component is shown in Table 17.1.

The airframe tooling cost was estimated based on component dimensions, component material, rough and fine machining, and any finishing process. Total tooling cost of *Balto* was determined by summing the individual tooling costs of the fuselage, wings, lifting rotor and cruise propeller blades, horizontal and vertical stabilizers, and control surfaces. The acquisition cost of the batteries, motors, servo, and gearbox were determined from the information gathered in Section 12, including current vendor costs. Avionics and landing gear costs were computed from examination of current technologies [172, 173]

Section 7 details the documentation used to calculate the medical or safety equipment costs. Accounting for all components, the acquisition cost of *Balto* is \$763,170. With a mission time of 49 minutes, quick turnaround time for battery recharge, simple ingress and egress using ramp, and a re-configurable cabin, it was assumed that *Balto* would be able to perform at least 8 flights per day based on the mission profile and be in operation for around 10 years [169]. To determine the acquisition cost per mission, the total acquisition cost was divided by flights per year and the lifetime of the vehicle. It is important to note that the regular inspection, maintenance, and overhaul down times might result in *Balto* not being able to fly 7 days a week; therefore, 60% of the year was found to be a more reasonable yearly usage of *Balto*. From this, the acquisition cost of *Balto* is calculated to be \$0.44 per flight mile.

Component	Cost (\$)
Airframe Tooling	11,819
Material	246,510
Battery	55,840
Motor	72,000
Servo	2,000
Gearbox	5,000
Avionics	360,000
Landing Gear	10,000
Medical Equipment	5,000
Total	763,170

Table 17.1 *Balto*’s acquisition cost breakdown

17.2 Operating Cost

Operating cost includes all expenses related to the operation of a vehicle. It includes: the facility rental cost, insurance cost, and the energy cost for recharging the batteries between the missions. A breakdown of the operating cost is shown in Table 17.2.

Facility rental cost was computed based on the cost per unit area at the operating hub location and the vehicle footprint, accounting for an additional twice the footprint area for movement involved in maintenance and ground operations. The energy cost of *Balto* was estimated from rates in the US where average electrical rates for commercial purposes are \$0.11 per kW-hr [174] and the batteries were assumed to be recharged at 100% efficiency. From Vahana’s code methodology, insurance cost was estimated to be around 6.5% of the total acquisition cost [169]. In total, the operating cost was calculated to be \$30 per flight mile.



Component	Cost per Flight Mile (\$)
Facility	29.9
Insurance	0.17
Energy	0.16
Total	30.19

Table 17.2 *Balto's* operating cost breakdown

Component	Cost per Flight Mile(\$)
Battery Replacement	0.28
Motor Replacement	0.098
Servo Replacement	0.005
Gearbox Replacement	0.008
Labor	0.17
Total	0.56

Table 17.3 *Balto's* maintenance cost breakdown

17.3 Maintenance Cost

Maintenance is needed in order to prolong the lifespan of machinery equipment, and the associated expenses include replacement costs for batteries, motors, servos, and gearbox which are calculated based on the components' life cycles and labor costs. A breakdown of the maintenance cost is shown in Table 17.3. Total maintenance cost of *Balto* is \$0.56 per flight mile.

17.4 Cost Comparison

The total cost per mission of *Balto* was found by summing acquisition, operating, and maintenance costs. It is estimated to be approximately \$3,100 per mission, or \$31 per flight mile.

According to Linear Air, [175], the starting price for an Air Taxi from Dallas/Fort Worth International Airport (DFW) to Wichita Falls Regional Airport (SPS), totals to \$4,332. This flight has a commute time of around 46 minutes with three passengers for a distance of 120 miles, making it comparable to the RFP-designated mission profile. For a four-passenger, 100 miles mission similar to *Balto's*, the Linear Air flight mile cost would be around \$48.00, over 1.5 times greater than *Balto*.

During the Uber Elevate Summit of 2019, the current Head of Product at Joby Aviation, Dr. Eric Allison, estimated a cost of \$5.73 per passenger mile for UberAir (now extinct) [176]. For *Balto's* four-passenger, 100 miles mission, their flight mile cost would have been around \$23.00, but without the accommodations for PRM or other disabilities.

Evaluation of competing technologies show that *Balto's* cost per flight mile falls between these two estimates. While more costly than the Uber configuration, it is important to note that *Balto* is designed specifically for the safety and comfort of PRM, unlike other Air Taxi concepts. The configuration also accounts for luggage, carry-ons, and medical equipment, further justifying the estimated cost of the vehicle. The cost analysis shows that the adoption of *Balto* as an air taxi is financially feasible.

As per the Air Taxi market research statistics [177], *Balto*, being all electric, multicopter, with four-passenger capacity, falls under the most lucrative Air Taxi market segments for the years 2021-2030 assuring revenue generation in its role as an Air Taxi.

18 Summary

The Georgia Institute of Technology graduate team designed *Balto* to meet all the vehicle and operational requirements specified in the Request for Proposals for an eVTOL Air Taxi for Passengers with Reduced Mobility (PRM) for the 2022 VFS Student Design Competition. *Balto* is a fully-electric thrust and lift compounding multirotor that is designed with the safety and comfort of its passengers at the forefront. The reconfigurable cabin offers one configuration that accommodates four passengers on regular seats, and configuration that accommodates two passengers with reduced mobility and their caregivers.

After a literature review, extensive consultations with Anne Jannarone, the Director of Georgia Tech's Office of Disability Services, and Bob Shaffer, a travel agent that specializes in travel for people with disabil-



ities, allowed Georgia Tech's team to fully understand the specific needs for people with disabilities. *Balto's* cabin is designed so that all passengers feel comfortable, safe and respected while aboard the vehicle.

Balto's lifting rotors and cruise propellers allow for zero vehicle tilt over the entire mission for maximum comfort, while the landing gear, control system, and crash-worthy seats provide optimum safety. With a cruise speed of 54 m/s (105 knots), *Balto* can complete the 160 km (100 mi) mission in less than an hour, making it a great alternative to road travel. With its large payload capacity and spacious cabin, *Balto* is an inclusive, comfortable and safe air taxi.

A series of design features allow *Balto* to fulfil the mission requirements as efficiently as possible. *Balto* is equipped with multiple lifting rotors that can withstand single points of electrical failure can glide to safety with wings in the case of a catatonic failure of the tractor propellers. In the cruise configuration, *Balto* utilizes the rotor blown wing which experiences an increase in the velocity over the wing from the wake of the cruise propellers to generate additional lift. This decreases the the required wing area making *Balto* a more versatile vehicle. *Balto* is also fitted with extreme energy absorbing landing gear constant and slow rate of deceleration which provides for a softer landing and mitigates any rebound that will be uncomfortable or further injurious to passengers with mobility restrictions.



References

- [1] Airbus, “CityAirbus NextGen - Urban Air Mobility,” <https://www.airbus.com/en/innovation/zero-emission/urban-air-mobility/cityairbus-nextgen>, accessed 2022-04-27.
- [2] Joby Aviation, “Joby Aviation - Home,” <https://www.jobyaviation.com>, accessed 2022-04-27.
- [3] Center for Disease Control, “CDC: 1 in 4 US adults live with a disability,” 2022, <https://www.cdc.gov/media/releases/2018/p0816-disability.html>, accessed 2022-04-27.
- [4] The Civic Air Transport Association (CIVATAglobal) & Aeromobility, “Urban Air Mobility has the power to transform the lives of millions... But only if we make it inclusive and accessible [White Paper],” Tech. rep., The Civic Air Transport Association (CIVATAglobal) & Aeromobility, April 2021.
- [5] Bell, “39th Annual Student Design Competition 2021-2022 Request for Proposal (RFP) – eVTOL Air Taxi for Passengers with Reduced Mobility (PRM),” Tech. rep., Vertical Flight Society, August 2021.
- [6] World Health Organization, Regional Office for Africa, “Disabilities Overview,” <https://www.afro.who.int/health-topics/disabilities>, accessed 2022-01-14.
- [7] Americans with Disabilities Act, “Introduction to the ADA,” https://www.ada.gov/ada_intro.htm, accessed 2022-01-14.
- [8] Jannarone, A. L., Personal communications with Georgia Tech’s Office of Disability Services, with Atte, Bonnet, Safieh, and Srivathsan, January 23, 2022.
- [9] Braithwaite, D. O. and Thompson, T. L., *Handbook of communication and people with disabilities: research and application*, Routledge, 2000.
- [10] Center for Talent Innovation, “Disabilities and Inclusion: US findings,” 2017, <https://www.cdc.gov/media/releases/2018/p0816-disability.html>, accessed 2022-04-27.
- [11] National Seating & Mobility, “Wheelchair Ramps Are Not Only For Wheelchairs,” <https://www.nsm-seating.com/blog/wheelchair-ramps-are-not-only-for-wheelchairs/>, accessed 2022-03-28.
- [12] Wolfinbarger, K. G. and Shehab, R. L., “A Survey of Ramp and Stair Use among Older Adults,” *Proceedings of the Human Factors and Ergonomics Society Annual Meeting*, Vol. 44, No. 24, 2000. doi:10.1177/154193120004402421.
- [13] Paralyzed Veterans of America, “The Air Carrier Access Act: Protecting passengers with disabilities,” <https://pva.org/research-resources/disability-rights-advocacy/air-carrier-access-act/>, accessed 2022-01-14.
- [14] Office of Civil Rights, FAA, “14 CFR § 382.67 - What is the requirement for priority space in the cabin to store passengers’ wheelchairs?” 2022, <https://www.law.cornell.edu/cfr/text/14/382.67>, accessed 2022-03-28.
- [15] Poria, Y., Reichel, A., and Brandt, Y., “The Flight Experiences of People with Disabilities: An Exploratory Study,” *Journal of Travel Research*, Vol. 49, No. 2, 2010, pp. 216–227. doi:10.1177/0047287509336477.
- [16] American Printing House, “Annual Report from the American Printing House for the Blind,” 2020, <https://aph.nyc3.digitaloceanspaces.com/app/uploads/2021/02/26065950/Annual-Report-FY2020.pdf>.
- [17] NPR, “Braille Under Siege As Blind Turn To Smartphones,” 2012, <https://www.npr.org/sections/alltechconsidered/2012/02/13/146812288/braille-under-siege-as-blind-turn-to-smartphones>, accessed 2022-01-26.



- [18] Mackenzie, I. and Smith, A., “Deafness – the neglected and hidden disability,” *Annals of Tropical Medicine & Parasitology*, Vol. 103, No. 7, 2009, pp. 565–571. doi:10.1179/000349809X12459740922372.
- [19] World Health Organization, “Epilepsy,” <https://www.who.int/news-room/fact-sheets/detail/epilepsy>, accessed 2022-03-09.
- [20] Centers for Disease Control and Prevention, “Epilepsy Fast Facts,” <https://www.cdc.gov/epilepsy/about/fast-facts.htm>, accessed 2022-03-09.
- [21] Baker, G. A., Hargis, E., Hsieh, M. M.-S., Mounfield, H., Arzimanoglou, A., Glauser, T., Pellock, J., and Lund, S., “Perceived impact of epilepsy in teenagers and young adults: An international survey,” *Epilepsy and Behavior*, Vol. 12, No. 3, 2008, pp. 395 – 401. doi:10.1016/j.annals.2019.102856.
- [22] McIntosh, A. J., “The hidden side of travel: Epilepsy and tourism,” *Annals of Tourism Research*, Vol. 81, 2020. doi:10.1016/j.annals.2019.102856.
- [23] Cushman, J. T. and Floccare, D. J., “Flicker Illness: An Underrecognized but Preventable Complication of Helicopter Transport,” 2007, <https://go.openathens.net/redirector/gatech.edu?url=https://search.proquest.com/scholarly-journals/flicker-illness-underrecognized-preventable/docview/221188597/se-2?accountid=11107>, accessed 2022-01-24.
- [24] High, K. H. and Moore, A., “Unknown, Unrecognized, and Underreported: Flicker Vertigo in Helicopter Emergency Medical Services,” *Air Medical Journal*, Vol. 31, No. 3, 2012, pp. 129–130. doi:10.1016/j.amj.2011.08.012.
- [25] Harding, G., Harding, P., and Wilkins, A., “Wind turbines, flicker, and photosensitive epilepsy: Characterizing the flashing that may precipitate seizures and optimizing guidelines to prevent them,” *Epilepsia*, Vol. 49, No. 6, 2008, pp. 1095–1098. doi:10.1111/j.1528-1167.2008.01563.x.
- [26] Centers for Disease Control and Prevention, “What is Autism Spectrum Disorder?” <https://www.cdc.gov/ncbddd/autism/facts.html>, accessed 2022-04-15.
- [27] Centers for Disease Control and Prevention, “Autism and Developmental Disabilities Monitoring (ADDM) Network,” <https://www.cdc.gov/ncbddd/autism/addm.html>, accessed 2022-04-15.
- [28] The Arc, “Wings for Autism / Wings for All,” <https://thearc.org/our-initiatives/travel/>, accessed 2022-04-15.
- [29] The Arc, “Wings for Autism / Wings for All,” <https://www.autism.org.uk/advice-and-guidance/topics/sensory-differences/sensory-differences/all-audiences>, accessed 2022-04-15.
- [30] American Psychiatric Association, “What Is Mental Illness?” 2022, <https://www.psychiatry.org/patients-families/what-is-mental-illness>, accessed 2022-03-05.
- [31] National Institute of Mental Health, “Mental Illness,” 2022, <https://www.nimh.nih.gov/health/statistics/mental-illness>, accessed 2022-03-05.
- [32] National Alliance on Mental Illness, “Mental Health By the Numbers,” 2022, <https://www.nami.org/mhstats>, accessed 2022-03-05.
- [33] McManus, S., Meltzer, H., Brugha, T., Bebbington, P. E., and Jenkins, R., “Adult psychiatric morbidity in England, 2007: Results of a household survey,” *Adult Psychiatric Morbidity Survey*, January 2009. doi:10.13140/2.1.1563.5205.
- [34] Healthdirect Australia, “Types of mental illness,” 2022, <https://www.healthdirect.gov.au/types-of-mental-illness>, accessed 2022-03-05.
- [35] Johns Hopkins Medicine, “Mood Disorders,” 2022, <https://www.hopkinsmedicine.org/health/conditions-and-diseases/mood-disorders>, accessed 2022-03-05.



- [36] American Psychiatric Association, *Diagnostic and statistical manual of mental disorders*, American Psychiatric Association, 5th ed., 2013.
- [37] Mayo Clinic, “Anxiety disorders,” 2022, <https://www.mayoclinic.org/diseases-conditions/anxiety/symptoms-causes/syc-20350961>, accessed 2022-03-05.
- [38] Standing, L. and Stace, G., “The Effects of Environmental Noise on Anxiety Level,” *The Journal of General Psychology*, Vol. 103, No. 2, 2010. doi:10.1080/00221309.1980.9921007.
- [39] Healthdirect Australia, “Personality disorders: an overview,” 2022, <https://www.healthdirect.gov.au/personality-disorders>, accessed 2022-03-05.
- [40] Medline Plus, “Psychotic disorders,” 2022, <https://medlineplus.gov/psychoticdisorders.html>, accessed 2022-03-05.
- [41] National Institute of Mental Health, “Eating Disorders,” 2022, <https://www.nimh.nih.gov/health/topics/eating-disorders>, accessed 2022-03-05.
- [42] Children’s Hospital of Philadelphia, “Trauma and Stressor-related Disorders in Children,” 2022, <https://www.chop.edu/conditions-diseases/trauma-and-stressor-related-disorders-children>, accessed 2022-03-05.
- [43] Peterson, R. L. and Pennington, B. F., “Developmental Dyslexia,” *Annual Review of Clinical Psychology*, Vol. 1, No. 1, 2015, pp. 283–307. doi:10.1146/annurev-clinpsy-032814-112842.
- [44] Lyon, G. R., Shaywitz, S. E., and Shaywitz, B. A., “A definition of dyslexia,” *Annals of Dyslexia*, Vol. 53, 2003, pp. 1–14. doi:10.1007/s11881-003-0001-9.
- [45] Boer, C., “Dyslexie: A Unique Typeface, Better Reading for Everybody,” <https://www.dyslexiefont.com/en/typeface/>, accessed 2022-03-02.
- [46] Diliberto, J. A. and Wery, J. J., “The effect of a specialized dyslexia font, OpenDyslexic, on reading rate and accuracy,” *Annals of Dyslexia*, Vol. 67, 2017, pp. 114–127. doi:10.1007/s11881-016-0127-1.
- [47] Kuster, S. M., van Weerdenburg, M., Gompel, M., and Bosman, A. M. T., “Dyslexie font does not benefit reading in children with or without dyslexia,” *Annals of Dyslexia*, Vol. 68, No. 1, 2018, pp. 25–42. doi:10.1007/s11881-017-0154-6.
- [48] Ari, O., “Dyslexia Fonts: What Postsecondary Instructors Need to Know,” *Journal of College Reading and Learning*, Vol. 52, No. 1, 2021, pp. 64–71. doi:10.1080/10790195.2021.1986430.
- [49] Perea, M., Panadero, V., Moret-Tatay, C., and Gómez, P., “The effects of inter-letter spacing in visual-word recognition: Evidence with young normal readers and developmental dyslexics,” *Learning and Instruction*, Vol. 22, 2012, pp. 420–430. doi:10.1080/10790195.2021.1986430.
- [50] Marinus, E., Mostard, M., Segers, E., Schubert, T. M., Madelaine, A., and Wheldall, K., “A Special Font for People with Dyslexia: Does it Work and, if so, why?” *Dyslexia*, Vol. 22, No. 3, 2016, pp. 233–244. doi:10.1002/dys.1527.
- [51] Americans with Disabilities Act, “ADA 2010 Revised Requirements: Service Animals,” https://www.ada.gov/service_animals_2010.htm, accessed 2022-03-07.
- [52] U.S. Department of Transportation, “U.S. Department of Transportation Announces Final Rule on Traveling by Air with Service Animals,” <https://www.transportation.gov/briefing-room/us-department-transportation-announces-final-rule-traveling-air-service-animals>, accessed 2022-03-07.
- [53] Pittsburgh Post-Gazette Editorial Board, “Service dog dilemma: Untrained animals should not be in plane cabins,” <https://www.post-gazette.com/opinion/editorials/2020/02/09/Service-dogs-untrained-animals-airplanes/stories/202001240038>, accessed 2022-03-07.



- [54] Canine Companions for Independence, “New Rules for Service and Emotional Support Animals on Planes make a Difference,” <https://www.prnewswire.com/news-releases/new-rules-for-service-and-emotional-support-animals-on-planes-make-a-difference-301188698.html>, accessed 2022-03-07.
- [55] ESA Doctors, “How to Fly with a Large Dog,” <https://esadoctors.com/how-to-fly-with-esa-dog/>, accessed 2022-03-07.
- [56] Zevitas, C., Spengler, J., Jones, B., McNeely, E., Coull, B., Cao, X., Ming Loo, S., Hard, A., and Allen, J., “Assessment of noise in the airplane cabin environment,” *Journal of Exposure Science & Environmental Epidemiology*, Vol. 28, 2018, pp. 568–578. doi:10.1038/s41370-018-0027-z.
- [57] Kim, J., Lee, W., Won, J., Yoon, J., Seok, H., Kim, Y., Lee, S., and Roh, J., “The relationship between occupational noise and vibration exposure and headache/eyestrain, based on the fourth Korean Working Condition Survey (KWCS),” *PLoS One*, Vol. 23, 05 2017. doi:10.1371/journal.pone.0177846.
- [58] Ashkenazi, A., Mushtaq, A., Yang, I., and Oshinsky, M., “Ictal and interictal phonophobia in migraine – a quantitative controlled study,” *Cephalalgia*, Vol. 29, 10 2009, pp. 1042–1048. doi:doi:10.1111/j.1468-2982.2008.01834.x.
- [59] Vertical Aerospace Group, “Vertical Aerospace - Pioneering electric aviation,” <https://vertical-aerospace.com>, accessed 2022-04-27.
- [60] Coldewey, D., “Lift Aircraft’s Hexa may be your first multirotor drone ride,” 2018, https://techcrunch.com/2018/12/11/lift-aircrafts-hexa-may-be-your-first-multirotor-drone-ride/?guccounter=1&guce_referrer=aHR0cHM6Ly93d3cuZ29vZ2xlLmNvbS8&guce_referrer_sig=AQAAADUF45MD6ai4vcfK-g10bIs04h97voc3spm-wG0zb4L81NcCQCQuB77LVouSjD9AtOpiAMurtTm6fCyB8MnM-sETfmGel, accessed 2022-05-20.
- [61] Bell Textron Inc., “Bell UH-1Y - The Ultimate Utility Helicopter,” 2022, <https://www.bellflight.com/products/bell-uh-1y>, accessed 2022-05-20.
- [62] Airforce Technology, “Ka-52 Alligator Attack Helicopter,” 2013, <https://www.airforce-technology.com/projects/ka52-alligator-attack-helicopter-russia/>, accessed 2022-05-20.
- [63] Lockheed Martin, “SB₁ DEFIANT[®],” 2022, <https://www.lockheedmartin.com/en-us/products/sb1-defiant-technology-demonstrator.html>, accessed 2022-05-20.
- [64] Boeing, “Boeing: H-47 Chinook,” 2022, <https://www.boeing.com/defense/ch-47-chinook/>, accessed 2022-05-20.
- [65] Bell Textron Inc., “Bell Boeing V-22 - Un avantage incomparable pour les assauts aériens et les opérations spéciales,” 2022, <https://fr.bellflight.com/products/bell-boeing-v-22>, accessed 2022-05-20.
- [66] Airbus, “Demonstrated the viability of a self-piloted, electric urban air mobility vehicle,” 2022, <https://acubed.airbus.com/projects/vahana/>, accessed 2022-05-20.
- [67] Department, S. B. C. F., “Kaman “K-Max”,” 2022, <https://www.sbcfire.com/links/2414-types-of-fixed-wing-aircraft-and-helicopters/resources/8941-kaman-k-max>, accessed 2022-05-20.
- [68] 19fortyfive, “Convair XFY Pogo: This Strange Plane Almost Flew From Navy Aircraft Carriers,” 2021, <https://www.19fortyfive.com/2021/06/convair-xfy-pogo-this-strange-plane-almost-flew-from-navy-aircraft-carriers/>, accessed 2022-05-20.



- [69] Flying mag, “Following Bankruptcy, Enstrom Helicopter Corporation is Resurrected,” 2021, <https://www.flyingmag.com/following-bankruptcy-enstrom-helicopter-corporation-is-resurrected/>, accessed 2022-05-20.
- [70] Wisk Aero LLC., “Discover the Future of Urban Air Mobility,” 2022, <https://wisk.aero/aircraft/>, accessed 2022-05-20.
- [71] Reed, J., “Jaunt Air Mobility and Avports Partner to Advance eVTOL Integration,” 2022, <https://www.aviationtoday.com/2022/02/16/jaunt-air-mobility-and-avports-partner-to-advance-evtol-integration/>, accessed 2022-05-20.
- [72] Leishman, J. G., *Principles of Helicopter Aerodynamics*, Vol. 1, Cambridge University Press, 2006.
- [73] Johnson, W., *Helicopter Theory*, Vol. 1, Dover Publications, 1980.
- [74] Johnson, W., *Rotorcraft Aeromechanics*, Cambridge University Press, 2013.
- [75] Anderson, J., *Fundamentals Aerodynamics 6th edition*, McGraw Hill Education Press, 6th ed., 2017.
- [76] Inderjit Chopra, A. D., *Helicopter Dynamics*, 2019.
- [77] Nagaraj, V. T. and Chopra, I., *Preliminary Design of Rotorcraft*, 2020.
- [78] Safieh, D. A., Lent, A., Cohen, J., Young, T., Azadze, E., Williams, R., Kaplan, N., Zufar, A., and Schmidt, J., “Garra Final Proposal Undergraduate Design Team, University of Maryland,” http://vfs.umd.edu/assets/downloads/2021_garra.pdf, accessed 2022-05-20.
- [79] Anderson, J., *Aircraft performance and design*, McGraw Hill Education Press, 11th ed., 2010.
- [80] Reynard de Vries, M. F. M. H. and Vos, R., “Range Equation for Hybrid-Electric Aircraft with Constant Power Split,” *AIAA Journal of Aircraft*, Vol. 57, No. 3, 4 2020. doi:<https://doi.org/10.2514/1.C035734>.
- [81] Ben Brelje, “Deriving the modified Breguet range equation for a hybrid-turboelectric aircraft,” 2017, <https://brelje.net/blog/deriving-modified-breguet-range-equation-hybrid-turboelectric-aircraft/>, accessed 2022-05-21.
- [82] Hodara, J., *Hybrid RANS-LES Closure for Separated Flows in the Transitional Regime*, Ph.D. thesis, Georgia Institute of Technology, Atlanta, Georgia, 2016, <https://smartech.gatech.edu/handle/1853/54995>.
- [83] Menter, F. R., Kuntz, M., and Langtry, R., “Ten Years of Industrial Experience with the SST Turbulence Model,” *Turbulence, Heat and Mass Transfer*, Vol. 4, No. 1, 2003, pp. 625–632.
- [84] Bonnet, C. and Smith, M. J., “Development of Nonlinear Transverse Wing-Gust Models for Urban Environments,” *56th 3AF International Conference on Applied Aerodynamics, Toulouse, France*, March 2022.
- [85] Ramasamy, M., “Measurements Comparing Hover Performance of Single, Coaxial, Tandem, and Tilt-Rotor Configurations,” *AHS 69th Annual Forum*, May 2013.
- [86] Drela, M., “XFOIL Subsonic Airfoil Development System,” 2013, <https://web.mit.edu/drela/Public/web/xfoil/>, accessed 2022-05-23.
- [87] Drela, M. and Youngren, H., “AVL,” 2022, <https://web.mit.edu/drela/Public/web/avl/>, accessed 2022-05-23.
- [88] Research In Flight, “FlightStream Fast Aerodynamics with Fidelity,” 2004, <https://researchinflight.com/>, accessed 2022-02-06.



- [89] Schaeffler, N. W., Allan, B. G., Lienard, C., and Pape, A. L., “Progress Towards Fuselage Drag Reduction via Active Flow Control: A Combined CFD and Experimental Effort,” *36th European Rotorcraft Forum, Paris*, 2010.
- [90] ©, A., “Aim, Release 19.1, Help System, Static Structural Analysis Guide, ANSYS, Inc,” 2018, <https://www.ansys.com/>, accessed 2022-05-29.
- [91] Floros, M. W. and Johnson, W., “Performance Analysis of the Slowed-Rotor Compound Helicopter Configuration,” *Journal of the American Helicopter Society*, Vol. 54, No. 2, 2009, pp. 22002–22002.
- [92] Spinlife, “Jazzy 600 ES,” 2022, https://www.spinlife.com/Pride-Jazzy-600-ES-Full-Size-Power-Wheelchairs/spec.cfm?productID=103386&adv=googlepla&utm_medium=CSE&utm_source=googlepla&utm_term=&utm_campaign=11097663967&gclid=Cj0KCQiAosmPBhCPARIsAH0en-MdH3eVjPAdLzAHUJ-0Y-NcvJVgcHyUgObt_wcB, accessed 2022-02-18.
- [93] Mobility Direct, “Merits Health P301 Gemini Power Wheelchair,” 2022, <https://www.mobilityscootersdirect.com/merits-health-usa/merits-health-p301-gemini-power-wheelchair.html>, accessed 2022-02-18.
- [94] Spinlife, “Jazzy 1450,” 2022, https://www.spinlife.com/Pride-Jazzy-1450-Heavy-Duty/High-Weight-Capacity-Power-Wheelchair/spec.cfm?productID=98260&adv=googlepla&utm_medium=CSE&utm_source=googlepla&utm_term=&utm_campaign=610148043&gclid=Cj0KCQiAosmPBhCPARIsAH0en-MLGf21b5A179d6Ye70kh7cierLfyywv6V0duSGlhYBFSWNkC3soa0oaAluwEALw_wcB, accessed 2022-02-18.
- [95] Sunrise Medical, “QUICKIE Life R,” 2022, <https://www.sunrisemedical.eu/wheelchairs/quickie/lightweight-wheelchairs/life-r#specifications>, accessed 2022-02-18.
- [96] Ki Mobility, “TsunamiALX,” 2022, <https://www.kimobility.com/Product.action?productName=Tsunami+ALX>, accessed 2022-02-18.
- [97] Shaffer, B., Personal communications with a Luxury Travel Advisor Specialized in Travel for Passengers with Reduced Mobility, with Atte and Bonnet, January 31st, 2022.
- [98] Hiller Aircraft Corp., “Proposal for the Light Observation Helicopter (Army) - Weight Report,” Tech. rep., Hiller Aircraft Corporation, December 1960.
- [99] Cessna, “MODEL 172S - Weight and Balance Equipment List,” Tech. rep., Cessna Aircraft, July 1998.
- [100] ETC Connect, “Eos Augment3d - Expert Topics,” 2022, <https://www.etcconnect.com/Support/Tutorials/Expert-Topics/Augment3d.aspx>, accessed 2022-05-06.
- [101] Personal communications with Hugues Moreau (CEO IAS), and Jean-Marc Trolard (Technical Director IAS Group) with Bonnet, April 30 and May 4, 2022.
- [102] Chrysler, “2022 Chrysler Pacifica Interior - Seating, Storage & More,” 2022, <https://www.chrysler.com/pacifica/interior.html>, accessed 2022-02-06.
- [103] Stellantis Media, “Stow ’N Go™ Seating and Storage System Solidifies Dodge Caravan as the Leader in Minivan Sales and Innovations,” 2005, <https://media.stellantisnorthamerica.com/newsrelease.do?id=129>, accessed 2022-02-06.
- [104] BraunAbility Europe AB, “Wheelchair tie-down and occupant restraint system,” <https://www.braunability.eu/en/products/tie-downs-and-seatbelts/wtors/>, accessed 2022-01-08.
- [105] van Roosmalen, L., Bertocci, G. E., Hobson, D. A., and Karg, P., “Preliminary evaluation of wheelchair occupant restraint system usage in motor vehicles,” *Journal of Rehabilitation Research and Development*, Vol. 39, No. 1, Jan - Feb 2002, pp. 83 – 93, <https://citeseerx.ist.psu.edu/viewdoc/download?doi=10.1.1.612.1877&rep=rep1&type=pdf>, accessed 2022-01-08.



- [106] BraunAbility Europe AB, “Rails - Low profile rail,” <https://www.braunability.eu/en/products/flooring-and-seating/rails/#tab2>, accessed 2022-01-08.
- [107] Bertocci, G., Digges, K., and Hobson, D., “Shoulder belt anchor location influences on wheelchair occupant crash protection,” *Journal of Rehabilitation Research and Development*, Vol. 33, No. 3, July 1996, pp. 279 – 289, <https://www.rehab.research.va.gov/jour/96/33/3/pdf/bertocci.pdf>, accessed 2022-01-08.
- [108] BraunAbility Europe AB, “Upper Anchorage Point,” <https://www.braunability.eu/en/products/flooring-and-seating/upper-anchorage-point/>, accessed 2022-01-08.
- [109] Lombaerts, T., Kaneshige, J., and Feary, M., “Control Concepts for Simplified Vehicle Operations of a Quadrotor eVTOL Vehicle,” *AIAA Aviation 2020 Forum*, June 2020.
- [110] Joby Aviation, “How We Reinvented Flight Controls for the Joby eVTOL Aircraft,” 2022, https://www.youtube.com/watch?v=60ocd_6g2Vg, accessed 2022-05-30.
- [111] Hawkins, A. J., “Joby Aviation inches closer to getting full government approval for its electric air taxis,” <https://www.theverge.com/2022/5/26/23141849/joby-aviation-faa-certification-part-135-evtol>, accessed 2022-05-30.
- [112] PSN Team, “CARES Gives Parents Of Older Disabled Children Freedom to Fly,” 2022, <https://www.parentingspecialneeds.org/article/cares-disabled-children-freedom-fly/>, accessed 2022-05-20.
- [113] Office of Civil Rights, FAA, “Airport Disability Compliance - Accessible Aircraft Boarding Equipment and Service Overview,” https://www.faa.gov/sites/faa.gov/files/about/office_org/headquarters_offices/acr/Day2_Sess_3_Access_Aircraft_Board_Equip_and_Service.pdf, accessed 2022-03-28.
- [114] Americans with Disabilities Act, “About the ADA Accessibility Standards,” <https://www.access-board.gov/ada/#ada-303>, accessed 2022-05-22.
- [115] Lee, S.-K., Seungmin Lee, J. B., and Shin, T., “A New Method for Active Cancellation of Engine Order Noise in a Passenger Car,” *Applied Sciences*, , No. 8, 2018, pp. 1394. doi:10.3390/app8081394.
- [116] Bai, M. R. and Chen, H., “Active Cancellation of Noise in a Car Cabin Using the Zero Spillover Controller,” *Journal of Sound and Vibration*, Vol. 5, No. 235, 2000, pp. 787–800. doi:10.1006/jsvi.2000.2958.
- [117] Ma, X., Lu, Y., and Wang, F., “Active structural acoustic control of helicopter interior multifrequency noise using input-output-based hybrid control,” *Journal of Sound and Vibration*, , No. 405, 2017, pp. 187–207. doi:10.1016/j.jsv.2017.05.051.
- [118] Akiho, M., Masakatsu, Haseyama, M., and Kitajima, H., “Performance Improvements on MEFX-LMS Based Noise Cancelling System in Vehicle Cabin,” *IEEE International Symposium on Circuits and Systems, Geneva*, 2000.
- [119] Smith, M., Personal communications based on prior analysis and design of various UAM/AAM and traditional helicopters, February, 2022.
- [120] Faisal Mahmuddina, Syerly Klaraa, H. S. S. H., “Airfoil Lift and Drag Extrapolation with Viterna and Montgomerie Methods,” *The 8th International Conference on Applied Energy – ICAE2016*, October 2016.
- [121] jmp Statistical Discovery, “jmp Statistical Software,” 2022, https://www.jmp.com/en_us/home.htm, accessed 2022-03-14.
- [122] McCormick, B., *Aerodynamics, Aeronautics, and Flight Mechanics*, Vol. 1, Wiley, 1979.



- [123] Bodine Electric Company, “42A5-FX Parallel Shaft DC Gearmotor,” 2020, <https://www.bodine-electric.com/products/dc-parallel-shaft-gearmotors/42a5-fx-parallel-shaft-dc-gearmotor/5056/>, accessed 2022-05-30.
- [124] Yogesh Ashok Ingale, A. P. Kadam, D. G. B., “COMPARATIVE STUDY OF STEEL, NYLON 66 AND DELRIN HELICAL GEARS USED IN STEERING GEARBOX,” *IJRET: International Journal of Research in Engineering and Technology*, Vol. 5, 6 2016. doi:eISSN: 2319-1163.
- [125] Damijan Zorko, Joze Duhovnik, J. T., “Different teeth profile shapes of polymer gears and comparison of their performance,” *Journal of Advanced Mechanical Design Systems and Manufacturing*, Vol. 5, 1 2017. doi:DOI: 10.1299/jamdsm.2017jamdsm0083.
- [126] Manager, “Why Circles Are Better Than Squares – An Introduction to Geometric Tolerancing,” 2017, <https://www.plextek.com/why-circles-are-better-than-squares-an-introduction-to-geometric-tolerancing/>, accessed 2022-05-21.
- [127] Hoerner, S. F., *Fluid-Dynamic Lift: Practical Information on Aerodynamic and Hydrodynamic Lift*, 2nd ed., 1985.
- [128] Gudmundsson, S., *Aircraft performance and design*, Butterworth-Heinemann, 1st ed., 2014.
- [129] Dassault Systèmes, “SolidWorks,” 2022, <https://www.solidworks.com/>, accessed 2022-05-31.
- [130] Constellium, “Airware 2050-T84 PLATE,” Brochure, 2017.
- [131] Staruk, W., Woods, B. K. S., Berry, B., and Bowen-Davies, G., “Design and fabrication of ultra-lightweight composite structures for the gamera human-powered helicopters,” 2012.
- [132] Shams, T. A., Shah, S. I. A., Ahmad, M. A., Mehmood, K., Ahmad, W., and Rizvi, S. T. u. I., “Selection Methodology of an Electric Actuator for Nose Landing Gear of a Light Weight Aircraft,” *Applied Sciences*, Vol. 10, No. 23, 2020. doi:10.3390/app10238730.
- [133] Carter, J., “Air Taxi Concepts & Supporting Technologies,” 2016.
- [134] Technologies, C. A., “Carter Landing Gear - Drop Test,” 2012.
- [135] Raymer, D. P., *Aircraft design: A conceptual approach*, AIAA education series, American Institute of Aeronautics and Astronautics, 4th ed., 2006.
- [136] Currey, N. S., *Aircraft Landing Gear Design: Principles and Practices*, AIAA education series, American Institute of Aeronautics and Astronautics, 1984.
- [137] Timemetal, “Timemetal 10-2-3,” Brochure, 2000.
- [138] Maeve Arthur, E. and Institute, E. S., “A Look at the Status of Five Energy Storage Technologies,” 2020, <https://www.eesi.org/articles/view/a-look-at-the-status-of-five-energy-storage-technologies>, accessed 2022-05-30.
- [139] Battery University, “Types of Lithium-Ion,” 2021, <https://batteryuniversity.com/article/bu-205-types-of-lithium-ion>, accessed 2022-05-20.
- [140] Battery Universe, “Whats the difference between Nickel Cadmium (Nicad), Nickel-metal hydride (NiMH), and Lithium Ion (Li-Ion)?” <https://www.batteryuniverse.com/help/battery-chemistries>, accessed 2022-05-20.
- [141] canary media, “The many variates of lithium-ion batteries battling for market share,” 2021, <https://www.canarymedia.com/articles/batteries/the-many-varieties-of-lithium-ion-batteries-battling-for-market-share>, accessed 2022-05-20.



- [142] Nature Nanotechnology, “Reviving the lithium metal anode for high-energy batteries,” 2017, <https://www.nature.com/articles/nnano.2017.16>, accessed 2022-05-20.
- [143] Team, M. E. V., “A Guide to Understanding Battery Specifications,” 2008, http://web.mit.edu/evt/summary_battery_specifications.pdf, accessed 2022-05-25.
- [144] Engineering, L. E., “Basic Battery Terminology,” 2017, <https://www.electricalengineeringtoolbox.com/2017/07/basic-battery-terminology.html>, accessed 2022-05-25.
- [145] TYTO Robotics, “Brushless Motor Manufacturers for eVTOL and Aviation,” 2022, <https://www.tytorobotics.com/blogs/articles/brushless-motor-manufacturers-for-evtol-and-aviation>, accessed 2022-05-21.
- [146] EMARX, “Manual for EMRAX Motors / Generators,” Tech. rep., EMRAX Innovative E-Motors, March 2020.
- [147] Dengel, B. and Gear Solutions, “Finding the ideal materials for gears,” 2021, <https://gearsolutions.com/features/finding-the-ideal-materials-for-gears/#:~:text=four%2Ddigit%20sequence,-,Thermoplastics,injection%20molded%20thermoplastic%20is%20acetal>, accessed 2022-05-20.
- [148] Science Direct, “Gearbox Guide,” <https://www.sciencedirect.com/science/article/pii/B9780750673280500410>, accessed 2022-05-20.
- [149] Anaheim Automation, “Finding the ideal materials for gears,” 2021, <https://www.anaheimautomation.com/manuals/forms/gearbox-guide.php>, accessed 2022-05-20.
- [150] Neeraj Nijjaawan, R. N., *Modern Approach to Maintenance in Spinning*, Woodhead Publishing, 2010, <https://www.sciencedirect.com/science/article/pii/B9780857090003500155>, accessed 2022-05-31.
- [151] Kevin M. Lynch, Nicholas Marchuk, M. L., *Embedded Computing and Mechatronics with the PIC32*, Newnes, 2016, <https://www.sciencedirect.com/science/article/pii/B9780124201651000263>, accessed 2022-05-31.
- [152] Mobley, R. K., *Plant Engineer’s Handbook*, 2001, <https://www.sciencedirect.com/science/article/pii/B9780750673280500410>, accessed 2022-05-31.
- [153] Motion Control Tips, “What are the best methods for gearbox lubrication?” <https://www.motioncontroltips.com/gearbox-lubrication-best-methods/>, accessed 2022-05-22.
- [154] govinfo, “Content Details 14 CFR 29.927 - Additional tests,” <https://www.govinfo.gov/app/details/CFR-2011-title14-vol1/CFR-2011-title14-vol1-sec29-927/summary>, accessed 2022-05-22.
- [155] Aerossurance, “EASA Launch Helicopter Gearbox Lubrication Rule Making,” 2014, <http://aerossurance.com/helicopters/easa-launch-helicopter-gearbox-lubrication-rule-making/>, accessed 2022-05-22.
- [156] Charluet, C. and BOX, W. V. B. E., “How long does it take to charge an electric car?,” 2021, <https://blog.evbox.com/ev-charging-times>, accessed 2022-05-22.
- [157] pod point, “How Long Does It Take to Charge an Electric Car?” 2021, <https://pod-point.com/guides/driver/how-long-to-charge-an-electric-car>, accessed 2022-05-24.
- [158] Cory, R. and Tedrake, R., “Experiments in fixed-wing UAV perching,” *AIAA Guidance, Navigation and Control Conference and Exhibit*, 2008, p. 7256.
- [159] Etkin, B. and Reid, L. D., *Dynamics of flight*, Vol. 2, Wiley New York, 1959.
- [160] Nelson, R. C. et al., *Flight stability and automatic control*, Vol. 2, WCB/McGraw Hill New York, 1998.



- [161] Prasad, J. V. R., “AE6520 Advanced Flight Dynamics, Notes, Georgia Institute of Technology,” 2022.
- [162] Raymer, D., *Aircraft design: a conceptual approach*, American Institute of Aeronautics and Astronautics, Inc., 2012.
- [163] Caughey, D. A., “Introduction to Aircraft Stability and Control Course Notes for MAE 5070 Cornell University,” 2011.
- [164] Sadraey, M., *Aircraft Design: A Systems Engineering Approach*, Vol. 1, Wiley Publications, 2012.
- [165] Decibel Pro, “How Loud Is 70 dB?” 2022, <https://decibelpro.app/blog/how-loud-is-70-db/>, accessed 2022-05-18.
- [166] Vivek Ahuja, “FlightStream Aeroacoustics Toolbox: Early Design Aeroacoustics With OpenVSP Geometries,” http://openvsp.org/wiki/lib/exe/fetch.php?media=workshop21:flightstream_vsp_workshop_2021_acoustics.pdf, October 2021.
- [167] Engineering ToolBox, “Sound Pressure,” 2004, https://www.engineeringtoolbox.com/sound-pressure-d_711.html, accessed 2022-05-10.
- [168] Airbus, “Blue Pulse™ Creates a Buzz at Heli-Expo,” 2010, https://www.airbushelicopters.com/website/en/press/Blue-Pulse%E2%84%A2-Creates-a-Buzz-at-Heli-Expo_6.html, accessed 2022-05-31.
- [169] Project Vahana, “Vahana OpenSource – Vahana Trade Study Codes,” 2017, <https://github.com/VahanaOpenSource/vahanaTradeStudy>, accessed 2022-05-20.
- [170] Lovering, Z., “Vahana Configuration Trade Study — Part I,” 2016, <https://acubed.airbus.com/blog/vahana/vahana-configuration-trade-study-part-i/>, accessed 2022-05-20.
- [171] Investopedia, “Acquisition Cost,” 2022, <https://www.investopedia.com/terms/a/acquisition-cost.asp>, accessed 2022-05-31.
- [172] Infinity Aerospace, “The Infinity 1 Retractable Oleo Strut Main Landing Gear also fits other Canards,” 2016, <http://www.infinityaerospace.com/infgear.htm>, accessed 2022-05-31.
- [173] Johnson, O., “Hill Helicopters records over 200 HX50 sales; prototypes to fly in 2022,” *Vertical*.
- [174] Energy Information Administration, “TElectric Power Monthly,” 2022, https://www.eia.gov/electricity/monthly/epm_table_grapher.php?t=epmt_5_6_a, accessed 2022-05-31.
- [175] Linear Air, “Premium Air Taxi from DFW to SPS,” 2022, <https://www.linearair.com/flights/Dallas-Fort-Worth-International-in-Dallas-TX-DFW/Wichita-Falls-Regional-Sheppard-AFB-in-Wichita-Falls-TX-SPS/2022-06-30/1/>, accessed 2022-05-30.
- [176] Bellamy, W., “Rotor & Wing International - Uber Wants Full Electric Air Taxi Operational by 2023,” 2019, <https://www.rotorandwing.com/2018/05/09/uber-wants-full-electric-air-taxi-operational-2023/>, accessed 2022-05-30.
- [177] Singh, A. and Baul, S., “Allied Market Research - Air Taxi Market Statistics - 2030,” 2019, <https://www.alliedmarketresearch.com/air-taxi-market>, accessed 2022-05-31.

